1996

Cross-section study of ion-molecule reactions of planetary importance

Xu Li
Iowa State University

INFORMATION TO USERS

This manuscript has been reproduced from the microfilm master. UMI films the text directly from the original or copy submitted. Thus, some thesis and dissertation copies are in typewriter face, while others may be from any type of computer printer.

The quality of this reproduction is dependent upon the quality of the copy submitted. Broken or indistinct print, colored or poor quality illustrations and photographs, print bleedthrough, substandard margins, and improper alignment can adversely affect reproduction.

In the unlikely event that the author did not send UMI a complete manuscript and there are missing pages, these will be noted. Also, if unauthorized copyright material had to be removed, a note will indicate the deletion.

Oversize materials (e.g., maps, drawings, charts) are reproduced by sectioning the original, beginning at the upper left-hand corner and continuing from left to right in equal sections with small overlaps. Each original is also photographed in one exposure and is included in reduced form at the back of the book.

Photographs included in the original manuscript have been reproduced xerographically in this copy. Higher quality 6" x 9" black and white photographic prints are available for any photographs or illustrations appearing in this copy for an additional charge. Contact UMI directly to order.

UMI

A Bell & Howell Information Company
300 North Zeeb Road, Ann Arbor MI 48106-1346 USA
313/761-4700 800/521-0600

Cross-section study of ion-molecule reactions of planetary importance

by

Xu Li

A dissertation submitted to the graduate faculty

in partial fulfillment of the requirements for the degree of

DOCTOR OF PHILOSOPHY

Major: Physical Chemistry

Major Professor: Cheuk-Yiu Ng

Iowa State University

Ames, Iowa

1996

Graduate College

Iowa State University

This is to certify that the doctoral dissertation of

Xu Li

has met the thesis requirements of Iowa State University

Signature was redacted for privacy.

Major Professor

Signature was redacted for privacy.

For the Major Program

Signature was redacted for privacy.

For the Graduate College

TABLE OF CONTENTS

ACKNOWLEDGEMENTS

During my five-year graduate study here at Iowa State University I have been helped by a lot of people. To all of whom I feel very thankful. But here I only mention a few I feel particularly indebted.

I can't thank Professor Cheuk-Yiu Ng enough for his encouragement, understanding and support through out my years here. I learned from him not only chemistry-in a broader sense, science-but also many many inspiring experiences that he shared with us. These experiences had a larger influence on my personal life as a young man who strived to understand science and his own destiny. Dr. Ng's sincerity, motivation, good attitude made it all easier. His constant support and encouragement has made my graduate study which leads to this thesis possible.

A special thank-you is due to Jerry Flesch who helped me from day one to settle me in. He helped me in more ways than I know of. We have been co-workers and friends for my entire graduate years, during which I had the privilege to know Jerry both as a scientist and as a genuinely good man. He is a very good experimentalist and teacher with many experiences and knowledge which he never hesitated to share with me. I wouldn't have achieved as much had there not been Jerry's always readily available helping hands and patience. He is also a caring and loving husband, father and grandfather. His way of treating other people had great impact on my own personal life. To him I'm forever indebted.

I also acknowledge the Chemistry Machine Shop crew of Eldon Ness, Terry Soseman and Dick Egger for their prompt service. Their work is recognized and valued. In the same way, I thank the people in the Metals Development Building Electronic Shop for their fine service. Their ideas and help had made the automation project successful.

I also appreciate the friendship of Chu-Xong Liao, Chung-Lin Liao, Chia-Wei Hsu, Yulin Huang, Yu-Ju Chen, Stephanie Stimson and Tom Fenn. Yulin Huang had been my colleague for more than a year. His motivation and hard-working influenced me. Stephanie has been working with me for the past couple of years. She is a fun and intelligent person to work with and always has some idea to solve a particular problem.

I thank my parents and brother for their encouragement and support that helped me through these years. Their letters and phone calls never failed to cheer me up when I was down. They were always there when I needed them. I couldn't have been what I'm today had they not sacrificed their own lives. To them all I have is love.

Finally, special thank goes to my very close friend and fiancee Caijiao Zhao who for the last two years had been the light of my life. I can't thank her enough for all the things she had done for me. It was always a great relief to have a nice dinner ready for me after coming home from a very rough day. Her whole-hearted support and care had made my thesis work much easier.

I acknowledge the Ames Lab, operated for the US DOE by Iowa State University, and the Iowa State University Chemistry Department for supporting me and this research. This work was performed at the Ames Laboratory under the U.S. Department of Energy.

GENERAL INTRODUCTION

Dissertation Organization

This dissertation consists of five chapters and an Appendix. Chapters I-V are each an independent paper and are preceded by a General Introduction chapter and followed by a Genaral Conclusion chapter. Each paper is in the format ready for publication and contains a brief abstract, an introduction, experiment, data analysis (if any) and conclusion. The tables, figures, and references mentioned in each chapter pertain only to that chapter. The references cited in each chapter are listed after the conclusion of each chapter. The Appendix explains the development of the computer programs used for data acquisition and instrumental control.

Introduction

Metastable species existing in planetary atmospheres are produced mostly by solar ultraviolet and electron impact dissociation and ionization processes. Through chemical interactions, these energetic species influence the concentrations and temperatures of electron, ion and neutral molecules. Quantitative in situ and laboratory measurements of rate constants and cross sections for reactions involving relevant metastable species are of importance for modeling the reaction cycles and predicting ion densities in planetary atmosphere.

The O^+ ions formed by solar VUV photoionization of O atoms are the most abundant ions in the F-region of the Earth's ionosphere. Thus the reactions involving $O^+(^4S,^2D,^2P)$ and N_2, O_2, CO_2, H_2, CO and H_2O are the most important set of reactions in the Earth's

ionosphere and also the atmospheres of Mars and Venus where CO_2 is the dominant constituent. Measuring the integral cross sections for these ion-molecule reactions will enable us to predict the ion densities, reaction channels, reaction kinetics and dynamics in the upper atmosphere where interactions with the magnetic field of the Earth and telecommunication radio signals occur. Furthermore, the reactions between $O^+(^4S,^2D,^2P)$ and organosulfuric compounds such as CH_3SH, CH_3SCH_3, CH_3CH_2SH, CH_3SSCH_3 are of atmospheric importantce since these compounds are combustion exhausts and major air pollutants. Knowing the kinetics of these reactions will help us understand the influences of these processes on the condition of the atmosphere.

Absolute total cross sections for ion-molecule reactions vary with the initial electronic state of the ion and collision energies between the ion and molecule of interest. $O^+(^2D)$ and $O^+(^2P)$ are the excited states ions which lie 3.32 and 5.02 eV above the ground $O^+(^4S)$, respectively. The reactions involving $O^+(^2D)$ and $O^+(^2P)$ are interesting since they not only bring in extra energy for the above mentioned reactions but also different multiplicities that may play an important role in those reactions. The collision energy of ion-molecule reactions can arrange from thermal energy to well above 10eV. Collision processes in the low energy region are very important in understanding the ion chemistry of the ionosphere because of the predominance and also the very high cross-sections of these processes. However, there are also many circumstances where higher collision energy situations prevail. For example, some high-energy O^+ ions, born in the ion sheath of Venus, are believed to penetrate into the atmosphere of Venus. Thus the full range collision energy study is warranted.

Using the unique triple-quadrupole double-octopole(TQDO) photoionization and electron-impact apparatus developed in our laboratory, we were able to measure the absolute state-selected ion-molecue reactions involving $O^+(^4S,^2D,^2P)$ and many other neutral molecules of importance in the ionosphere over a collision energy range from near thermal energy to above 10eV. The reactions involving $O^+(^4S)$ have already been extensively studied by array of different experimental methods. In our studies, we obtained cross-sections from scattering experiments and found good agreement with other people's results. We also have developed a simple method to isolate $O^+(^2D)$ and $O^+(^2P)$ so we can have state-selected reactions of $O^+(^2D)$ and $O^+(^2P)$ with neutral molecules, which has never been achieved before. Because of the nature of our TQDO apparatus, the kinetic energy spread of the prepared ions is around 1eV, which is not good enough for the study of low-energy ion-molecule collision processes. We have developed a differential retarding potential method for improving the kinetic energy resolution. With this method, we were able to study the cross sections for reactions with collision energy below 0.1eV.

Since many ion-molecule reactions involve secondary reactions given the nature of the scattering cell methodology, which tend to skew the cross section data for the primary reaction processes, we have to find a way to eliminate as much secondary reactions as possible. Generally this can achieved by lowering the pressure of the neutral gas sufficiently. But circumstances arise that the secondary reactions are so dominating that even at extremely low pressure in the scattering cell we still see a lot of the secondary ions. For these situations, we are incorporating the ability of doing pulsed cross beam study into the existing TQDO

apparatus. By pulsing the neutral gas to cross the ion beam perpendicularly and using differential pumping scheme, we should be able to remove the background neutral gas pressure hence the secondary reactions.

The data acquisition of the original TQDO apparatus was accomplished by a PDP-11 computer system developed about ten years ago. Besides of the fact that this system is old and crashes from time to time, it does not have the capability of controlling the voltages of the electrostatic lens system. Therefore it becomes very tedious to implement the differential retarding potential method which involves changing the voltages of certain electrostatic lenses during the data acquisition process. Furthermore, this computer system can not synchronize the action of the pulse valve with the data acquisition process which makes it unsuitable for the pulsed cross-beam study. All these call for a modern PC-based system for automatic control, manipulation, data acquisition and analysis. We have been able to utilize the latest development both in plug-in data acquisition board and in window software to develop our own control and acquisition system based on a Pentium PC. This system is posed to give us automatic hardware control and faster data acquisition and analysis. It is a great experiment of the leap from the old stand-alone instrumentation methodology that has been dominating the scientific research society as well as many of the industrial processes. Especially in today's computer revolution age, scientists should exploit the enormous information handling capability of personal computers well beyond mere scientific computing.

CHAPTER I

STATE SELECTION OF $O^+(^4S,^2D,^2P)$ USING RESONANCE DISSOCIATIVE CHARGE TRANSFER OF $He^+(Ne^+, Ar^+) + O_2$ AND RADIO FREQUENCY MULTIPOLE ION GUIDE TECHNIQUES

A paper submitted to Review Scientific Instruments

X. Li, Y.-L. Huang, G. D. Flesch, and C. Y. Ng

Abstract

By controlling the collision energies for dissociative charge transfer collisions of He^+ (Ne^+, Ar^+) + O_2 in a radio frequency (RF) octopole ion guide gas cell, and by applying appropriate effective ion trapping potentials to the RF octopole ion guide, we show that state-selected $O^+(^4S^\circ)$, $O^+(^2D^\circ)$, and $O^+(^2P^\circ)$ reactant ion beams with high purities and usable intensities can be prepared for scattering experiments. This experimental scheme, which makes possible the enrichment of an ionic species with a lower kinetic energy distribution in an RF multipole ion guide, should be useful for state-selection of other excited atomic ions by using appropriate dissociative charge transfer or dissociative photoionization processes.

I. Introduction

State-selected and state-to-state ion chemistry have played an important role in our fundamental understandingof elementary bimolecular ion-molecule collision dynamics.[1-3] The

progress in state-selected ion chemistry depends on the development of experimental techniques for state-selection of reactant ions. The formation of reactant ions in their ground states can be achieved when one of a variety of ionization methods is followed by collisional relaxation in a flow tube[4] or in a supersonic beam[5]. Due to a finer control of ionization energy, photoionization is preferred over electron impact ionization for the preparation of state-selected ions from neutral precursors.[6,7] However, a photoionization ion source, which requires high photon intensities in the ultraviolet (UV) or vacuum ultraviolet (VUV), is usually more expensive than an electron impact ionization ion source.

The O^+ ions formed by solar VUV photoionization of O atoms are the most abundant ions in the F-region of the Earth's ionosphere,[8] with the branching ratios for $O^+(^4S°)$: $O^+(^2D°)$: $O^+(^2P°) \approx 0.43 : 0.29 : 0.28$.[9-12] Since the $O^+(^2D°)$ and $O^+(^2P°)$ states are metastable with lifetimes of 3.57 hr and 4.47 s, respectively, the ion-molecule reactions involving $O^+(^4S°,^2D°,^2P°)$ and atmospheric gases constitute the most important set of reactions in the ionosphere of Earth.[13-16] Similarly, ion-molecule reactions involving $O^+(^4S°,^2D°,^2P°)$ play an important role in modeling the ionosphere chemistry of other planets such as Mars and Venus.[17] The chemistry of $O^+(^4S°)$ has been investigated extensively.[18] However, absolute cross sections for ion-molecule processes involving $O^+(^2D°)$ and $O^+(^2P°)$, which are 3.32 and 5.02 eV above the ground $O^+(^4S°)$ state,[19] respectively, have not been examined directly.

The recent increase in activity in state-selected ion chemistry is attributable to the development of sophisticated ionization schemes, including photoelectron-photoion coincidence (PEPICO)[20] and VUV or UV multiphoton laser ionization techniques.[21,22] In principle, the formation of O^+ ions in an excited state can be made by the photoionization of O atoms using laser or PEPICO schemes.[23] However, because of the difficulty in the formation of transient O atoms with high intensity, the preparation of an excited O^+ reactant ion beam in the pure $O^+(^2D°)$

or $O^+(^2P°)$ state with a usable intensity for scattering experiments still cannot be easily achieved.

In this report, we present an experimental scheme for the preparation of O^+ reactant ions in the selected $O^+(^2P°)$ or $O^+(^2D°)$ or $O^+(^4S°)$ state. This scheme combines the dissociative charge transfer reactions,

$$He^+ + O_2 \rightarrow O^+(^4S°, {}^2D°, {}^2P°) + O(^3P, {}^1D, {}^1S) + He, \quad (1)$$

$$Ne^+ + O_2 \rightarrow O^+(^4S°, {}^2D°) + O(^3P) + Ne, \quad (2)$$

$$Ar^+(^2P_{3/2,1/2}) + O_2 \rightarrow O^+(^4S°) + O(^3P) + Ar, \quad (3)$$

and the radio frequency (RF) octopole ion trap technique. The branching ratios for the formation of $O^+(^4S°)$, $O^+(^2D°)$, $O^+(^2P°)$ by reaction (1) have been measured as a function of collision energy in great detail in previous crossed-beam[24] and RF octopole ion guide[25,26] experiments. The formation of $O^+(^2D°)$ and $O^+(^4S°)$ by reactions (2) and (3), respectively, is endothermic. In previous experiments[27,28] in our laboratory, we have demonstrated that $O^+(^2D°)$ and $O^+(^4S°)$ can be produced efficiently by these reactions at collision energies above their respective thermochemical thresholds. The O^- ions produced by reaction (3) have been found predominantly in the $O^+(^4S°)$ ground state.[28] Here, we show that state-selected $O^+(^4S°)$, $O^+(^2D°)$, and $O^+(^2P°)$ reactant ions, prepared by reactions (1)-(3) at appropriate collision energies and RF trapping conditions of the octopole ion guide, are of sufficiently high purities and intensities for performing absolute total cross section measurements. The experimental scheme described here is expected to be applicable for the preparation of other excited atomic ions.

II. Experimental Considerations

The triple quadrupole-double octopole (TQDO) apparatus[6,7] is used to demonstrate the preparation of reactant $O^+(^4S°)$, or $O^+(^2D°)$, or $O^+(^2P°)$ ions and to perform absolute total cross

section measurements for ion-molecule reactions involving these ions. The principles and procedures for state-selected and state-to-state absolute cross section measurements using the TQDO apparatus have been described in detail previously.[28-33] Figure 1 shows the schematic diagram for the TQDO ion-molecule reaction apparatus. The TQDO apparatus essentially consists of, in sequential order, a vacuum ultraviolet (VUV) photoionization ion source or an electron impact ionization ion source (1), a reactant quadrupole mass spectrometer (QMS) (5), a lower radio frequency (RF) octopole ion guide reaction gas cell (RFOIGGC) [(6) + (7)], a middle QMS (10), an upper RFOIGGC [(11) + (14)], a product QMS (15), and a Daly-type scintillation ion detector[34] [(17) + (19) + (20)]. The electron ionization ion source used here is of the Brink design[35] and has been added to the TQDO apparatus recently. The TQDO apparatus is partitioned into five chambers which are separately evacuated by liquid nitrogen- or freon-trapped diffusion pumps. The differential pumping arrangement is important for the reactant ion preparation scheme and the cross section measurement experiments described here. Readers are referred to previous publications[6,7] for the details of this arrangement.

The application an RF octopole field as an ion guide for absolute cross section measurements, pioneered by Teloy and Gerlich,[36] has recently been reviewed in detail by Gerlich.[26] An electric multipole structure with $2n$ poles is formed by $2n$ rods symmetrically spaced on an inscribed circle. The inner tubular diameter of the octopole, defined by the inner surfaces of the rods, is $2r_o$. The principle of the RF electric multipole field with $2n$ poles for trapping and guiding ions (charge = q, mass = m) is based on the fact that with a sufficiently high RF field (amplitude = V_o) and an appropriate frequency (ω), a sufficiently high effective potential [$V_{eff}(r)$] is established to confine the ions. Within the limit of certain operating conditions, the expression for V_{eff} can be shown as

$$V_{eff}(r) = n^2 [(q^2 V_o^2)/(4 m \omega^2 r_o^2)] (r/r_o)^{2n-2}. \quad (4)$$

Figure 1 Schematic of the tandem mass spectrometer arrangement for absolute total cross section measurements. (1) electron impact ionization ion source, (2) atomic or molecular nozzle beam, (3) to freon-trapped 6" diffusion pump (DP), (4) to liquid-nitrogen (LN_2)-trapped 6" DP, (5) reactant QMS, (6) lower RF octopole ion guide, (7) lower RFOIGGC, (8) to LN_2-trapped 6" DP, (9) the lower RF octopole ion guide chamber, (10) middle QMS, (11) upper RF octopole ion guide, (12) to LN_2-trapped 4" DP, (13) upper RF octopole ion guide chamber, (14) upper RFOIGGC, (15) product QMS, (16) detector chamber, (17) plastic scintillator window, (18) to LN_2-trapped 2" DP, (19) photomultiplier tube, (20) aluminum ion target.

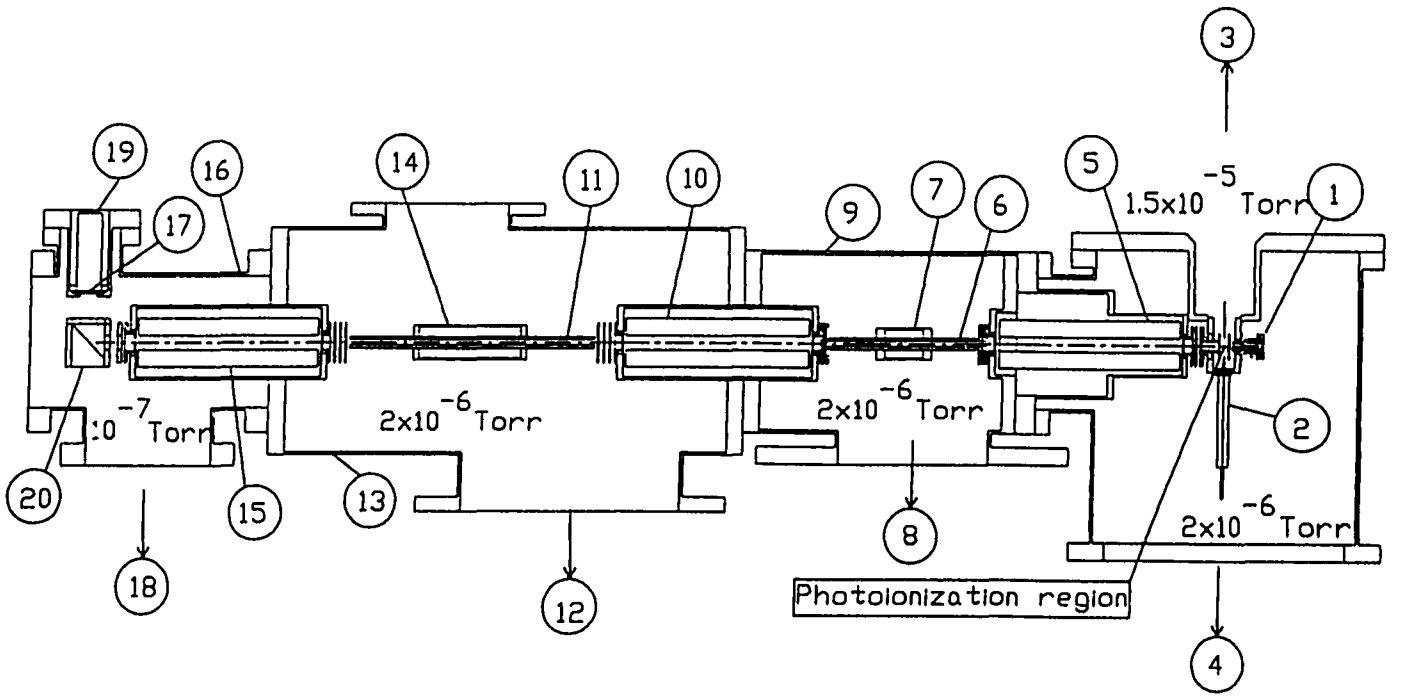
3
19
16
14
11
10
9
7
6
5
1.5x10 -5 Torr
1
17
2x10 -6 Torr
2x10 -6 Torr
2
20
15
13
8
2x10 -6 Torr
18
12
Photoionization region
4

For an electric octopole, $n = 4$,

$$V_{eff}(r) = 4\,[(q^2 V_o^2)/(m\,\omega^2 r_o^2)]\,(r/r_o)^6. \qquad (5)$$

This potential is close to a square well, providing a tubular trapping volume with a low potential near the center and a rapidly increasing potential wall near the poles.[37]

An ion formed with kinetic energy acquired in an ion-molecule collision process in an RFOIGGC can be trapped radially and guided to the detector with a near 100% ion collection efficiency when appropriate values of V_o and ω are applied to the RF octopole ion guide. This is the principle for absolute total cross section measurements of ion-molecule reactions using the (reactant) QMS-(upper) RFOIGGC-(product) QMS arrange-ment when reactant ions are prepared by VUV ionization or electron impact ionization.

In this experiment, He^+ (Ne^+, Ar^+) ions formed by electron impact ionization at an electron energy of ≈ 80 eV are extracted and mass-selected by the reactant QMS before reacting with O_2 in the lower RFOIGGC. State-selected $O^+(^4S°, ^2D°, ^2P°)$ ions prepared by reactions (1), (2), and (3) in the lower RFOIGGC (using the procedures described below) are mass-selected by the middle QMS and are further guided into the upper RFOIGGC to react with neutral reactants of interest. The intensities for the reactant O^+ and the product ions formed in the upper RFOIGGC are measured using the product QMS and the ion detector and allow the calculation of absolute total cross sections of the ion-molecule reaction of interest. Thus, absolute total cross section measurements of ion-molecule reactions involving $O^+(^4S°, ^2D°, ^2P°)$ prepared by reactions (1), (2), and (3) fully utilize the QMS-RFOIGGC-QMS-RFOIGGC-QMS arrangement.

Since $V_{eff}(r)$ for a quadrupole field (n =2) is proportional to $(r/r_o)^2$, compared to $(r/r_o)^6$ for a octopole field, the kinetic energy resolution achieved for ion-molecule collisional studies using

an RF octopole (or higher multipoles) ion guide reaction gas cell is better than that using an RF quadrupole reaction gas cell. For this reason, an RFOIGGC is preferred over an RF quadrupole reaction gas cell for absolute total cross section measurements of ion-molecule processes. However, for the application described here, an RF quadrupole can be used in place of an RF octopole ion guide.

The principle ultilized here to form an O^- ion beam in the nearly pure $O^-(^2P°)$ [or $O^-(^2D°)$] state is based on the fact that $O^-(^2P°)$ [$O^-(^2D°)$] ions formed by reaction (1) [reaction (2)] in the lower RFOIGGC possess lower kinetic energies than those for $O^-(^2D°,^4S°)$ [$O^-(^4S°)$] ions. By choosing appropriate V_o and ω values applied to the lower RF octopole ion guide, $O^-(^2D°,^4S°)$ [$O^-(^4S°)$] ions formed with higher kinetic energies can be released, whereas $O^-(^2P°)$ [$O^-(^2D°)$] ions with lower kinetic energies are collected and guided towards the middle QMS. We note that using this scheme a finite fraction of unwanted $O^-(^2D°,^4S°)$ [$O^-(^4S°)$] ions originally scattered along the lower RF octopole ion guide are expected to come through the ion guide together with the trapped $O^-(^2P°)$ [$O^-(^2D°)$]. However, assuming that O^- product ions are scattered isotropically,[38] the number of unwanted $O^-(O^-(^2D°,^4S°)$ [$O^-(^4S°)$] ions is small, estimated from the solid angle sustained by the exit of the octopole. For the lower RF octopole (r_o = 0.5 cm, length of rods = 18 cm) used in this experiment, a fraction[39] of $\leq$ 0.16% of the total $O^-(^2D°,^4S°)$ or [$O^-(^4S°)$] ions originally produced by reaction (1) [reaction (2)] is expected to be transmitted as impurity reactant ions.

A. Preparation of $O^-(^2P°)$

Previous experiments indicate that charge transfer product O_2^- represents only a minor fraction (< 1%) of total products for the collision of He^- + O_2 over the collision energy range of 0.5-200 eV.[24-26,40] Since the recombination energy for He^- [RE(He^-)] is 24.586 eV,[19] the energetically allowed product channels of reaction (1) are: I: $O^-(^4S°)$ + $O(^3P)$, II: $O^-(^4S°)$ +

$O(^1D)$, III: $O^+(^2D^\circ) + O(^3P)$, IV: $O^+(^4S^\circ) + O(^1S)$, V: $O^+(^2P^\circ) + O(^3P)$, and VI: $O^+(^2D^\circ) + O(^1D)$. The heats of reaction (ΔE) for these Channels are given in Table I.[41] The labels of Channels I-VI are those given by Bischof and Linder.[24]. In their crossed-beam study of reaction (1), the kinetic energy distribution of product O^- was measured as a function of scattering angle. All kinetic energy spectra of O^- consist of essentially four resolved kinetic energy peaks. Based on their careful analysis of the scattering data, the four peaks in decreasing order of kinetic energy are assigned to product Channels I, II, III and V, respectively. Note that Channels I and II produce O^- in the $^4S^\circ$ ground state, whereas Channels III and V yield O^- in the $^2D^\circ$ and $^2P^\circ$ states, respectively. Bischof and Linder have obtained angle-integrated branching ratios for Channels I, II, III, and V.[24] The branching ratios for Channels I-V determined in a more recent investigation by Scherbarth and Gerlich[25,26] using the radio frequency (RF) octopole ion guide technique are consistent with those of the crossed-beam experiment.

Since this article concerns the state selection of O^-, it is appropriate to summarize the experimental and theoretical arguments leading to the determination of the branching ratios for Channels I-V. Bischof and Linder conclude from their crossed-beam study that two near resonance charge transfer mechanisms are responsible for the population of excited O_2^{-*} intermediate states, which subsequently dissociate to form products, $O^- + O$. The predissociation of O_2^- in the $c^4\Sigma_u^-(v'=0)$ state populated by a long-range energy-resonant charge transfer mechanism is responsible for the formation of Channels I and II. This mechanism is relatively unimportant at low collision energies, but increases markedly as the collision energy is increased. The $O_2^-[c^4\Sigma_u^-(v'=0)]$ has been determined spectroscopically to lie 24.465 eV above the ground O_2 state.[42,43] The latter value is lower than $RE(He^-)$ by 0.121 eV. The $O_2^-(c^4\Sigma_u^-)$ state has been shown theoretically to be quasibound with a low potential barrier just sufficient to

Table I. Energetics of possible product channels for the dissociative charge transfer reactions, $He^+(Ne^+, Ar^+) + O_2 \rightarrow O^+ + O + He$ (Ne, Ar).

Reactions		Product channels[a]	ΔE (eV)[b,c] (eV)	Expected $E_{cm}(O^-)$[d]
$He^- + O_2$	**I:**	**$O^+(^4S°) + O(^3P)$**	-5.86	2.93
	II:	**$O^+(^4S°) + O(^1D)$**	-3.89	1.95
	III:	**$O^+(^2D°) + O(^3P)$**	-2.54	1.27
	IV:	$O^+(^4S°) + O(^1S)$	-1.67	0.84
	V:	**$O^+(^2P°) + O(^3P)$**	-0.84	0.42
	VI:	$O^+(^2D°) + O(^1D)$	-0.57	0.29
$Ne^- + O_2$	I′:	$O^-(^4S°) + O(^3P)$	-2.84 (-2.94)	...
	II′:	$O^-(^4S°) + O(^1D)$	-0.87 (-0.97)	...
	III′:	$O^-(^2D°) + O(^3P)$	0.48 (0.38)	...
	IV′:	$O^-(^4S°) + O(^1S)$	1.35 (1.25)	...
	V′:	$O^-(^2P°) + O(^3P)$	2.18 (2.10)	...
$Ar^- + O_2$	I":	$O^-(^4S°) + O(^3P)$	2.97 (2.79)	...
	II":	$O^-(^4S°) + O(^1D)$	4.94 (4.76)	...
	III":	$O^-(^2D°) + O(^3P)$	6.29 (6.11)	...

a) The label of Channel I-VI for the $He^- + O_2$ reaction is given by Bischof and Linder. The channels in bold letters are identified as major products in the crossed-beam experiment. See Ref. 24.

b) The heats of reactions (ΔE) are calculated using: $RE(He^-) = 24.586$ eV; $RE[Ne^-(^2P_{3/2})] = 21.564$ eV; $RE[Ne^-(^2P_{1/2})] = 21.661$ eV; $RE[Ar^-(^2P_{3/2})] = 15.760$ eV; $RE[Ar^-(^2P_{1/2})] = 15.937$ eV: $\Delta H°_{f0}[O^-(^4S°)] = 373.0$ kcal/mol; $\Delta H°_{f0}[O^-(^2D°)] = 449.6$ kcal/mol; $\Delta H°_{f0}[O^-(^2P°)] = 488.8$ kcal/mol; $\Delta H°_{f0}[O(^3P)] = 59.0$ kcal/mol; $\Delta H°_{f0}[O(^1D)] = 104.4$ kcal/mol; and $\Delta H°_{f0}[O(^1S)] = 155.6$ kcal/mol. See Refs. 19 and 41.

c) The values in parentheses are calculated assuming $Ne^-(^2P_{1/2})$ and $Ar^-(^2P_{1/2})$ reactant ions are involved in Reactions (2) and (3), respectively.

d) The expected E_{cm} for O^- is predicted by the two-step near resonant charge transfer-dissociation mechanism proposed by Bischof and Linder (Ref. 24).

support two vibrational levels.[44] Tunneling through the barrier is proposed to be the main predissociation mechanism. The comparison of the branching ratios for channel I : Channel II obtained in the crossed-beam[24] and PEPICO[45-47] experiments supports the long-range charge transfer mechanism for the population of $O_2^-[c^4\Sigma_u^-(v'=0)]$.

The formation of Channels III and V is attributed to excitation to the repulsive part of the $O_2^-[(III)^2\Pi_u]$ state in the Franck-Condon region slightly below the $O_2^-(c^4\Sigma_u^-)$ state.[24] This slightly exothermic charge transfer mechanism, which is responsible for the production of $O^-(^2P^\circ)$, is found to be dominant at low collision energies with the exothermicity dependent on collision energy. At a center-of-mass collision energy (E_{cm}) of 0.5 eV, the exothermicity is 0.6 eV.

In accord with the two-step charge transfer-dissociation reaction model, the experimental branching ratio measurements [see Fig. 12(a) and 12(b) of Ref. 24 or Fig. 74 of Ref. 26] indicate that Channels III and V are the dominant processes at $E_{cm} \leq 1$ eV with branching ratios of ≈ 60% and ≈23%, respectively. Channel V decreases rapidly to a branching ratio of ≈ 40% as the collision energy is increased to 3 eV, followed by a gradual decrease to ≈ 27% at 200 eV, whereas the branching ratio for Channel III decreases gradually throughout the collision energy range of 0.5-200 eV to a value of ≈ 12% at 200 eV. The sum of the branching ratios for Channels I and II increases from ≈ 7% to ≈ 37% at 3 eV. At collision energies > 3 eV, the sum of the branching ratios for Channels I and II increases gradually to ≈ 50% as the collision energy is increased to a value of 200 eV.

The conclusion of negligible formation of Channels IV and VI is in accord with the observed kinetic energy spectra of O^- and previous experimental[45-47] and theoretical[44,48] information concerning the predissociation of excited O_2^- states. Channels IV and VI are not found in the PEPICO studies of O_2.[45-47] We note that a small peak at near zero kinetic energy observed in the O^- kinetic energy spectrum has not been assigned. The intensity of this peak is

small, < 5% of that of Channel V, at E_{cm} of 1-3 eV. This small channel, which is labeled as Channel "0" by Bischof and Linder,[24] is found to increase in significance at higher collision energies.

The two-step near-resonant charge-transfer-dissociation model for reaction (1) predicts that the kinetic energies for O^+ associated with Channels I-VI are approximately equal to half of the corresponding ΔE values (see Table I).[24] The experimental O^+ kinetic energy peaks assigned to Channels I, II, III, and V are only slightly shifted with respect to these predicted E_{cm} values because of the finite exothermicity of the charge transfer processes, depending on the collision energy of reaction (1). Assuming that the assignments of the kinetic energy peaks to Channels I, II, III, and V are correct, at approximately 2.93, 1.95, 1.27, and 0.42 eV, respectively, we can lower V_{eff} of the lower octopole to a value of $\leq$ 0.4 eV in order to lose radially the $O^+(^2D°,^4S°)$ ions produced in Channels I, II, III, and IV. Nevertheless, by using a sufficiently high V_{eff}, the majority of the $O^+(^2P°)$ ions are trapped for transmission to the middle QMS and then to the upper RFOIGGC for ion-molecule reaction studies. As pointed out above, a small fraction of $O^+(^2D°,^4S°)$ ions scattered along the octopole axis will also be transmitted as impurity reactant ions.

Since the production of $O^+(^2P°)$ by reaction (1) is strongly favored at low collision energies, we choose an E_{cm} value of 1.69±0.8 eV for the $He^* + O_2$ reaction in the lower RFOIGGC. According to the previous branching ratio measurements of Bischof and Linder,[24-26] the branching ratios [scaled from Figs. 12(a) and 12(b) of Ref. 24] for Channel I : Channel II: Channel III : Channel V are approximately 0.08 (0.10) : 0.18 (0.20) : 0.20 (0.27) : 0.52 (0.43). These amount to branching ratios for $O^+(^4S°) : O^+(^2D°) : O^+(^2P°) \approx 0.26$ (0.30) : 0.20 (0.27) : 0.52 (0.43). The branching ratios in parentheses [scaled from Fig. 74 of Ref. 26] are obtained by

Scherbarth and Gerlich using RF octopole ion guide techniques and are in reasonable accord with the crossed-beam results. Note that the branching ratios obtained by Bischof and Linder also include an unidentified channel "0", which amounts to 2-3% of O^- at E_{cm} = 1.69 eV.[24]

In order to investigate the state selection scheme described above, our approach has been to monitor the reactivities for $O^-(^4S°,^2D°,^2P°)$ with appropriate monitoring gases at specific collision energies in the upper RFOIGGC. A survey of the literature shows that the total cross section for the charge transfer reactions $O^- + N_2$ [reactions (6)-(8)] are relatively well known. At E_{cm} < 1.96 eV, the cross section for reaction (6) is zero,[18] whereas those for the exothermic charge transfer processes [reactions (7) and (8)] are high and are found to be the overwhelmingly dominant product channels.

$$O^-(^4S°) + N_2 \rightarrow N_2^- + O, \qquad \Delta E = 1.96 \text{ eV} \qquad (6)$$

$$O^-(^2D°) + N_2 \rightarrow N_2^- + O, \qquad \Delta E = -1.33 \text{ eV} \qquad (7)$$

$$O^-(^2P°) + N_2 \rightarrow N_2^- + O, \qquad \Delta E = -3.03 \text{ eV} \qquad (8)$$

Furthermore, in a recent PEPICO experiment[49] the cross sections for reactions (7) and (8) are shown to be different in the E_{cm} range of 5.5-14.7 eV. Because of this information, we have chosen reactions (6)-(8) as the monitoring reactions to be examined using the upper RFOIGGC. The absolute total cross section for N_2^- formation by the $O^- + N_2$ reaction with reactant O^- ions prepared by reaction (1) at E_{cm} = 1.69±0.8 eV has been measured as a function of V_o applied the lower RFOIGGC. For ω = 10.4 MHz, m = 16 amu for O^-, and r_o = 0.5 cm used in our experiment, the V_{eff} values for corresponding V_o's can be calculated by equation 5. Unless otherwise specified, the V_{eff} values given below are calculated with r/r_o = 1.

Since we are only interested in trapping $O^-(^2P^\circ)$, which has a kinetic energy distribution peaked at 0.4 eV, we begin to examine the trapping efficiency at V_{eff} = 1.53 V. Figure 2 depicts a typical plot of $I(N_2^-)/I(O^+)$ versus $I(O^-)$ trapped by the lower RFOIGGC, where $I(N_2^-)$ and $I(O^+)$ are the respective intensities for product N_2^- and reactant O^-. We note that $I(N_2^-)/I(O^-)$ is proportional to the total cross section for N_2^+ formation by the $O^+ + N_2$ reaction in the upper RFOIGGC. The $I(O^+)$ value depends on and is a measure of V_{eff} applied to the lower RFOIGGC. Since the relationship between $I(O^-)$ and V_{eff} is not linear, the $I(O^+)$ scale cannot be directly translated into the V_{eff} scale. In order to assist the discussion below, we have marked several corresponding V_{eff} values on the horizontal axis of Fig. 2. The plot of Fig. 2 reveals that the N_2^- total cross section increases when V_{eff} is decreased, an observation consistent with our expectation. As V_{eff} is reduced from 1.53 to 0.51 V and to 0.25 eV, we find that the intensity for O^- formed in the lower RFOIGGC decreases to 70% and 40%, respectively, of the original intensity (100%) at V_{eff} = 1.53 V. The absolute total cross section observed for N_2^- at V_{eff} = 1.53 V [$\sigma(N_2^-|1.53\ V)$] is 38±2 Å^2, as compared to 44±4 Å^2 at V_{eff} = 0.25 V [$\sigma(N_2|0.25\ V)$]. The N_2^- cross section is found to remain constant as V_{eff} is further decreased from V_{eff} = 0.25 V. Here, the absolute cross sections for N_2^- at V_{eff} [$\sigma(N_2^-|V_{eff})$] are calculated using the relation: $\sigma = (nl)^{-1}$ [$I(N_2^-|V_{eff})/I(O^-|V_{eff})$], where n is the number density of N_2, l is the length of the upper RFIGGC, and $I(N_2^-|V_{eff})$ and $I(O^-|V_{eff})$ are the N_2^- and O^- intensities observed at V_{eff} applied to the lower RFIGGC. The N_2^- cross sections due to the difference of O^- trapped at V_{eff} = 0.51 V and V_{eff} = 1.53 V [$\sigma(N_2^-|1.53\text{-}0.51\ V)$] and that at V_{eff} = 0.25 V and V_{eff} = 0.51 V [$\sigma(N_2^-|0.51\text{-}0.25\ V)$] are calculated to be 25±2 and 40±4 Å^2, respectively. The values for $\sigma(N_2^-|1.53\text{-}0.51\ V)$ and

$\sigma(N_2^+|0.51\text{-}0.25\ V)$ are calculated as: $(nl)^{-1}$ $[I(N_2^+|0.51\ V) - I(N_2^+|1.53\ V)]/[I(O^-|0.51\ V) - I(O^-|1.53\ V)]$ and $(nl)^{-1}$ $[I(N_2^+|0.25\ V) - I(N_2^+|0.51\ V)]/[I(O^+|0.25\ V) - I(O^-|0.51\ V)]$, respectively. The comparisons of these cross sections are summarized in Table II. The increase in N_2^+ cross section can be attributed to the increase in purity of the $O^+(^2P°)$ reactant ions. At V_{eff} = 0.25 eV, nearly the maximum loss of $O^-(^4S°,^2D°)$ has been achieved and the purity of $O^-(^2P°)$ is close to its maximum.

Considering that the kinetic energy distributions for $O^+(^4S°)$ (Channel II) and V.$O^-(^2D°)$ are peaked at 1.95 and 1.27 eV, respectively, it may be surprising that a low V_{eff} value of 0.25 V is required to lose these unwanted ions. When $O^+(^4S°)$ (Channel II) or $O^-(^2D°)$ having a specific E_{cm} is scattered at an angle θ with respect to the axis of the octopole, the kinetic energy effective for surmounting V_{eff} is $E_{cm}\bullet\sin^2\theta$. Thus, even at V_{eff} = 0.25 V, a finite fraction of $O^-(^4S°)$ (Channel II) or $O^-(^2D°)$ scattered at $\theta < 21°$ or $\theta < 26°$ may remain trapped by the octopole. For too low a V_{eff}, an excessive fraction of $O^-(^2P°)$ ions may be lost. The experimental value of V_{eff} = 0.25 V is merely a compromise between the retention of $O^+(^2P°)$ and the release of unwanted $O^-(^4S°,^2D°)$. Assuming that $O^-(^2S°)$ $[O^-(^2D°)]$ ions scattering at $\theta > 21°$ $[\theta > 26°]$ are lost, the fraction of $O^-(^2S°)$ $[O^-(^2D°)]$ transmitted through the octopole ion guide is estimated to be 6% (9%).[39] The experimental kinetic energy distribution for $O^-(^2P°)$ (Channel V) is asymmetric and peaks at 0.3-0.4 eV[24,25] with a more gradual decrease towards lower kinetic energies. For V_{eff} = 0.25 V, the release of $O^+(^2P°)$ is estimated to be ≈ 50%. Thus, under the experimental conditions which maximize the relative transmitting fraction for $O^-(^2P°)$, we estimate that the relative intensities for $O^-(^4S°) : O^-(^2D°) : O^+(^2P°) \approx 0.05 : 0.06 : 0.89$. The latter

Figure 2 Plot of $I(N_2')/I(O')$ versus $I(O')$, where $I(N_2')$ and $I(O')$ are the intensities for the product N_2' (formed in the upper RFOIGGC by the reaction $O' + N_2$) and reactant O' (formed by reaction 1 in the lower RFOIGGC). The decrease of $I(O')$ is due to the lowering of V_{eff} applied to the lower RF octopole ion guide. The ratio $I(N_2')/I(O')$ is directly proportional to the total cross section for N_2'.

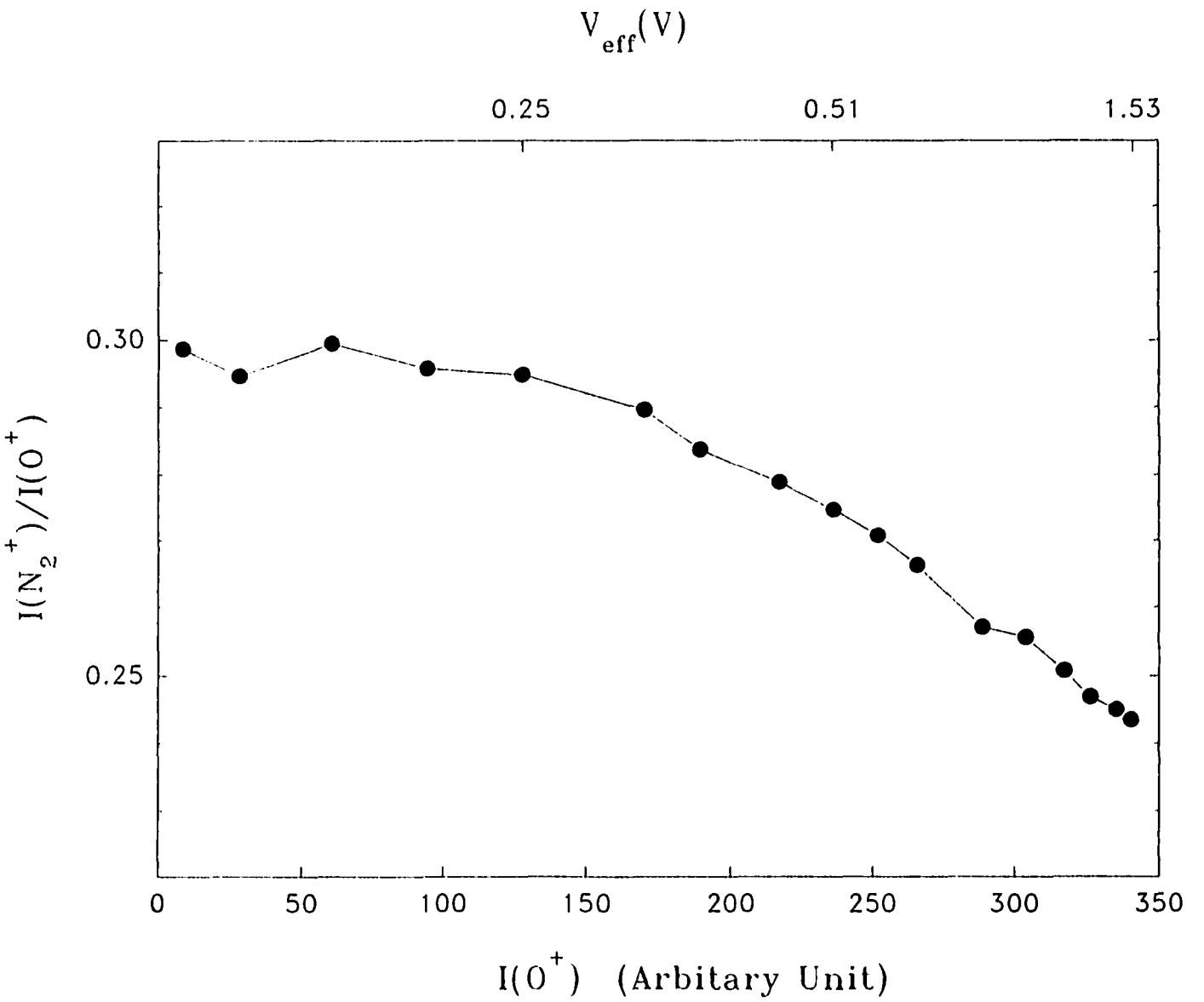
$V_{eff}(V)$
0.25
0.51
1.53
0.30
0.25
$I(N_2^+)/I(O^+)$
0
50
100
150
200
250
300
350
$I(O^+)$ (Arbitary Unit)

values are calculated using the branching ratios[24] of $O^+(^4S°) : O^+(^2D°) : O^+(^2P°) = 0.26 : 0.20 : 0.52$ for $O^-(^4S°,^2D°,^2P°)$ originally produced by reaction (1) at $E_{cm} = 1.69 \pm 0.8$ eV.

This above conclusion is based on a value of $V_{eff} = 0.25$ V (corresponding to $V_o = 33.5$ V) calculated using Eq. 5 with $r/r_o = 1$. However, in order to satisfy the adiabatic requirement for stable ion trajectories through the octopole, the turning radius of an ion r_c should be less than r_o (i.e., $r/r_o < 1$). Gerlich suggests an empirical rule for safe operation within the adiabatic approximation as $r_c/r_o < 0.8$ or $r_c < 0.8\ r_o$. For $r/r_o = 0.8$, the corresponding V_{eff} for $V_o = 33.5$ V is 0.066 V. If the maximum ion turning radius is $r_c = 0.8\ r_o$, we estimate that the fraction of $O^-(^4S°)$ [$O^-(^2D°)$] transmitted through the octopole becomes 1.2% (2.6%).[39] It is reasonable to believe that the actual fraction lies between 1.2 and 6% for $O^+(^4S°)$, and 2.6 and 9% for $O^-(^2D°)$. We note that the fraction of $O^-(^2P°)$ released for a trapping potential of 0.066 V is greater than that for 0.25 V.

B. Preparation of $O^+(^2D°)$

The recombination energy for Ne^- is $RE(Ne^-) = 21.564$ eV.[19] Thus, the ΔE values for the formation of Channel I′ [$O^-(^4S°) + O(^3P)$], Channel II′ [$O^-(^4S°) + O(^1D)$], Channel III′ [$O^-(^2D°) + O(^3P)$], Channel IV′ [$O^-(^4S°) + O(^1S)$], and Channel V′ [$O^-(^2P°) + O(^3P)$] by dissociative charge transfer collisions of $Ne^- + O_2$ are -2.84, -0.87, 0.48 eV, 1.35, and 2.18 eV, respectively (see Table I).[19,41] Branching ratios and the dynamics leading to formation of these channels have not been examined in detail. In a series of recent charge transfer experiments performed in our laboratory,[28,32,33,50] we have shown that product ions formed by dissociative photoionization may also be produced by endothermic dissociative charge transfer. In view of the efficient production of $O^-(^2D°) + O(^3P)$ and $O^-(^2P°) + O(^3P)$ by dissociative photoionization[45-47] and by dissociative charge

Table II. Absolute cross sections for N_2^+ formed by the $O^+ + N_2$ reaction at E_{cm} = 16 eV with O^+ prepared by reaction (1) in the lower RFOIGGC at E_{cm} = 1.69±0.8 eV and specific V_{eff} values.[a]

Reaction sequence[b]	$\sigma(N_2^-\|1.53\ V)$[c] (Å²)	$\sigma(N_2^-\|1.53\text{-}0.51\ V)$[d] (Å²)	$\sigma(N_2^-\|0.51\text{-}0.25\ V)$[e] (Å²)	$\sigma(N_2^-\|0.25\ V)$[f] (Å²)
$He^- + O_2/O^- + N_2$	38 ± 2	25 ± 2	40 ± 4	44 ± 3
$Ne^- + O_2/O^- + N_2$	30 ± 4	28 ± 4	28 ± 5	31 ± 5

a) The values for V_{eff} are calculated using $r/r_o = 1$. At V_{eff} = 0.51 and 0.25 V, the intensities for O^- reactant ions are ≈70% and ≈40%, respectively, of the intensity (100%) for O^- ions observed at V_{eff} = 1.53 eV.

b) The first reaction is used for preparing O^- reactant in the lower RFOIGGC and the second reaction is the probing reaction for examining the reactivity of O^- in the upper RFOIGGC.

c) Absolute total cross section for N_2^- formed in the charge transfer reaction of $O^- + N_2$ at V_{eff} = 1.53 V applied to the lower RF octopole ion guide. The value for $\sigma(N_2^-|1.53\ V)$ is calculated using the relation: $\sigma = (nl)^{-1}\,[I(N_2^-|1.53\ V)/I(O^-|1.53\ V)]$, where n is the number density of N_2, l is the length of the upper RFIGGC, and $I(N_2^-|1.53\ V)$ and $I(O^-|1.53\ V)$ are the N_2^- and O^- intensities observed at V_{eff} = 1.53 V applied to the lower RFIGGC.

d) Absolute total cross section for N_2^- characteristic of the difference of O^- reactant ions observed at V_{eff} = 1.2 and 0.51 V. The value for $\sigma(N_2^-|1.53\text{-}0.51\ V)$ is calculated as: $(nl)^{-1}\,[I(N_2^-|0.51\ V) - I(N_2^-|1.53\ V)]/[I(O^-|0.51\ V) - I(O^-|1.53\ V)]$. See footnote c.

e) Absolute total cross section for N_2^- characteristic of the difference of O^- reactant ions observed at V_{eff} = 0.51 and 0.25 V. The value for $\sigma(N_2^-|0.51\text{-}0.25\ V)$ is calculated as: $(nl)^{-1}\,[I(N_2^-|0.25\ V) - I(N_2^-|0.51\ V)]/[I(O^-|0.25\ V) - I(O^-|0.51\ V)]$. See footnote c.

f) Absolute total cross section for N_2^- formed in the charge transfer reaction of $O^- + N_2$ at V_{eff} = 0.25

transfer of $He^+ + O_2$,[24-26] we expect that these channels will also be formed efficiently by endothermic dissociative charge transfer collisions of $Ne^+ + O_2$. At $E_{cm} < 2.1$ eV, the formation of $O^-(^2P^\circ) + O(^3P)$ is not allowed energetically.[51]

Using $E_{cm} = 0.73 \pm 0.6$ eV, an energy above the ΔE value for Channel III′, we have shown previously that the formation of $O^-(^2D^\circ)$ is efficient,[27] in accordance with the endothermic dissociative charge transfer mechanism. By choosing $E_{cm} = 0.73 \pm 0.6$ eV for reaction (2), we also avoid the possible formation of Channel IV′.

Figure 3 shows the absolute total cross sections for O^+ formation by reaction (2) in the E_{cm} range of 0.06-2.35 eV.[52,53] The cross section for O^+ increases from 1.25 Å^2 at $E_{cm} = 0.06$ eV to a near constant value of 4.25 Å^2 at $E_{cm} = 0.4$ eV. Taking into account the experimental uncertainties, we interpret that this increase in cross section corresponds to the onset for the formation of $O^+(^2D) + O(^3P)$ ($\Delta E = 0.43$ eV).[54] This interpretation is also consistent with the conclusion that the cross sections for the formation of $O^+(^4S^\circ)$ (or Channels I′ and II′) are $\lesssim 1.25$ Å^2 at E_{cm}'s near the threshold of Channel III′. The PEPICO studies[45-47] of O_2 in the photon energy range of 20.29-20.93 eV, which corresponds to ionization transition to $O_2^+(B^2\Sigma_g^-, v=0\text{-}5)$, indicate that the formation of $O^-(^4S^\circ) + O(^1D)$ is minor with branching ratios < 0.10. It is conceivable that the formation of Channel II′ is also small compared to that of channel I′. Assuming that the kinetic energy assisted dissociative charge transfer mechanism operates for reaction (2), at $E_{cm} = 0.73 \pm 0.06$ eV we expect that the kinetic energy distribution of $O^-(^4S^\circ)$ associated with Channel I′ peaks at $1.42 \text{ eV} < E_{cm} < 1.79$ eV [$0.5\ (\Delta E + E_{cm})$, where $\Delta E = 2.84$ eV and $E_{cm} = 0.73 \pm 0.06$ eV]. The formation of $O^-(^2D^\circ)$ is most likely due to excitation to the repulsive part of the $O_2^-[(III)^2\Pi_u]$ state, which is adiabatically correlated to the $O^-(^2D^\circ) + O(^3P)$ asymptotic limit.

We have also examined the reactivity of O^- prepared by reaction (2) at $E_{cm} = 0.73 \pm 0.06$ eV as a function V_{eff} applied to the lower RF octopole ion guide. As shown in Table II, the values for $\sigma(N_2^-|1.53\text{ V})$, $\sigma(N_2^-|1.53\text{-}0.51\text{ V})$, $\sigma(N_2^-|0.51\text{-}0.25\text{ V})$, and $\sigma(N_2^-|0.25\text{ V})$ at $E_{cm} = 15.9$eV are observed to be 30±4, 28±4, 28±4, and 31±5 Å^2, respectively. Within the experimental uncertainties, the N_2^- cross sections for $V_{eff} < 0.25$ V are equal to that for $V_{eff} = 0.25$ V. These N_2^- cross sections are

Figure 3 Absolute total cross sections for O^+ formed by reaction (2) in the E_{cm} range of 0.06-2.6 eV measured using the differential retarding potential method (Ref. 52) with an Ne^+ ion beam kinetic energy spread of ±0.2 eV.

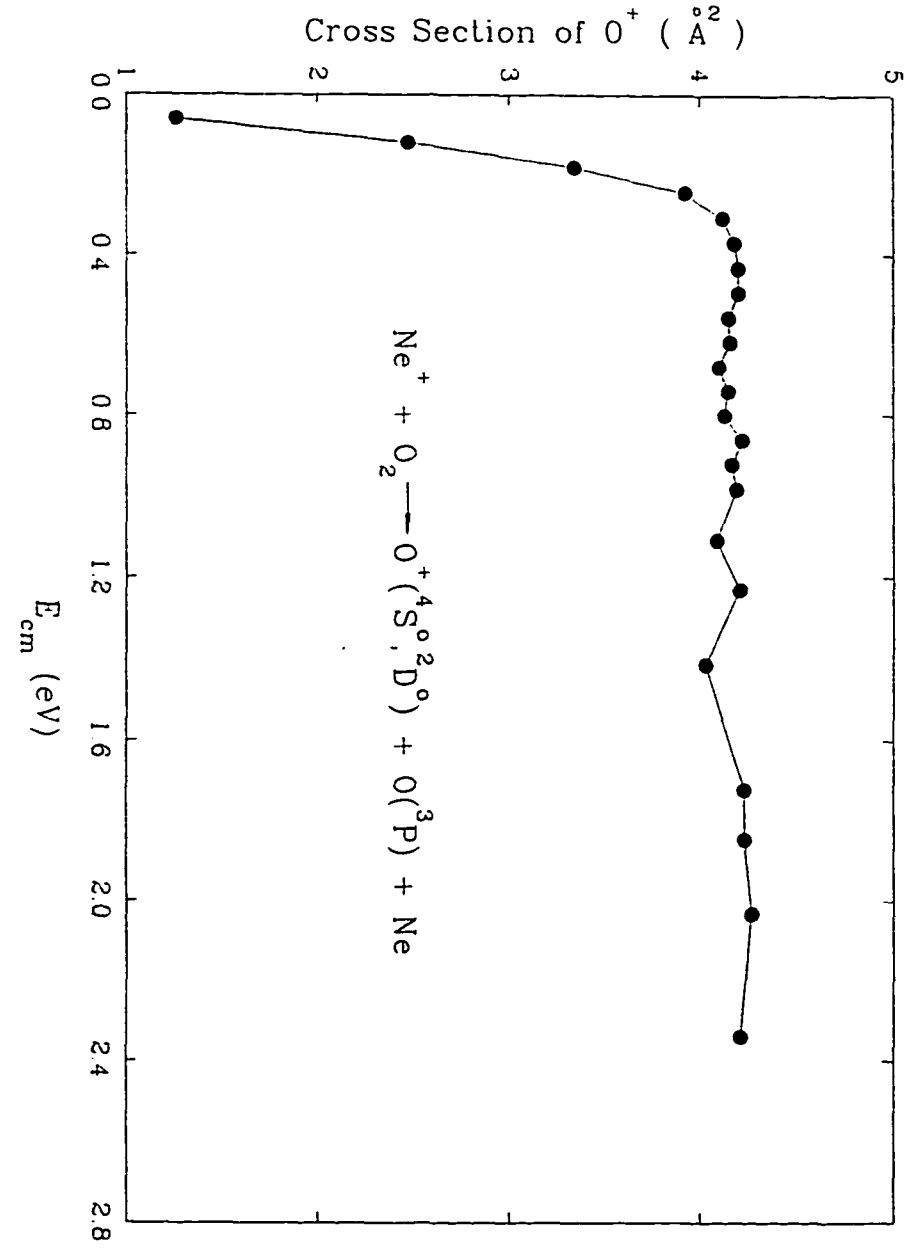
Cross Section of O^+ ($Å^2$)
1
2
3
4
5
0.0
0.4
0.8
1.2
1.6
2.0
2.4
2.8
E_{cm} (eV)
$Ne^+ + O_2 \rightarrow O^+(^4S^o, ^2D^o) + O(^3P) + Ne$

significantly higher than that observed for the $O^+(^4S°) + N_2$ reaction,[18] indicating that O^- prepared under the conditions of this experiment consists of a good fraction of $O^+(^2D°)$. The observation that the N_2^- cross section increases only slightly from V_{eff} = 1.53 to 0.25 V supports the conclusions that Channel I′ is minor compared to Channel II′ and that $O^-(^4S°)$ ions formed by reaction (2) are not trapped effectively in this V_{eff} range.

Without detailed information about the reaction mechanisim for O^+ formation, we assume that the reaction models for reactions (1) and (2) are similar. Namely, at E_{cm} = 0.73±0.06 eV, $O^-(^4S°)$ ions (mostly contributed by Channel I") are produced with a kinetic energy distribution peaked between 1.42 eV and 1.79 eV, whereas $O^-(^2D°)$ ions are formed with kinetic energies < 0.3 eV. Based on the interpretation given here for the cross section curve for O^- formation (Fig. 3), the branching ratio for $O^-(^4S) : O^-(^2D)$ is estimated to be < 1.25 : 3.00. In accordance with the analysis for releasing $O^-(^4S°)$ presented in Section IIB, we estimate that at V_{eff} = 0.25 V used in this experiment, the purity of $O^-(^2D°)$ is > 90%.

C. Preparation of $O^+(^4S°)$

The respective endothermicities for the formation of $O^-(^4S°) + O(^3P)$ (Channel I"), $O^-(^4S°) + O(^1D)$ (Channel II"), and $O^-(^2D°) + O(^3P)$ (Channel III") by the $Ar^+ + O_2$ reaction are 2.97, 4.94, and 6.29 eV (see Table I). We have shown in a previous experiment that the absolute cross sections for O^- formation are peaked at E_{cm} = 11.1 eV with values of ≈ 2-3 Å^2.[28] Furthermore, O^- ions are shown to be produced predominantly in the $O^-(^4S°)$ ground state by comparing their reactivity with that of $O^-(^4S°)$ prepared by dissociative photoionization of O_2.

In order to eliminate the possibility for the formation of $O^-(^2D°)$ and $O^-(^2P°)$, we have prepared O^- by reaction (3) at E_{cm} = 4.4 eV. Since the cross section for NO^- is structured and is significantly greater than that for N_2^- formed in the $O^-(^4S°) + N_2$ reaction, reaction (9),

$$O^-(^4S°) + N_2 \rightarrow NO^- + N, \qquad (9)$$

is a good monitoring reaction for $O^+(^4S°)$ formation. Figure 4 shows the cross sections for reactions (9)[52] and (6) in the E_{cm} = 0.07-13.2 eV for $O^-(^4S°)$ prepared by reaction (3). These cross sections are

Figure 4 Absolute total cross sections for NO^+ (●) and N_2^+ (○) formed by the reaction of $O^+(^4S^o) + N_2$ in the E_{lab} range of 0.15-30 eV. The thermochemical threshold of 1.96 eV for reaction (6) is marked in the figure. Here, $O^+(^4S^o)$ reactant ions are prepared by reaction (3) at E_{cm} = 0.44 eV. The cross sections in the E_{cm} range of ≈2-20 eV are measured using an $O^+(^4S^o)$ ion beam with a kinetic energy spread (FWHM) of ± 1.5 eV and the cross sections at E_{cm} < 2 eV are measured by applying the differential retarding potential method (Ref. 52) with an ion beam kinetic energy spread of ± 0.3 eV.

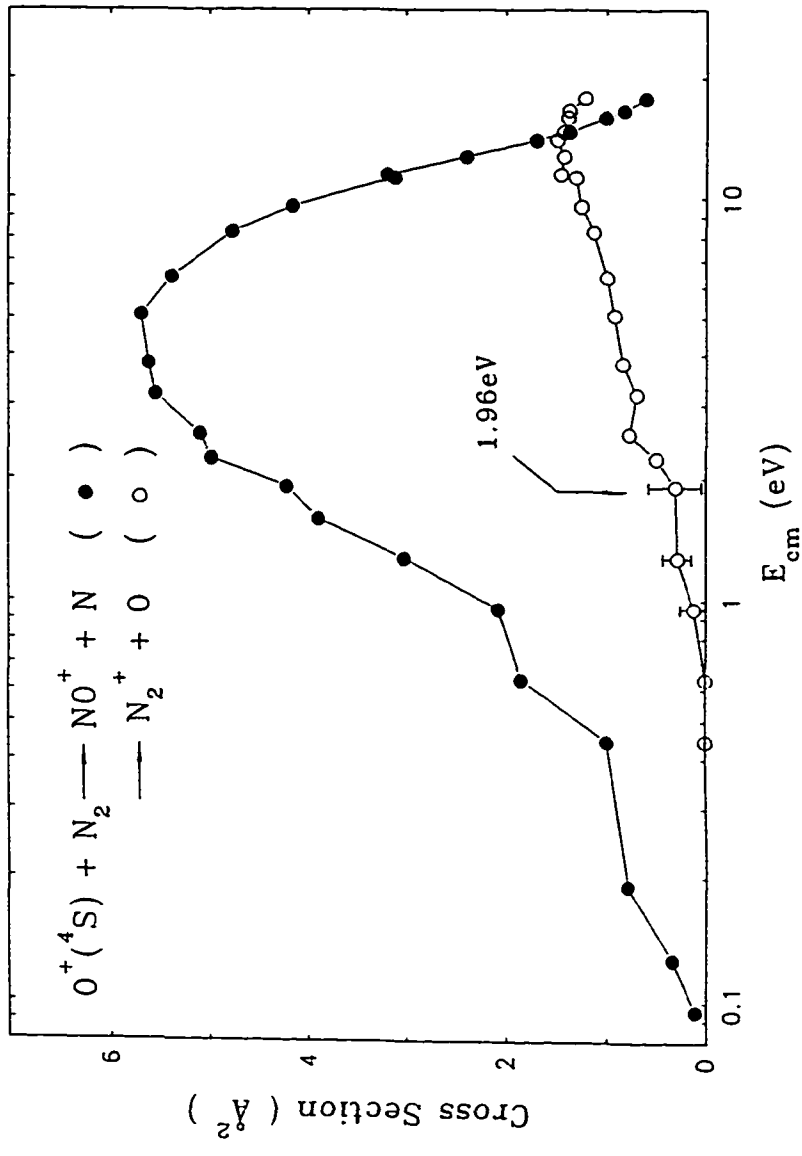
Cross Section (Å²)
0
2
4
6
0.1
1
10
E_cm (eV)
1.96eV
O⁺(⁴S) + N₂ — NO⁺ + N (●)
— N₂⁺ + O (o)

in agreement with that obtained previously using $O^-(^4S°)$ reactant ions formed by dissociative photoionization of O_2,[18] confirming that O^- ions formed by reaction (3) at E_{cm} = 4.4. eV are in the $O^-(^4S°)$ ground state. In this experiment, the RF voltage applied to the lower RF octopole ion guide is raised to a high level optimized for yielding the maximum O^+ intensity.

D. Further characterization of $O^+(^4S°, ^2D°, ^2P°)$

In summary, we have shown above that state-selected $O^-(^2P°)$ and $O^-(^2D°)$ can be prepared by reactions (1) and (2) at E_{cm} = 1.7±0.8 and 0.73±0.06 eV, respectively, using a V_{eff} of ≈0.25 V applied to an RF octopole ion guide, while state-selected $O^-(^4S°)$ can be formed by reaction (3) at E_{cm} = 4.4 eV.

According to the analyses presented in sections IIA and IIB, we conclude that the cross sections for reactions (7) and (8) at E_{cm} = 15.9 eV are 31±5 and 44±3 Å^2, respectively. We find that the cross sections for reaction (7) and (8) are nearly independent of collision energy in the E_{cm} range of 2-20 eV. This finding that the cross section is greater for reaction (8) than for reaction (7) is contrary to the results of the previous PEPICO study.[49] In order to resolve this disagreement, we have performed further characterization of $O^-(^2D°)$ and $O^-(^2P°)$ prepared using reactions (1) and (2) under the conditions described above.

In a recent study of the ion-molecule reaction of $O^-(^4S°) + CO_2$, we find that the experimental onset for the reaction,

$$O^-(^4S°) + CO_2 \rightarrow CO^- + O + O, \qquad (10)$$

is in accord with its thermochemical threshold of 5.93 eV.[55] For reactions (11) and (12) involving $O^-(^2D°)$ and $O^-(^2P°)$, the experimental onsets should shift lower to corresponding thresholds of 2.63 and 0.91 eV.

$$O^-(^2D°) + CO_2 \rightarrow CO^- + O + O \qquad (11)$$

$$O^-(^2P°) + CO_2 \rightarrow CO^- + O + O \qquad (12)$$

The absolute cross sections for reactions (10), (11), and (12) in the E_{cm} range of 1-30 eV characteristic of $O^-(^4S°)$, $O^-(^2D°)$, and $O^-(^2P°)$ formed by reactions (1), (2), and (3) are depicted in Fig.

Figure 5 Absolute total cross sections for reactions (10)-(12) in the E_{cm} range of ≈1-30 eV characteristics of $O'(^4S^o)$ (●), $O'(^2D^o)$ (○), and $O'(^2P^o)$ (▽) prepared by reactions (1)-(3) in this experiment.

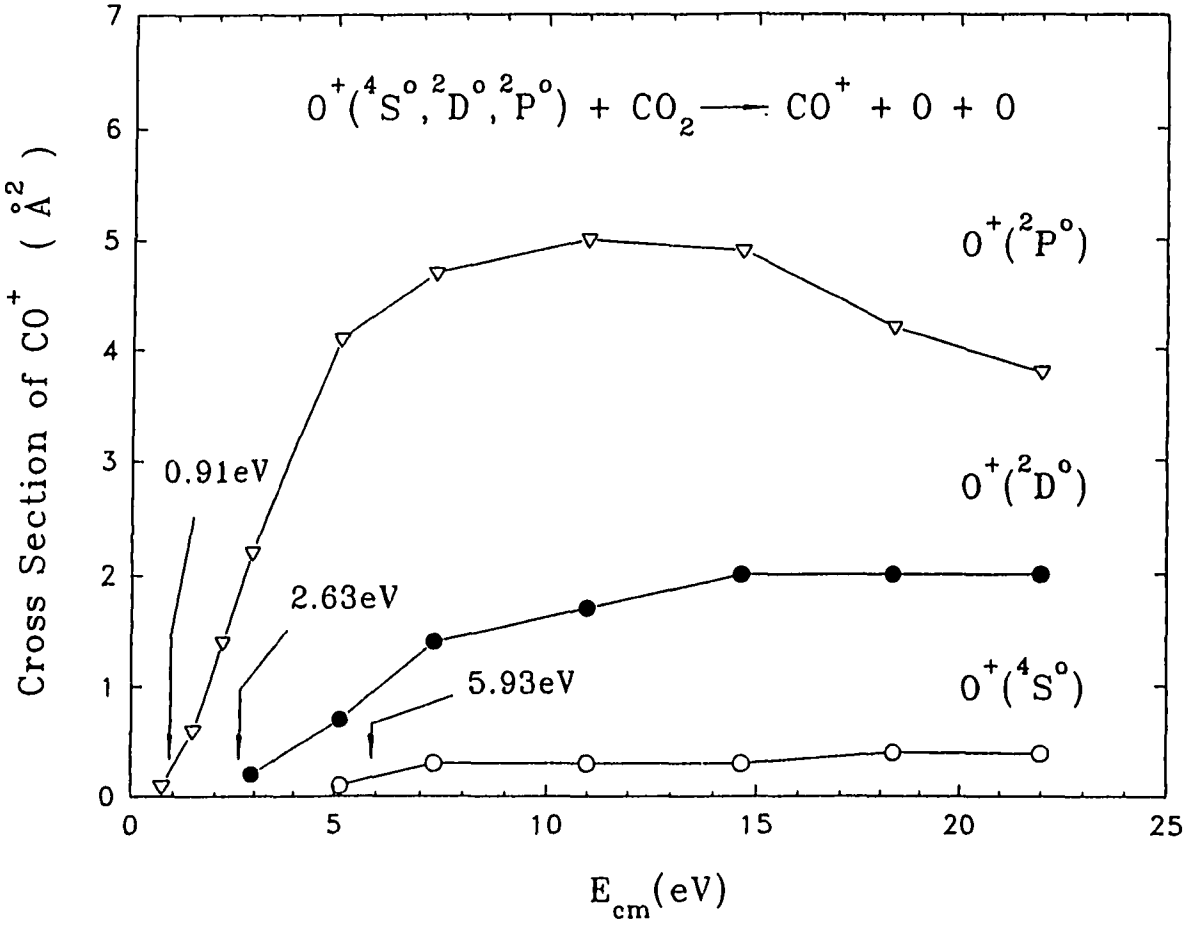
$O^+(^4S^o, ^2D^o, ^2P^o) + CO_2 \longrightarrow CO^+ + O + O$
$O^+(^2P^o)$
$O^+(^2D^o)$
$O^+(^4S^o)$
0.91eV
2.63eV
5.93eV
Cross Section of CO^+ ($Å^2$)
E_{cm}(eV)
0
1
2
3
4
5
6
7
0
5
10
15
20
25

5. These cross sections rise from their onsets and reach a constant value of 0.4 $Å^2$ for $O^+(^4S°)$, 2 $Å^2$ for $O^+(^2D°)$, and 4.7 $Å^2$ for $O^+(^2P°)$. As expected, the experimental onsets for reactions (11) and (12) are found to be in good agreement with the respective thermochemical thresholds, assuring that the O^+ ion beams prepared in these experiments using reactions (1) and (2) consist of predominantly $O^+(^2P°)$ and $O^+(^2D°)$, respectively.

For $O^+(^4S°)$ prepared by reaction (3) at E_{cm} = 4.4 eV, the formation of excited $O^+(^2D°,^2P°)$ states are not allowed energetically. The CO^+ absolute cross sections observed for $O^+(^4S°)$ of Fig. 5 agree with those obtained using $O^+(^4S°)$ reactant ions formed by dissociative photoionization of O_2.[55] On energetic ground, no O^+ ions can be formed by reaction (2) at E_{cm} = 0.73±0.06 eV. However, the CO^+ absolute cross sections observed for $O^+(^2D°)$ cannot be used to rule out the existence of finite $O^+(^4S°)$ ions. Similarly, based on the CO^+ absolute cross sections for $O^+(^2P°)$ shown in Fig. 5, we cannot exclude the existence of finite $O^+(^2S°,^2D°)$ ions.

III. Conclusions

We have shown that using the dissociative charge transfer reactions (1), (2), and (3) at specific collision energies, and using appropriate RF octopole ion guide trapping potentials, ion beams in nearly pure $O^+(^4S°)$, $O^+(^2P°)$, and $O^+(^2D°)$ states can be obtained with usable intensities for scattering experiments. Using the experimental conditions given above, we estimate that the fraction of $O^+(^2P°)$ is enriched to ≈ 90% from ≈52% for $O^+(^2P°)$ originally produced by reaction (1) at E_{cm} = 1.69±0.8 eV. A higher fraction of $O^+(^2P°)$ can be realized if a lower E_{cm} for reaction (1) is used.

The experimental method described here can be viewed as an enrichment scheme which can be used to increase the concentration of an excited ionic species produced in an ion-molecule reaction with a lower kinetic energy distribution compared to those for ionic species in other states. With careful selection of dissociative charge transfer or dissociative photoionization processes, this method should be applicable for the preparation of other state-selected excited atomic ions.

Acknowledgement:

This work is supported by the National Science Foundation grant ATM 9200785.

References:

1. C. Y. Ng and M. Baer, eds., *"State-Selected and State-to-State Ion-Molecule Reaction Dynamics I: Experiment"* (Wiley, New York, 1992), *Adv. Chem. Phys.* Vol. 82
2. M. Baer and C. Y. Ng, eds., *"State-Selected and State-to-State Ion-Molecule Reaction Dynamics II: Theory"* (Wiley, New York, 1992), *Adv. Chem. Phys.* Vol. 82.
3. C. Y. Ng, T. Baer, and I. Powis, eds., *"Unimolecular and Bimolecular Ion-Molecule Reaction Dynamics"*, *Wiley Series in Ion Chem. & Phys.* (Wiley, Chichester, 1994)
4. P. B. Armentrout, in *"Gas Phase Inorganic Chemistry"*, D. H. Russell, ed. (Plenum, New York, 1989), p. 1.
5. M. A. Smith, in *"Unimolecular and Bimolecular Ion-Molecular Reaction Dynamics"*, C. Y. Ng, T. Baer, and I. Powis, eds. , *Wiley Series in Ion Chem. & Phys.* (Wiley, Chichester, 1994), p. 87.
6. C. Y. Ng, in *"State-Selected and State-to-State Ion-Molecule Reaction Dynamics: I. Experiment"*, C. Y. Ng and M. Baer, eds. (Wiley, New York, 1992), *Adv. Chem. Phys.* Vol. **82**, p. 401.
7. C. Y. Ng, in *"Techniques for the Study of Gas-Phase Ion-Molecule Reactions"*, J. M. Farrar and W. H. Saunder, Jr., Eds.; (Wiley: New York, 1988), p. 417.
8. P. M. Banks and G. Kockarts, *"Aeronomy"*, Part A (Academic, New York, 1973), p. 14. 257.
9. M. R. Torr and D. G. Torr, *Rev. Geophys. Space Phys.* **20**, 91 (1982).
10. A. Dalgarno and M. B. McElroy, *Planet. Space Sci.* **13**, 947 (1965).
11. R. J. Henry, *Astrophys. J.* **161**, 1153 (1970).
12. J. L. Kohl, G. P. Lafyatis, H. P. Palenius, and W. H. Parkinson, *Phys. Rev.* A **18**, 571 (1978).
13. D. G. Torr and N. Orsini, *Planet. Space Sci.* **25**, 1171 (1977).
14. D. G. Torr and N. Orsini, *Geophys. Res. Lett.* **5**, 657 (1980).
15. M. R. Torr and D. G. Torr, *Geophys. Res. Lett.* **7**, 103 (1980).
16. E. E. Ferguson, F. C. Fehsenfeld, and D. L. Albritton, in *"Gas Phase Ion Chemistry"*, M. T. Bowers, ed., (Academic, New York, 1979), Vol. 1, p. 45.
17. A. Dalgarno and J. L. Fox, in *"Unimolecular and Bimolecular Ion-Molecule Reaction Dynamics"*,

C. Y. Ng, T. Baer, and I. Powis, eds., *Wiley Series in Ion Chem. & Phys.* (Wiley, Chichester, 1994) p. 1.

18. G. D. Flesch and C. Y. Ng, *J. Chem. Phys.* **92**, 3235 (1990) and **94**, 2372 (1991), and references therein.
19. H. M. Rosenstock, K. Draxl, B. W. Steiner, and J. T. Herron, "Energetics of Gaseous Ions", *J. Phys. and Chem. Ref. Data*, **6**, Suppl. 1 (1977).
20. I. Koyano and K. Tanaka, in *"State-Selected and State-to-State Ion-Molecule Reaction Dynamics: I. Experiment"*, C. Y. Ng and M. Baer, eds. (Wiley, New York, 1992), *Adv. Chem. Phys.* Vol. **82**, p. 263.
21. J. C. Weisshaar, in *"State-Selected and State-to-State Ion-Molecule Reaction Dynamics: I. Experiment"*, C. Y. Ng and M. Baer, eds. (Wiley, New York, 1992), *Adv. Chem. Phys.* Vol. **82**, p. 213.
22. S. L. Anderson, in *"State-Selected and State-to-State Ion-Molecule Reaction Dynamics: I. Experiment"*, C. Y. Ng and M. Baer, eds. (Wiley, New York, 1992), *Adv. Chem. Phys.* Vol. **82**, p. 177.
23. In an effort to examine the ion chemistry for state-selected $O^+(^4S°,^2D°,^2P°)$, we attempted the preparation of state-selected $O^+(^2D°)$ and $O^+(^2P°)$ in a VUV photoionization experiment with O atoms using a PEPICO scheme (see Fig. 41 of Ref. 6). We found that the sensitivity is too low for performing a scattering experiment.
24. G. Bischof and F. Linder, *Z. Phys.* **D1**, 303 (1986).
25. M. Scherbarth, Diplom Thesis, University of Freiburg (1988).
26. D. Gerlich, in *"State-Selected and State-to-State Ion-Molecule Reaction Dynamics: I. Experiment"*, C. Y. Ng and M. Baer, eds. (Wiley, New York, 1992), *Adv. Chem. Phys.* Vol. **82**, p. 1.
27. G. D. Flesch and C. Y. Ng, *J. Geophys. Res.* **96**, 21407 (1991).
28. G. D. Flesch, S. Nourbakhsh, and C. Y. Ng, *J. Chem. Phys.* **92**, 3590 (1990).
29. C.-L. Liao, J.-D. Shao, R. Xu, G. D. Flesch, Y.-G. Li, and C. Y. Ng, *J. Chem. Phys.* **85**, 3874

(1986).

30. J.-D. Shao, Y.-G. Li, G. D. Flesch, and C. Y. Ng, *Chem. Phys. Lett.* **132**, 58 (1986).

31. J.-D. Shao, Y.-G. Li, G. D. Flesch, and C. Y. Ng, *J. Chem. Phys.* **86**, 170 (1987).

32. G. D. Flesch and C. Y. Ng, *J. Chem. Phys.* **89**, 3381 (1988); G. D. Flesch, S. Nourbakhsh, and C. Y. Ng, *J. Chem. Phys.* **95**, 3381 (1991).

33. G. D. Flesch and C. Y. Ng, *J. Chem. Phys.* **92**, 2876 (1990).

34. N. R. Daly, *Rev. Sci. Instrum.* **31**, 264 (1960).

35. G. O. Brink, *Rev. Sci. Instrum.* **37**, 857, 1626 (1966).

36. E. Teloy and D. Gerlich, *Chem. Phys.* **4**, 417 (1974).

37. The expression for the effective trapping potential V_{eff} given in Eq. (5) is valid for an ion formed near the axis of the octopole ion guide resulting in a negligibly small orbital angular momentum. See Ref. 26.

38. We note that O^+ formed by reaction (1) is not isotropic. The experimental results of Ref. 23 indicate that the angular distribution of O^+ formed by reaction (1) is peaked near the center-of-mass scattering angles of O° and 180°, i.e. in the directions along the octopole axis.

39. This fraction includes the forward and backward scattered $O^+(^4S°)$ or $O^+(^2D°)$ ions along the octopole axis.

40. W. R. Gentry, in "*Gas Phase Ion Chemistry*", M. T. Bowers, Ed. (Academic, New York, 1979), Vol. 2, p. 221.

41. C. E. Moore, "*Atomic Energy Levels*", Natl. Bur. Stand. (U.S.) Cir. No. 467 (U. S. GPO, Washington, D. C., 1949), Vol. I.

42. P. H. Krupenie, *J. Phys. Chem. Ref. Data*, **1**, 423 (1972).

43. K. Codling and R. P. Madden, *J. Chem. Phys.* **42**, 3935 (1965).

44. K. Tanaka and M. Yoshimine, J. Chem. Phys. **70**, 1626 (1979).

45. P. M. Guyon, T. Baer, L. F. A. Ferreira, I. Nenner, A. Tabché-Fouhailé, R. Botter, and T. R. Govers, *J. Phys.* **B11**, L141 (1978).

46. M. Richard-Viard, O. Dutuit, M. Lavollée, T. R. Govers, P. M. Guyon, and J. Durup, *J. Chem. Phys.* **82**, 4054 (1985).

47. I. Nenner, P. M. Guyon, T. Baer, and T. R. Govers, *J. Chem. Phys.* **72**, 6587 (1980).

48. N. H. Beebe, E. W. Thulstrup, and A. Anderson, *J. Chem. Phys.* **64**, 2080 (1976).

49. M. Lavollée and G. Henri, *J. Phys. B* **22**, 2019 (1989).

50. G. D. Flesch and C. Y. Ng, *J. Chem. Phys.*, **97**, 162 (1992).

51. By examining the reactivity of O^+ formed as a function of collision energy, we conclude that Channel V′ is also produced at E_{cm} above its thermochemical threshold. However, the reactivity measurement does not support the formation of Channel IV′.

52. X. Li, Y.-L. Huang, G. D. Flesch, and C. Y. Ng, *Rev. Sci. Instrum.*, accepted.

53. These cross sections are obtained using the differential retarding potential method (see Ref. 52) with a center-of-mass kinetic energy spread of ±0.25 eV (FWHM) at E_{cm} = 0.43 eV. The uncertainty due to the calibration of the ion beam energy is estimated to be ±0.06 eV.

54. The ΔE value of 0.43 eV is the average values of 0.38 and 0.48 eV for reaction (2) associated with the $Ne^+(^2P_{1/2})$ and $Ne^+(^2P_{3/2})$ spin-orbit states, respectively.

55. G. D. Flesch and C. Y. Ng, *J. Geophys. Res.* **96**, 21403 (1991).

CHAPTER II

A DIFFERENTIAL RETARDING POTENTIAL METHOD FOR IMPROVING ION BEAM KINETIC ENERGY RESOLUTION

A paper submitted to Review Scientific Instrument

X. Li, Y.-L. Huang, G. D. Flesch and C. Y. Ng

Abstract:

We present a differential retarding potential (DRP) method for improving the kinetic energy resolution of a reactant ion beam for scattering experiments. This method allows ion-molecule reaction absolute total cross section measurements to be performed down to thermal energies using the simple electrostatic aperture ion lenses of a tandem quadrupole mass spectrometric ion-molecule reaction apparatus, even though the reactant ions are formed originally with a broad kinetic energy distribution. To illustrate the principle of the DRP method, examples are given for its application to reactant ion beams prepared in an electron impact ion source and in an ion-molecule reaction ion source.

I. Introduction

Low energy ion-molecule reaction cross section or rate measurements have made important contributions to understanding the fundamental chemistry in plasma environments, such as in planetary atmospheres.[1-3] Because the cross sections or rates for exothermic ion-

molecule processes are usually very high at low collision energies, they play an important role in modeling reactive systems containing atomic and molecular ions. The appearance energies (AE) for endothermic ion-molecule reactions have been widely used to derive bond energies or heats of formation for ionic and neutral species.[4] The accuracy of experimental low energy cross sections and AEs depends on the kinetic energy resolution, which is in part determined by the kinetic energy spread of the reactant ion beam used in a scattering experiment.

The preparation of a reactant ion beam with a low kinetic energy spread may be achieved using an energy analyzer. However, disregarding the increased complexity of the experiment, the ion transmission for an energy analyzer is usually very poor at low kinetic energies, making its application impractical, especially when the original reactant ion beam intensity is low. This is the case where reactant ions are prepared by ion-molecule collisions or by photoionization.[5,6]

We have been undertaking ion-molecule reaction studies using a triple-quadrupole double-octopole (TQDO) apparatus.[5,6] Figure 1 depicts the schematic diagram for the TQDO ion-molecule reaction apparatus without the differential pumping vacuum chambers. The TQDO apparatus essentially consists in sequential order, a photoionization ion source or an electron impact ion source (1), a reactant quadrupole mass spectrometer (QMS) (3), a lower radio frequency (RF) octopole ion guide reaction gas cell (RFOIGGC) [(4) + (5)], a middle QMS (6), an upper RFOIGGC [(7) + (8)], a product QMS (9), and a Daly-type scintillation ion detector [(10) + (11) + (12)]. Using the QMS-RFOIGGC-QMS-RFOIGGC-QMS configuration, we have measured the internal energy distributions of product ions, formed by many simple ion-molecule reactions in the lower RFOIGGC, by examining their reactivities with an appropriate set of neutral reactants in the upper RFOIGGC. For absolute total cross section measurements, the TQDO apparatus is used as a tandem quadrupole mass spectrometer

together with the upper RFOIGGC. The QMS-RFOIGGC-QMS combination has become a standard arrangement for absolute total cross section measurements of ion-molecule processes.[6,7] In addition to the ability of forming reactant ions by the vacuum ultraviolet (VUV) photoionization and electron impact ionization methods, the TQDO apparatus also allows the preparation of reactant ions by an ion-molecule reaction in the lower RFOIGGC. In such cases, absolute total cross section measurements for ion-molecule reactions involving the reactant ions are measured using the upper RFOIGGC, i.e., an overall QMS-RFOIGGC-QMS-RFOIGGC-QMS configuration is used.

Assuming that photoionization or electron ionization takes place between two parallel repeller plates with a separation of ℓ (cm) and that a constant electrostatic field E (V/cm) is maintained at the ionization region by applying a potential difference ΔV (= E x ℓ) between the repeller plates, the reactant ion laboratory kinetic energy spread (ΔE_{lab}) is expected to be E x h eV. Here, h is the height of the photon or electron beam measured in the direction perpendicular to the repeller plates. Practically, a finite E is required for efficient extraction of the reactant ions, and lowering h can severely reduce the ionization VUV photon intensity. These conditions have limited the attainable kinetic energy resolution for a reactant ion beam formed by the VUV photoionization method. In order to achieve sufficiently low ΔE_{lab} for kinetic energies below 1 eV, the reactant ion intensity obtainable by VUV photoionization may become too low for accurate ion-molecule reaction cross section measurements. The intensity restriction for an electron impact ion source is less severe if monochromatic electrons are not required. However, an electron impact ion source operating in a relatively high pressure may suffer from surface charging, which introduces an unpredictable effect on the ion beam energy and its energy spread.

In the case of preparing reactant ions by an ion-molecule reaction, reactant ions may

be formed over the region defined by the repeller field. In addition to the restrictions in achievable kinetic energy spread stated above, the ΔE_{lab} value of the reactant ions thus formed is also governed by the nature, such as the exothermicity, of the ion-molecule process. Using the TQDO apparatus, the ΔE_{lab} value of the reactant ions prepared in the lower RFOIGGC is determined mainly by the exothermicity of the ion-molecule process involved.

In addition to these intrinsic limitations to the attainable kinetic energy resolution of a reactant ion beam, the kinetic energy distribution of an ion beam can be affected by passing through an RF device such as a QMS.[7] It is well known that in passing through a QMS, the radial kinetic energies of reactant ions may be altered, resulting in a broader ion kinetic energy distribution. This effect may be minimized by using small apertures for the ion entrance and exit of the QMS. Since the intensity for reactant ions prepared by VUV photoionization is low, it is necessary to use relatively large entrance and exit apertures for the QMS in order to maximize the ion transmission. We have found that the ΔE_{lab} increases after passing through the QMS and that the increase is proportional to the RF amplitude supplied to the QMS.

We present here a simple differential retarding potential (DRP) method which can be used to improve the kinetic energy resolution of reactant ions prepared by an electron impact or ion-molecule reaction ion source. In effect, this method allows the preparation of a reactant ion beam at laboratory kinetic energies (E_{lab}) well below 1 eV with good resolution even though the original ion kinetic energy spread is broad. The principle of this method is similar to the retarding potential difference method introduced previously by Fox et al.[8,9] to obtain a higher electron energy resolution of an electron beam for electron impact ionization studies. In essence, the RDP method achieves a narrower kinetic energy distribution by taking the difference between a non-retarded and a retarded kinetic energy distribution of the reactant

ions. To implement the DRP method in the application of the TQDO apparatus, we select two of the intermediate electrostatic lenses, lenses *a* and *b*, situated between the middle QMS and the upper RF octopole ion guide (7), as the retarding lenses (see Fig. 1). Using the DRP method described below on a reactant ion beam produced in an electron ionization or ion-molecule reaction ion source, we have obtained reliable ion-molecule reaction cross sections at collision energies close to thermal energies. Because of the simplicity of the DRP method, it can be applied readily in a conventional ion-molecule reaction apparatus with little modification.

II. Experiments illustrating the differential retarding potential method

The application of the TQDO apparatus (Fig. 1) for absolute total cross section measurements has been described in detail previously.[5,6] Although the TQDO apparatus is used here to illustrate the DRP method, we emphasize that the principle for the application of the DRP method does not depend on the detailed design of the TQDO apparatus.

A. Reactant ions prepared by an electron impact ionization source

Here, we use a Ne^+ ion beam formed in an electron impact ionization ion source and the cross section measurement for the reactions,

$$Ne^+ + O_2 \rightarrow O^+(^4S,^2D) + O(^3P) + Ne, \qquad (1)$$

as an example to illustrate the principle of the DRP method. The formation of $O^+(^4S)$ by reaction (1) is exothermic by 2.9 eV, while the channel for $O^+(^2D)$ formation is endothermic by 0.44 eV.[10,11] At center-of-mass kinetic energies (E_{cm}) below 2.1 eV ($E_{lab} < 2.8$ eV) , the formation of metastable O+(2P) ions is not allowed energetically.11

Figure 1 Schematic of the tandem mass spectrometer arrangement for absolute total cross section measurements. (1) electron impact ionization ion source, (2) nozzle, (3) reactant QMS, (4) lower RF octopole ion guide, (5) lower RFOIGGC, (6) middle QMS, (7) upper RF octopole ion guide, (8) upper RFOIGGC, (9) product QMS, (10) scintillator, (11) photomultiplier tube, (12) aluminum ion target. Note that the Daly-type scintillation detector consists of items (10), (11), and (12). The intermediate aperture lenses *a, b, c,* and *d* have the same aperture size (0.89 cm in diameter and 0.14 cm in thickness).

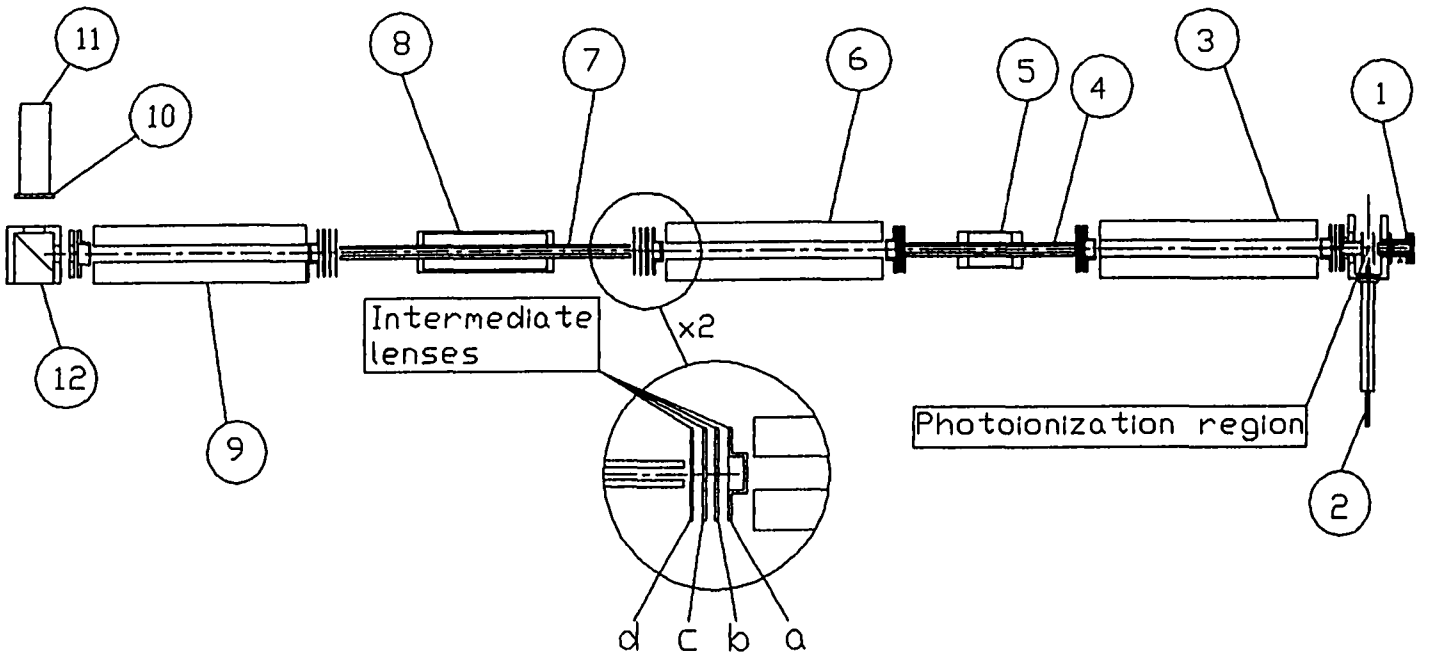
11
10
8
7
6
5
4
3
1
12
9
Intermediate lenses
x2
Photoionization region
2
d
c
b
a

Reactant Ne+ ions prepared by electron ionization of Ne in the electron impact ionization source are extracted and focused into the reactant QMS, which is tuned to the mass of Ne+ (mass to charge ratio = 20). The electron impact ionization source used here is of the Brink design12 and the ionization electron energy is ≈ 80 eV. The Ne+ ions exit the reactant QMS and traverse the lower RF octopole ion guide (4) and the middle QMS before entering the upper RFOIGGC, where they react with the neutral reactant O2. Here the middle QMS is operated in the RF only mode, functioning as an ion guide. The product ions formed in the gas cell are guided and focused into the product QMS, where they are mass analyzed before their detection by a Daly-type scintillating ion detector.13.

The nominal kinetic energy of the reactant Ne^+ ions is determined by the potential difference between the upper RFOIGGC and the grid of the Brink ionizer, where the Ne^+ ions are formed. However, due to surface charging and field penetration effects etc., the actual E_{lab} value is usually different from the nominal kinetic energy. A convenient method for measuring the actual E_{lab} of the Ne^+ ion beam is to perform a retarding potential analysis using the upper RF octopole ion guide as the retarding lens. This is done by raising the dc potential applied to the upper octopole ion guide until no ions are detected by the ion detector, indicating that no ions are transmitted. Curve A of Fig. 2 is a typical retarding potential curve for Ne^+ using the upper octopole ion guide as the retarding element. In this example, the Ne^+ intensity is nearly constant for retarding potentials of the octopole ion guide < 5.0 V, and decreases to half its highest intensity at 6.8 V. The intensity for Ne^+ remains finite for retarding potentials > 10 V. If the dc potential of the octopole ion guide is at ground potential (zero volt), E_{lab} for the Ne^+ ion beam is 6.8 ± 2.0 eV. The differential of Curve A (Curve A′, also shown in Fig. 2) is a measure of the E_{lab} distribution for Ne^+. Curve A′ indicates that the E_{lab} distribution for Ne^+ peaks at ≈ 5.9 eV and tails more gradually toward

higher E_{lab} with a full-width-at-half-maximum (FWHM) of ≈ 2 eV.

The four simple intermediate ion lenses (labelled as *a*, *b*, *c*, and *d*) normally used to refocus the reactant ion beam into the upper RF octopole (7) are shown in a magnified view in Fig. 2. As indicated above, we have selected lenses *a* and *b* as the retarding lenses for the reactant ions in the applicationof the DRP method.

Curve C is the retarding potential curve obtained when the dc potential applied to the intermediate lenses *a* and *b* (the same potential is applied to lenses *a* and *b*) is raised empirically above that used for obtaining Curve A. Note that the intensity for Ne^+ in the plateau region of Curve C decreases by nearly 40% compared to Curve A, indicating that ≈ 40% of the original Ne^+ ions at lower E_{lab}'s are blocked from entering the octopole ion guide by the higher potential applied to the retarding lenses *a* and *b*. However, Curves A and C are essentially identical at retarding potentials of the octopole ion guide > 6.6 V. The differential of Curve C (Curve C′ of Fig. 2) shows the E_{lab} distribution of the Ne^+ ion beam characterized by Curve C. By taking the difference between Curves A′ and C′ (Curve A′-C′), we obtain the E_{lab} distribution of the Ne^+ ions that have been blocked due to the dc potential increase of the intermediate lenses *a* and *b*. This distribution (Curve A′-C′), shown in the inset at the upper right-hand corner of Fig. 2, is truncated at 6.8 eV and has a FWHM = ΔE_{lab} of about 1.0 eV, a value more than a factor of two less than the FWHM for the E_{lab} distribution of the original Ne^+ ion beam characterized by Curve A′.

The retarding potential Curve B is observed using a potential applied to the intermediate lenses *a* and *b* that is between those used for Curves A and C. The intensity for Ne^+ in the plateau region of Curve B is about 20% lower than that of Curve A. Curve B is found to be identical to Curve A at retarding potentials of the octopole ion guide > 6.2 V. The differential of Curve B (Curve B′) lies in between Curves A′ and C′ in the retarding

Figure 2 Retarding potential energy curves for the Ne^+ reactant ion beam formed in a Brink-type electron ionization ion source. Curves A, B, and C are measured using dc potentials of 7.5, 8.0, and 8.5 V, respectively, applied to the intermediate lenses *a* and *b*. A′, B′, and C′ (the respective differentials of Curves A, B, and C) show the kinetic energy distributions of ion beams associated with A, B, and C. The kinetic energy distributions for the DRP Ne^+ reactant ions A-C and A-B are A′-C′ and A′-B′, respectively, and are compared in the inset of the upper right hand corner. See the text.

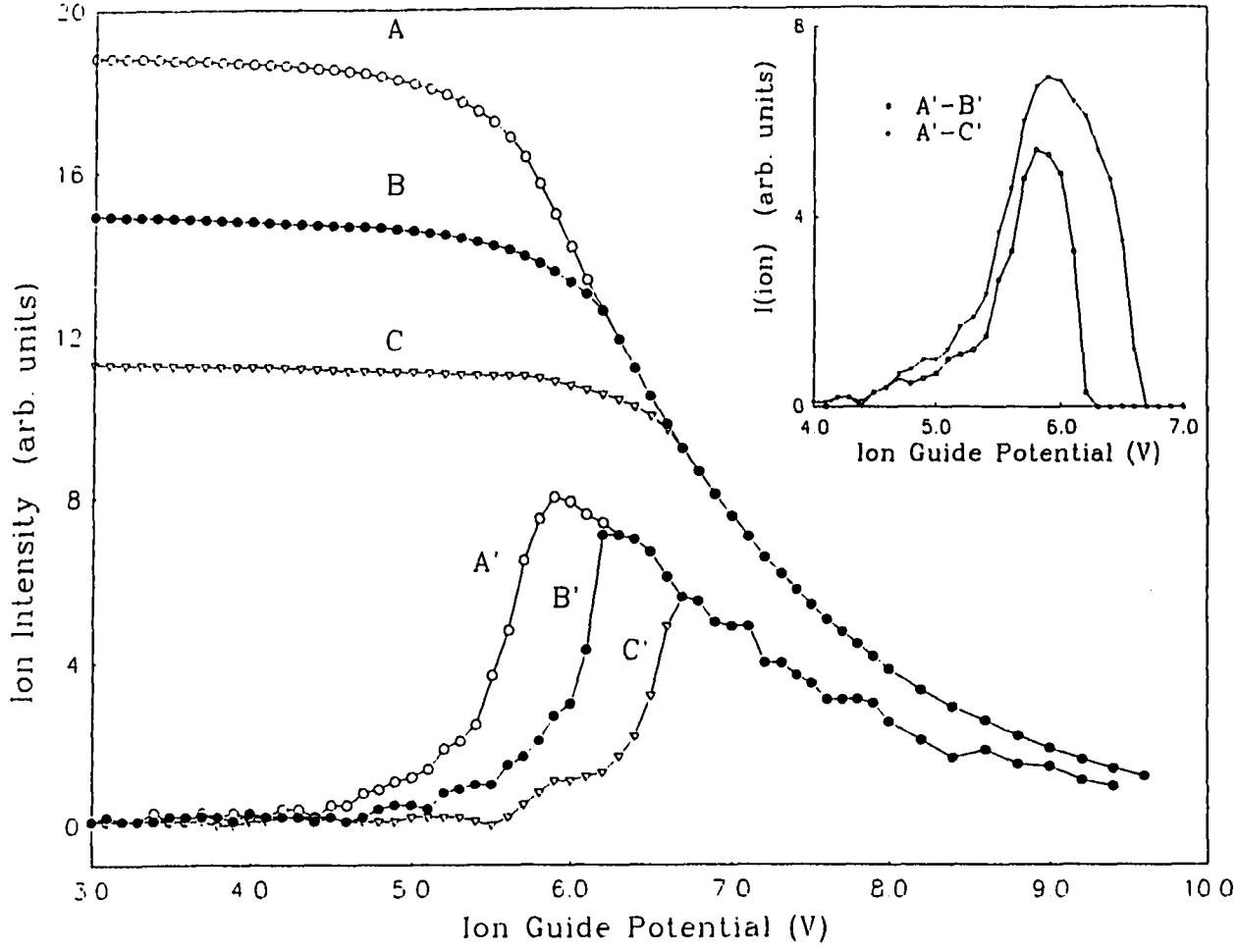
A
B
C
A'
B'
C'
Ion Intensity (arb. units)
Ion Guide Potential (V)
I(ion) (arb. units)
A'-B'
A'-C'
Ion Guide Potential (V)

potential range < 6.6 V applied to the octopole ion guide. We compare the E_{lab} distributions, Curve A′-B′ and Curve A′-C′, in the inset at the upper right-hand corner of Fig. 2. As expected, the FWHM (= ΔE_{lab}) for Curve A′-B′ is ≈ 0.5 V, a factor of two narrower than that for Curve A′-C′.

The actual potentials applied to the intermediate lenses *a* and *b* are 7.5, 8.0, and 8.5 V for obtaining the retarding potential Curves A, B, and C, respectively. Note that these lens potentials are greater than the average Ne^+ beam energy of 6.8 V. However, since the apertures for the intermediate lenses are relatively large, a portion of the Ne^+ ions at energies lower than the intermediate lens potential can still pass through these lenses because of field penetration from the entrance lens (intermediate lenses *c* and *d*) of the octopole ion guide. That is, the effective potentials seen by the Ne^+ ions are less than the actual potentials applied to the intermediate lenses *a* and *b*. The essential point is that care is needed to establish retarding potential energy curves (such as Curves A, B, and C) whose high energy tails are nearly identical. In such cases, the transmission of the higher energy Ne^+ ions is unaffected by slight changes in focusing conditions.

We have shown above that the differences Curve A - Curve B and Curve A - Curve C correspond to Ne^+ ion beams with kinetic energies of 5.8 ± 0.5 and 6.0 ± 1.0 eV, respectively. The E_{lab} of the Ne^+ reactant ion beam can be varied by varying the dc potential of the octopole ion guide. For example, when the octopole ion guide dc potential is set at 4.0 V, the E_{lab} for the Ne^+ ion beam of Curve A - Curve B becomes 1.8 ± 0.5 eV. We note that the kinetic energy distribution of Curve A′-B′ has a low energy tail extending down to 4.4 eV. As the dc potential applied to the octopole ion guide increases above 4.4 V, the tail part of the Ne^+ ions with E_{lab} lower than the dc octopole potential is expected to be stopped by the octopole ion guide and thus to be unable to enter the reaction gas cell.

Figure 3 shows the absolute total cross sections (solid circles) of reaction (1) in E_{cm} range of 0.06-2.35 eV obtained using a DRP Ne^+ ion beam with $\Delta E_{lab} = \pm 0.2$ eV. The uncertainties of the absolute total cross sections presented here are estimated to be $\pm$ 20%. However, the relative uncertainties are less than 5%.

Here, the center-of-mass kinetic energy is $E_{cm} = E_{lab}x[M/(M + m)]$, where M and m are the masses for O_2 and Ne, respectively. Thus, a ΔE_{lab} of $\pm$ 0.2 eV corresponds to $\Delta E_{cm} = \pm 0.12$ eV. The uncertainty contributed by the random thermal motion[14] of O_2 in the gas cell is predicted to be $\Delta E_{th} = (11.1\gamma kTE_{cm})^{1/2}$, where k is the Boltzmann constant, T is the temperature of the gas cell, and $\gamma = m/(M + m)$. Since a finite fraction of the RF power is dissipated in the octopole ion guide, we estimate that T is approximately 300 K. At $E_{cm} =$ 0.44 eV, we calculate a value of 0.22 eV for ΔE_{th}. That is, the actual experimental kinetic energy spread at $E_{cm} = 0.44$ eV is $\Delta E_{1/2} = [(\Delta E_{th})^2 + (\Delta E_{cm})^2]^{1/2} = \pm 0.25$ eV. Furthermore, we estimate that the E_{lab} scale of the DRP Ne^+ ion beam is uncertain by $\pm$ 0.1 eV, translating into possible shifts of $\pm$ 0.06 eV for the E_{cm} scale. As shown in Fig. 3, the cross section curve for O^+ measured using the DRP Ne^+ (solid dots) increases from a cross section of 1.25 $Å^2$ at $E_{cm} = 0.06$ eV to 4.25 $Å^2$ at $E_{cm} = 0.4$ eV. Taking into account the $\Delta E_{1/2}$ value and the possible shift in the E_{cm} scale, we interpret that this increase in cross section corresponds to the onset for the formation of $O^+(^2D)$, which is endothermic by 0.44 eV.

The cross sections for reaction (1) (open circles) measured using the original Ne^+ beam, which has a E_{lab} distribution characterized by Curve A', are also included in Fig. 3. A possible shift in the E_{cm} scale for these cross section is estimated to be $\pm$ 0.4 eV. The cross sections for O^+ measured at $E_{cm} > 1.6$ eV using the original and the DRP Ne^+ ion beam are in agreement. The cross section curve associated with the original Ne^+ ion beam begins to

Figure 3 Absolute total cross sections for O^+ formed by reaction (1) in the E_{cm} range from 0.06-2.6 eV. Solid dots: measured using a DRP Ne^+ reactant ion beam with $\Delta E_{lab} = \pm 0.2$ eV. Open dots: measured using the original Ne^+ reactant ion beam with $\Delta E_{lab} \approx 2$ eV.

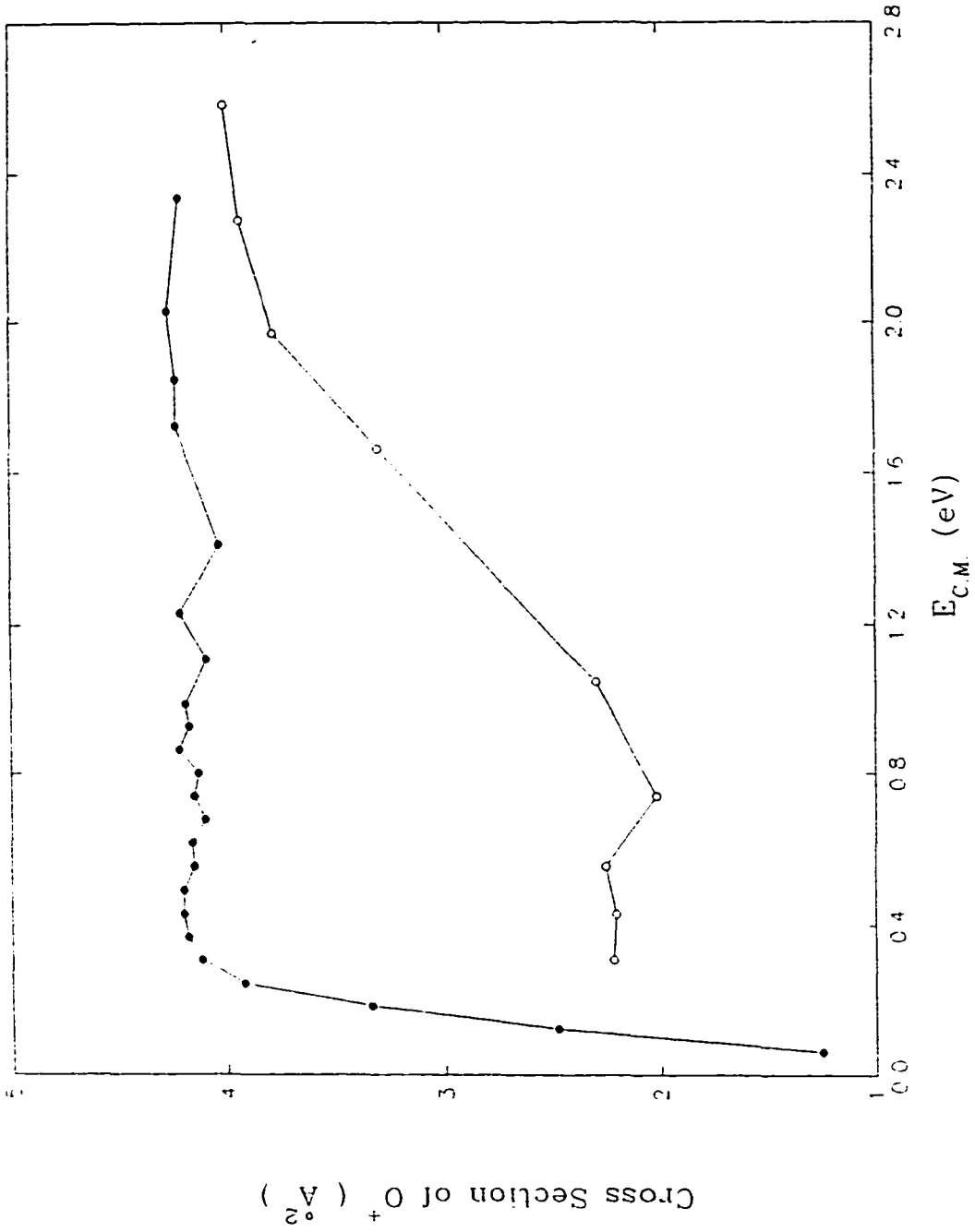
Cross Section of O^+ ($\AA^2$)
$E_{C.M.}$ (eV)
0.0
0.4
0.8
1.2
1.6
2.0
2.4
2.8
1
2
3
4
5

drop at E_{cm} = 1.6 eV and reaches a constant value of 2.25 Å^2 at E_{cm} < 0.9 eV. The difference between the two cross section curves can be attributed in most part to the different ΔE_{lab}'s of the reactant Ne^+ ion beams used in the measurements.

B. Reactant ions prepared by an ion-molecule reaction source

We have selected the ion-molecule reaction,

$$O^+(^4S) + N_2 \rightarrow NO^+ + N, \qquad (2)$$

to illustrate the case for reactant ions prepared using an ion-molecule reaction ion source. In this experiment, $O^+(^4S)$ reactant ions are formed by the endothermic ion-molecule reaction,

$$Ar^+(^2P_{3/2,1/2}) + O_2 \rightarrow O^+(^4S) + O + Ar, \qquad (3)$$

in the lower RFOIGGC. The $Ar^+(^2P_{3/2,1/2})$ ions are formed by ionization of Ar in the electron impact ion source and are selected by the reactant QMS before entering the lower RFOIGGC. The formation of O^+ by the reaction $Ar^+(^2P_{3/2}) + O_2$ is endothermic by 2.97 eV. We have shown in a previous experiment[15] that the absolute total cross sections for the O^+ formation by reaction (3) are peaked at $E_{lab} \approx 25$ eV with values of ≈ 2-3 Å^2. Furthermore, O^+ ions are shown to be produced predominantly in the ^4S ground state by comparing the reactivity of O^+ formed in reaction (3) and that of $O^+(^4S)$ prepared by photoionization of O_2.[15] The $O^+(^4S)$ reactant ions prepared by reaction (3) are mass selected by the middle QMS prior to their reactions with N_2 in the upper RFOIGGC. Using a lower RFOIGGC Ar pressure of 3×10^{-4} Torr, the $O^+(^4S)$ reactant ion intensity is observed to be ≈ 3×10^4 counts/s, which is sufficient for carrying out the cross section measurement for reaction (2). The nominal kinetic energy

for reaction (2) is thus determined by the dc potential difference between the upper and lower RFOIGGC's. Product NO^+ ions due to reaction (2) are mass selected by the product QMS before their detection by the Daly scintillating ion detector.

In order to eliminate the possibility for the formation of O^+ in the first excited $O^+(^2D)$ state, we have limited the E_{lab} for reaction (3) to less than 14 eV. The retarding potential analysis indicates that the reactant $O^+(^4S)$ ions formed by reaction (3) in the lower RFOIGGC have a ΔE_{lab} value of $\pm$ 1.5 eV. The absolute total cross sections for reaction (2) obtained using these $O^+(^4S)$ reactant ions are measured and plotted in Fig. 4 as open circles. Using the DRP method described in detail in section IIA, we have measured the absolute cross sections for the formation of NO^+ by reaction (2) using $O^+(^4S)$ at a ΔE_{lab} value of $\pm$ 0.3 eV. The cross sections thus obtained are also plotted in Fig. 4 (solid circles). The comparison shown in Fig. 4 indicates that cross sections for NO^+ at $E_{cm} < 1.3$ eV ($E_{lab} \approx 2$ eV) measured using an O^+ reactant ion beam with $\Delta E_{lab} = \pm 1.5$ eV are significantly greater than those obtained using an O^+ ion beam with $\Delta E_{lab} = \pm 0.3$ eV. As expected, the cross sections are unreliable when the value of E_{lab} is comparable to ΔE_{lab}. At $E_{cm} \geq 1.3$ eV, the cross sections measured using an O^+ ion beam with $\Delta E_{lab} = \pm 0.3$ eV are slightly higher than the corresponding cross sections with $\Delta E_{lab} = \pm 1.5$ eV. However, at $E_{cm} \geq 1.3$ eV, the cross sections obtained for $\Delta E_{lab} = \pm 0.3$ and ± 1.5 eV agree after taking into account the experimental uncertainties. Rejecting the cross sections for NO^+ at $E_{cm} < 1.3$ eV obtained using the O^+ reactant ion beam with $\Delta E_{lab} = \pm 1.5$ eV, the NO^+ cross section curve exhibits a maximum value of 5.7 $Å^2$ at $E_{cm} \approx 3.8$-5.1 eV ($E_{lab} \approx 6$-8 eV) and is in excellent agreement with that measured previously using $O^+(^4S)$ reactant ions formed by dissociative photoionization of O_2.[16]

The ΔE_{lab} value for a reactant ion beam prepared by photoionization usually is better defined compared to that formed by an electron impact ion source or an ion-molecule reaction

Figure 4 Absolute total cross sections in the E_{lab} range of 0.15-30 eV for NO^+ formed by reaction (2). (○): cross sections measured using the original $O^+(^4S)$ ion beam prepared by reaction (3) with $\Delta E_{lab} = \pm 1.5$ eV; (●): cross section measured by applying the DRP method to improve the kinetic energy resolution of the $O^+(^4S)$ to $\Delta E_{lab} = \pm 0.3$ eV.

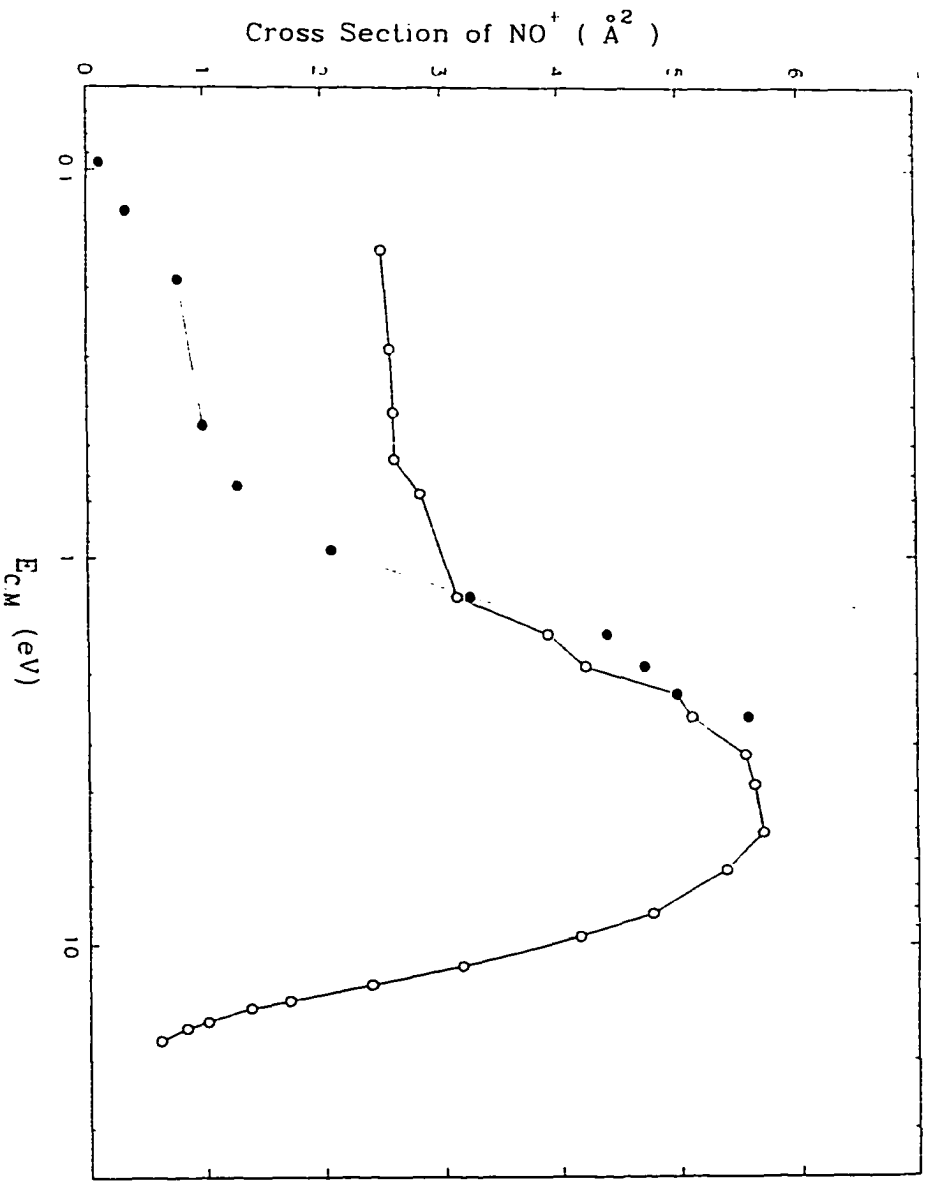
Cross Section of NO+ (Å2)
0
1
2
3
4
5
6
0.1
1
10
E_CM (eV)

ion source as described above, so an example of applying the DRP method to such a reactant ion beam is not given here. The application of the DRP method to an ion beam with a better kinetic energy resolution, such as that prepared in photoionization, should allow the cross section measurements to be made at collision energies $E_{lab} < 0.1$ eV.

IV. Conclusion

We have demonstrated that the kinetic energy resolution for a reactant ion beam can be improved significantly by using a simple DRP method. Since the method does not require a careful design of the ion optics system, it can be applied readily in existing ion-molecule reaction apparatuses to extend cross section measurements to lower collision energies, despite the fact that the original reactant ion beam has a broad kinetic energy distribution, such as in the case of a reactant ion beam prepared by ion-molecule collisions.

Acknowledgements:

This work is supported by National Science Foundation grant ATM 9200785.

References

1. A. Dalgarno and J. L. Fox, in "*Unimolecular and Bimolecular Ion-Molecule Reaction Dynamics*", C. Y. Ng, T. Baer, and I. Powis, eds. (Wiley, Chichester, 1994), p. 1.
2. R. A. Dressler and E. Murad, in "*Unimolecular and Bimolecular Ion-Molecule Reaction Dynamics*", C. Y. Ng, T. Baer, and I. Powis, eds. (Wiley, Chichester, 1994), p. 87..
3. M. A. Smith, in "*Unimolecular and Bimolecular Ion-Molecule Reaction Dynamics*", C. Y. Ng, T. Baer, and I. Powis, eds. (Wiley, Chichester, 1994), p. 87.
4. P. A. Armentrout, in "*Gas Phase Inorganic Chemistry*", D. H. Russell, ed. (Plenum, New York, 1989), p. 1.
5. C. Y. Ng, in "*Techniques for the Study of Gas-Phase Ion-Molecule Reactions*", J. M. Farrar and W. H. Saunder, Jr., eds. (Wiley, New York, 1988), p.417.

6. C. Y. Ng, in "*State-Selected and State-to-State Ion-Molecule Reaction Dynamics: I. Experiment*", C. Y. Ng and M. Baer, eds. (Wiley, New York, 1992), p. 401.

7. D. Gerlich, in "*State-Selected and State-to-State Ion-Molecule Reaction Dynamics: I. Experiment*", C. Y. Ng and M. Baer, eds. (Wiley, New York, 1992), p. 1.

8. F. H. Field and J. L. Franklin, "*Electron Impact Phenomena and the Properties of Gaseous Ions*" (Academic Press, New York, 1970), revised edition.

9. R. E. Fox, W. H. Hickam, D. J. Grove, and T. Kjeldaas, Jr., *Rev. Sci. Instrum.* 26, 1101 (1955).

10. S. G. Lias, J. E. Bartmess, J. F. Liebman, J. L. Holmes, R. D. Levin, and W. G. Mallard, *J. Phys. Chem. Ref. Data* 17, Suppl. No. 1 (1988).

11. C. E. Moore, "*Atomic Energy Levels*", Natl. Bur. Stand. (U.S.) Cir. No. 467 (U. S. GPO, Washington, D. C. 1949), Vol. I.

12. G. O. Brink, *Rev. Sci. Instrum.* 37, 857, 1626 (1966).

13. N. R. Daly, *Rev. Sci. Instrum.* 31, 264 (1960).

14. P. J. Chantry, *J. Chem. Phys.* 55, 2746 (1971).

15. G. D. Flesch, S. Nourbakhsh, and C. Y. Ng, *J. Chem. Phys.* 92, 3590 (1990).

16. G. D. Flesch and C. Y. Ng, *J. Chem. Phys.* 92, 3235 (1990); and references therein.

17. H. M. Rosenstock, K. Draxl, B. W. Steiner, and J. T. Herron, "Energetics of Gaseous Ions", *J. Phys. and Chem. Ref. Data*, **6**, Suppl. 1 (1977).

18. I. Koyano and K. Tanaka, in "*State-Selected and State-to-State Ion-Molecule Reaction Dynamics: I. Experiment*", C. Y. Ng and M. Baer, eds. (Wiley, New York, 1992), *Adv. Chem. Phys.* Vol. **82**, p. 263.

19. J. C. Weisshaar, in "*State-Selected and State-to-State Ion-Molecule Reaction Dynamics: I. Experiment*", C. Y. Ng and M. Baer, eds. (Wiley, New York, 1992), *Adv. Chem. Phys.* Vol. **82**, p. 213.

20. S. L. Anderson, in *"State-Selected and State-to-State Ion-Molecule Reaction Dynamics: I. Experiment"*, C. Y. Ng and M. Baer, eds. (Wiley, New York, 1992), *Adv. Chem. Phys.* Vol. **82**, p. 177.

CHAPTER III

A STATE-SELECTED STUDY OF THE ION-MOLECULE REACTIONS $O^+(^4S,^2D,^2P) + N_2$

A paper submitted to the Journal of Physical Chemistry

X. Li, Y.-L. Huang, G. D. Flesch and C.Y. Ng

Abstract:

Absolute state-selected cross sections for the reactions $O^+(^4S,^2D,^2P)+N_2 \rightarrow N_2^+ + O$, $NO^+ + N$, and $N^+ + NO$ (and/or $N^+ + N + O$) have been measured in the center-of-mass collision energy ($E_{c.m.}$) range of 0.06-40 eV employing the differential retarding potential method and the $O^+(^2D)$ and $O^+(^2P)$ ion state-selection schemes we developed recently. Charge transfer is the overwhelming product channel for the $O^+(^2D)+N_2$ and $O^+(^2P)+N_2$ reactions. Contrary to the results of previous experiments, the charge transfer cross sections for $O^+(^2P)+N_2$ is found to be 30-100% greater than those for $O^+(^2D)+N_2$. This observation suggests that N_2 is an excellent quenching gas for $O^+(^2D,^2P)$. While the $E_{c.m.}$ dependencies for the cross sections of NO^+ from $O^+(^4S)+N_2$ and $O^+(^2D)+N_2$ are similar, exbibiting a broad maximum in the $E_{c.m.}$ range 1.5-8 eV, the cross section for NO^+ from $O^+(^2P)+N_2$ is found to decrease as $E_{c.m.}$ is decreased. The N^+ signal observed in the $O^+(^4S)+N_2$ reaction is attributed to the formation of $N^+ + N + O$. The pathway of $O^+ + N_2 \rightarrow N^+ + NO$ to

generate N^+ is strongly suggested as the major channel in the reactions of $O^+(^2D,^2P) + N_2$, as evidenced by the observation of N^+ well below the thermochemical thresholds of $O^+(^2D,^2P) + N_2 \rightarrow N^+ + N + O$.

I. INTRODUCTION

Ions existing in planetary atmospheres are mostly produced by solar ultraviolet and vacuum ultraviolet (VUV) photodissociation and photoionization processes.[1-3] The $O^+(^4S)$ ions, together with the metastable $O^+(^2D)$ and $O^+(^2P)$, are the most abundant ion in the F-region of the Earth's ionosphere.[4-7] Through ion-molecule reactions, these O^+ atomic ions influence the densities and the temperatures of electrons, ions and neutral molecules in the ionosphere. Therefore, the study of relevant ion-molecule processes involving $O^+(^4S)$, $O^+(^2D)$, and $O^+(^2P)$ is important for modeling the chemistry of the atmospheres.[7-9]

It is well known that the rates of radiative recombination of O^+ with electrons are several orders of magnitude smaller than those of dissociative recombination of N_2^+, O_2^+, and NO^+ with electrons.[10,11] The major decay mechanism for $O^+(^4S,^2D,^2P)$ involves reactions with N_2 and O_2, leading to the formation of N_2^+, O_2^+, and NO^+ etc. Thus, the $O^+(^4S,^2D,^2P) + N_2$ reactions constitute one of the important sets of ion-molecule reactions in the ionosphere.[3,7-9]

The reactions of ground state $O^+(^4S) + N_2$ have been well studied by a variety of techniques[12,13]. The possible product channels and their energetics[14-16] for the reaction of $O^+(^4S) + N_2$ are given below.

$$O^+(^4S) + N_2 \rightarrow N_2^+ + O \qquad \Delta H^\circ = 1.97 \text{ eV} \qquad (1)$$

$$\rightarrow NO^+ + N \qquad \Delta H^\circ = -1.09 \text{ eV} \qquad (2)$$

$$\rightarrow N^+ + NO \qquad \Delta H^\circ = 4.17 \text{ eV} \qquad (3)$$

$$\rightarrow N^+ + N + O \qquad \Delta H^\circ = 10.71 \text{ eV} \qquad (4)$$

Unless specified, the atomic and molecular neutrals and ions involved in reactions (1)-(4) are assumed to be in their ground states. The absolute cross sections for processes (1), (2), and (4) covering the center-of-mass kinetic energies ($E_{c.m.}$) from thermal energies to 127 eV have been reported.[12,13] Reaction (3) is shown to be unimportant in the experiment of Flesch and Ng.[12]

Due to the difficulty of preparing state-selected metastable $O^+(^2D)$ and $O^+(^2P)$ ion beams, the reactions involving these ions have not been examined in detail previously. The metastable $O^+(^2D)$ and $O^+(^2P)$ states lie 3.324 eV and 5.017 eV above the $O^+(^4S)$ ground state and have radiative lifetimes of 3.6 hr and 4.57 s, respectively.[3,7-9,15] The $O^+(^2D,^2P)$ states can be produced together with the ground $O^+(^4S)$ state by electron impact[17,18] or by dissociative charge transfer (DCT) of $He^+ + O_2$ [reaction (5)] [19-23] and $Ne^+ + O_2$ [reaction (6)].[23,24]

$$He^+ + O_2 \rightarrow He + O^+(^4S,^2D,^2P) + O \qquad (5)$$

$$Ne^+ + O_2 \rightarrow Ne + O^+(^4S,^2D) + O \qquad (6)$$

Such O^+ sources have been used to measure cross sections[17,22] or reaction rates[19-21] of O^+ with N_2. The abundances of $O^+(^4S)$, $O^+(^2D)$, and $O^+(^2P)$ thus formed are often difficult to evaluate. With the $He^+ + O_2$ source, Rowe *et al.*[19] and Johnsen and Biondi[20,21] report rate constants for $O^+ + N_2$ assuming that $O^+(^2D)$ is the predominant ion formed in reaction (5). In the high resolution cross-beam experiment by Bischof and Linder[24] and the ion beam-gas cell study by Gerlich and co-worker,[5] the branching ratios for $O^+(^4S)$, $O^+(^2D)$, and $O^+(^2P)$

formed in reaction (5) have been measured as a function of $E_{c.m.}$. They find that more than 60% of the O^+ ions formed at thermal energies are in the $O^+(^2P)$ state, contrary to the assumption of Rowe, *et al.*[19] and Johnsen and Biondi.[20,21] Since then, different experimental techniques and procedures have been proposed to study the state-specific reactions involving $O^+(^2D)$ and $O^+(^2P)$. Among them, Lavollée and Henri[27] propose an extension of the threshold photoelectron-photoion coincidence technique (TPEPICO), which is based on the resonance dissociative photoionization of O_2 via the $O_2^+(III^2\Pi_u)$ predissociative state. The ratio of the cross section for NO^+ due to $O^+(^2P)$ to that due to $O^+(^2D)$ is reported.[27] However, the TPEPICO method suffers from low signal-to-noise ratios, and its application for extensive cross section measurements is impractical.

In the cross section measurements of $O^+(^4S,^2D,^2P) + N_2$, Flesch and Ng[24] have prepared $O^+(^4S)$ by dissociative photoionization of O_2, along with mixtures of $O^+(^4S,^2D,^2P)$ and $O^+(^4S,^2D)$ formed by reactions (5) and (6), respectively. By using the branching ratios for $O^+(^4S)$, $O^+(^2D)$, and $O^+(^2P)$ determined by Bischof and Linder[25] and known absolute cross sections for reactions (1), (2), and (4),[12,13] estimates for absolute cross sections of the $O^+(^2D) + N_2$ and $O^+(^2P) + N_2$ reactions have been obtained by deconvolution procedures.[24]

We have recently demonstrated a method for the preparation of state-specific $O^+(^2D)$ and $O^+(^2P)$ ion beams with sufficiently high intensities for scattering experiments.[23] This method involves the combination of the DCT reactions (5) and (6) and the RF octopole ion trap (OIT) techniques.[26] In order to improve the kinetic energy resolution for $O^+(^2D)$ and $O^+(^2P)$ ion beams prepared by the DCT-OIT method, we have also developed a differential

retarding potential (DRP) scheme[28]. Applying the DCT-OIT and DRP methods, we have obtained absolute cross sections for a series of atmospheric ion-molecule reactions involving $O^+(^2D)$ and $O^+(^2P)$ covering the $E_{c.m.}$ range from near thermal energies to ≈50 eV.[29] Here, we report the results for the $O^+(^2D) + N_2$ and $O^+(^2P) + N_2$ reactions. Cross sections for these reactions are compared to those for $O^+(^4S) + N_2$.[12,13]

II. EXPERIMENT

The experimental arrangement and procedures for cross section measurements using the triple-quadruple double-octopole (TQDO) apparatus (Fig. 1) have been described previously in detail[30-33]. The TQDO apparatus essentially consists of, in sequential order, a VUV photoionization ion source or an electron impact ionization ion source (1), a reactant quadruple mass spectrometer (QMS) (5), a lower radio frequency (RF) octopole ion guide reaction gas cell (RFOIGGC) [(6) + (7)], a middle QMS (10), an upper RFOIGGC [(11) + (14)], a product QMS (15), and a Daly-type scintillation ion detector[34] [(17) + (19) + (20)]. The electron impact ionization ion source used here is of the Brink design[35] and has been added to the TQDO apparatus recently. The TQDO apparatus is partitioned into five chambers which are separately evacuated by liquid nitrogen- or freon-trapped diffusion pumps. The differential pumping arrangement is important for the reactant ion preparation scheme and the cross section measurement experiments described here.

Here $O^+(^4S)$, $O^+(^2D)$ and $O^+(^2P)$ reactant ions are produced by the DCT processes (7), (6) and (5), respectively.

Figure 1 Schematic diagram of the TQDO apparatus. (1) electron impact ionization ion source, (2) atomic or molecular nozzle beam, (3) to freon-trapped 6" diffusion pump (DP), (4) to liquid-nitrogen (LN_2)-trapped 6" DP, (5) reactant QMS, (6) lower RF octopole ion guide, (7) lower RFOIGGC, (8) to LN_2-trapped 6" DP, (9) the lower RF octopole ion guide chamber, (10) middle QMS, (11) upper RF octopole ion guide, (12) to LN_2-trapped 4" DP, (13) upper RF octopole ion guide chamber, (14) upper RFOIGGC, (15) product QMS, (16) detector chamber, (17) plastic scintillator window, (18) to LN_2-trapped 2" DP, (19) photomultiplier tube, (20) aluminum ion target.

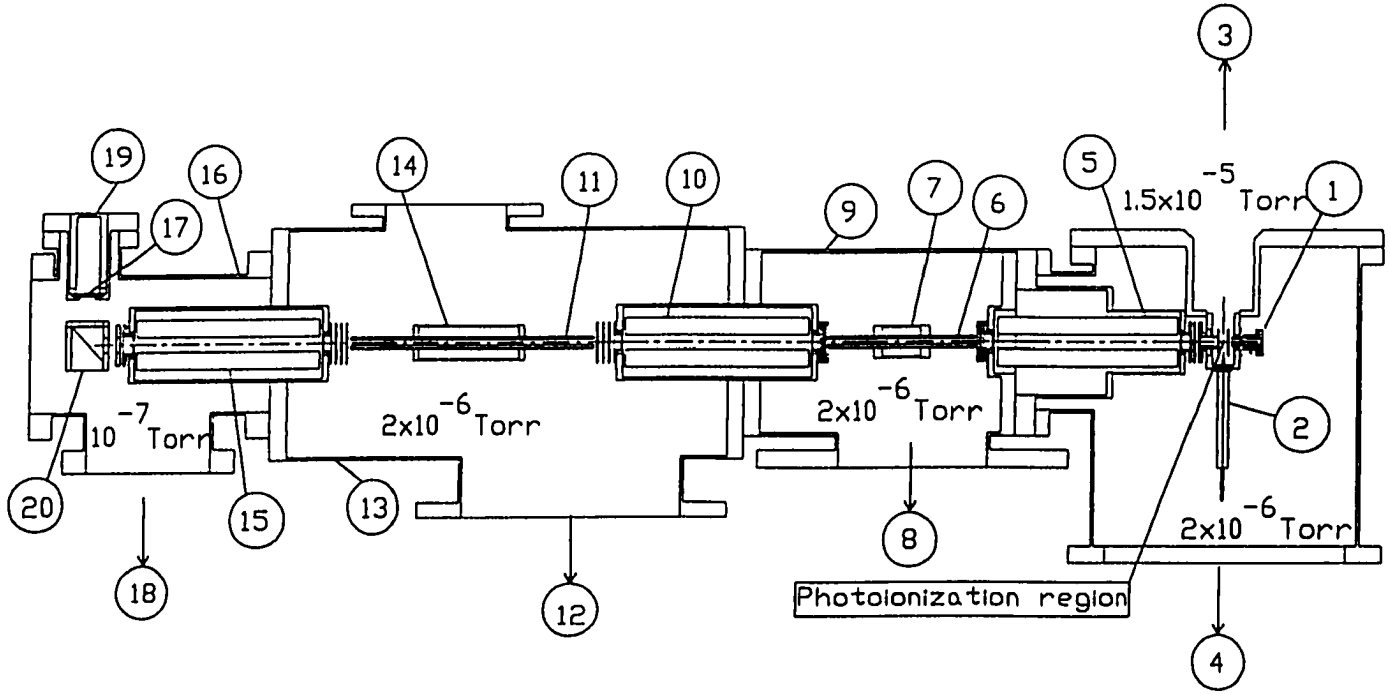
3
19
16
14
11
10
9
7
6
5
1.5x10 -5 Torr
1
17
10 -7 Torr
2x10 -6 Torr
2x10 -6 Torr
2
20
15
13
8
2x10 -6 Torr
18
12
Photoionization region
4

$$Ar^+ + O_2 \quad \rightarrow \quad O^+(^4S) + O(^3P) + Ar \qquad \Delta H^\circ = 2.97 \text{ eV} \qquad (7)$$

Basically, rare gas ions (He^+, Ne^+, or Ar^+,) are generated in the ionization region by electron impact. These ions are then extracted from the ionization region and mass-selected by the reactant QMS. The DCT reactions (5), (6), or (7) take place in the lower gas cell, into which oxygen gas has been introduced. It is our finding that by limiting the $E_{c.m.}$ to below 2.9 eV for collisions between Ar^+ and O_2, reaction (7) produces $O^+(^4S)$ only. Comparative studies have shown that the $O^+(^4S)$ source based on reaction (7) is identical to that based on the dissociative photoionization of O_2.[12] However, the $O^+(^4S)$ reactant ion beam generated by reaction (7) has an intensity more than 400 fold greater than that prepared by dissociative photoionization of O_2. In reaction (5), which is exothermic, a mixture of $O^+(^4S)$, $O^+(^2D)$, and $O^+(^2P)$ are produced with well resolved kinetic energy distributions.[25,26] At $E_{c.m.}$ = 1-2 eV, $O^+(^2P)$ ions have lower kinetic energies than those for $O^+(^4S)$ and $O^+(^2D)$, and are found to be the dominant product channel with a branching ratio of 50-60%. The idea of the state-selection method is to lower the trapping voltage of the lower RF octopole so that energetic $O^+(^4S)$ and $O^+(^2D)$ ions escape from the octopole trap and slow $O^+(^2P)$ ions remain trapped for scattering studies. This is essentially an $O(^2P)$ enrichment scheme. Under the present experimental conditions, which maximize the transmission fraction for $O^+(^2P)$, we estimate that the $O^+(^2P)$ ion beam has a purity of 89% with the remaining fraction being about 5% each for $O^+(^4S)$ and $O^+(^2D)$.[23] The formation of $O^+(^2D)$ and $O^+(^2P)$ from reaction (6) is endothermic by 0.48 (0.38)[36] and 2.18 (2.10)[36] eV, respectively. Thus, the formation of $O^+(^2P)$ can be avoided at $E_{c.m.} < 2.1$ eV. The $E_{c.m.}$ dependence of the cross section for

reaction (6) reveals a sharp onset at the thermochemical threshold for the formation of $O^+(^4D)$, indicating that the formation of $O^+(^2D)$ is efficient,[24] in accordance with the DCT mechanism.[32,37,38] By choosing $E_{c.m.} = 0.73$ eV and by lowering the effective trapping potential of the RF octopole ion trap to lose the $O^+(^4S)$ ions, we estimate that the $O^+(^2D)$ ion beam used in the present experiment has a purity ≥90%.[23]

The state-selected $O^+(^2D)$ [$O^+(^2P)$] ions thus formed are mass-selected by the middle QMS and transmitted into the upper gas cell where the reactions between $O^+(^2D)$ [$O^+(^2P)$] and N_2 occur. The N_2 gas cell pressures used in this experiment are $\leq 2\times10^{-4}$ Torr. The product ions are detected using the upper QMS and the Daly-type scintillation ion detector. At each $E_{c.m.}$, the product ion collection efficiency is maximized by carefully optimizing the transmission of the ion lenses, product QMS, and the octopole ion guide.

The laboratory kinetic energies for the Ar^+, Ne^+, He^+ and O^+ ion beams are measured by the retarding potential method, which has been detailed previously,[31] in the energy range above $E_{c.m.} = 2$ eV. Because of the relatively large energy spread of $O^+(^4S)$, $O^+(^2D)$, and $O^+(^2P)$ reactant ions generated by reactions (5), (6), and (7), respectively, the DRP method is used to improve the energy definition of O^+ in the $E_{c.m.}$ range below 2 eV. The energy resolution achieved for $E_{c.m.}$ in this study using the DRP method is $\pm$0.06 eV.

The pressures in the lower and upper reaction gas cell are measured by two separate MKS Baratron gauges. The gas pressures in both the lower and the upper reaction gas cells are kept $< 3\times10^{-4}$ Torr. In this pressure range, the cross sections of NO^+, N_2^+, N^+ are constant. Since the upper reaction gas cell is open ended, N_2 gas introduced into the gas cell

diffuses into the reaction chamber and forms a background pressure. This part of the diffused N_2, which is outside the cell but within the octopole rod structure, also reacts with $O^+(^4S,^2D,^2P)$ to produce N_2^+, NO^+, and N^+. The cross sections for the product ions reported here have been corrected for this background contribution. The uncertainties for the absolute cross sections reported here are estimated to be $\leq$ 25%. However, the uncertainties for relative cross sections are believed to be smaller than 10%.

III. Results and Discussion

The possible reactions and their energetics[14-16] involving $O^+(^4S,^2D,^2P)$ with N_2 are:

$$O^+(^2D) + N_2 \rightarrow N_2^+(X^2\Sigma_g^+) + O \qquad \Delta H^\circ = -1.35 \text{ eV} \qquad (8a)$$

$$\rightarrow N_2^+(A^2\Pi_u) + O \qquad \Delta H^\circ = -0.22 \text{ eV} \qquad (8b)$$

$$\rightarrow NO^+(X^1\Sigma^+) + N \qquad \Delta H^\circ = -4.41 \text{ eV} \qquad (9a)$$

$$\rightarrow NO^+(X^1\Sigma^+) + N(^2D) \qquad \Delta H^\circ = -2.07 \text{ eV} \qquad (9b)$$

$$\rightarrow NO^+(X^1\Sigma^+) + N(^2P) \qquad \Delta H^\circ = -0.80 \text{ eV} \qquad (9c)$$

$$\rightarrow N^+ + NO \qquad \Delta H^\circ = 0.85 \text{ eV} \qquad (10)$$

$$\rightarrow N^+ + N + O \qquad \Delta H^\circ = 7.39 \text{ eV} \qquad (11)$$

$$O^+(^2P) + N_2 \rightarrow N_2^+(X^2\Sigma_g^+) + O \qquad \Delta H^\circ = -3.05 \text{ eV} \qquad (12a)$$

$$\rightarrow N_2^+(A^2\Pi_u) + O \qquad \Delta H^\circ = -1.91 \text{ eV} \qquad (12b)$$

$$\rightarrow N_2^+(A^2\Pi_u) + O(^1D) \qquad \Delta H^\circ = 0.03 \text{ eV} \qquad (12c)$$

$$\rightarrow N_2^+(X^2\Sigma_g^+) + O(^1D) \qquad \Delta H^\circ = -1.16 \text{ eV} \qquad (12d)$$

$$\rightarrow N_2^+(B^2\Sigma_u^+) + O \qquad \Delta H^\circ = 0.116 \text{ eV} \qquad (12e)$$

$$\rightarrow NO^+(X^1\Sigma^+) + N \qquad \Delta H^\circ = -6.11 \text{ eV} \qquad (13a)$$

$\rightarrow NO^+(X^1\Sigma^+) + N(^2D)$ $\Delta H° = -3.77$ eV (13b)

$\rightarrow NO^+(X^1\Sigma^+) + N(^2P)$ $\Delta H° = -2.50$ eV (13c)

$\rightarrow NO^+(a^3\Sigma^+) + N$ $\Delta H° = 0.38$ eV (13c)

$\rightarrow N^+ + NO$ $\Delta H° = -0.85$ eV (14)

$\rightarrow N^+ + N + O.$ $\Delta H° = 5.69$ eV (15)

In the calculations of $\Delta H°$ values for these reactions, the neutrals and ions are assumed to be in their ground states unless otherwise specified. In the $E_{c.m.}$ range of interest in the present experiment, charge transfer product N_2^+ ions may be formed in the $N_2^+(X^2\Sigma_g^+, A^2\Pi_u)$ [reactions 8(a) and 8(b)] and $N_2^+(X^2\Sigma_g^+, A^2\Pi_u, B^2\Sigma_u^+)$ [reactions 12(a)-12(e)] states in the reactions of $O^+(^2D) + N_2$ and $O^+(^2P) + N_2$, respectively. The O atoms formed in the charge transfer collisions of $O^+(^2P) + N_2$ can be in the ground $O(^3P)$ as well as excited $O(^1D)$ states. The metastable $N(^2D)$ and $N(^2P)$ states are 2.34 and 3.61 eV above the ground $N(^4S)$ state, respectively.[15] Thus, these metastable $N(^2D,^2P)$ atoms can be formed, together with NO^+, in reactions 9(b), 9(c), 13(b), and 13(c). Furthermore, NO^+ in the excited $NO^+(a^3\Sigma^+)$ state can also be produced in reaction 13(d).

A. $O^+(^4S) + N_2$

We have re-measured the absolute cross sections for N_2^+, NO^+, and N^+ from $O^+(^4S) + N_2$ using the $O^+(^4S)$ reactant ions prepared by the DCT reaction (7). The cross sections for NO^+ (solid triangles), N_2^+ (solid squares), and N^+ (solid circles) from $O^+(^4S) + N_2$ in the $E_{c.m.}$ range of 0.09-40 eV are plotted in Fig. 2. As shown below, the favorable comparison between these cross sections and those for $O^+(^4S)+N_2$ obtained in previous studies[12,13]

Figure 2 Cross sections for N_2^+ (filled squares), NO^+ (filled triangles), and N^+ (filled circles) from $O^+(^4S) + N_2$ in the $E_{c.m.}$ range of 0.09-40 eV. The thermochemical thresholds for reactions (2) and (4) are marked by the arrows.

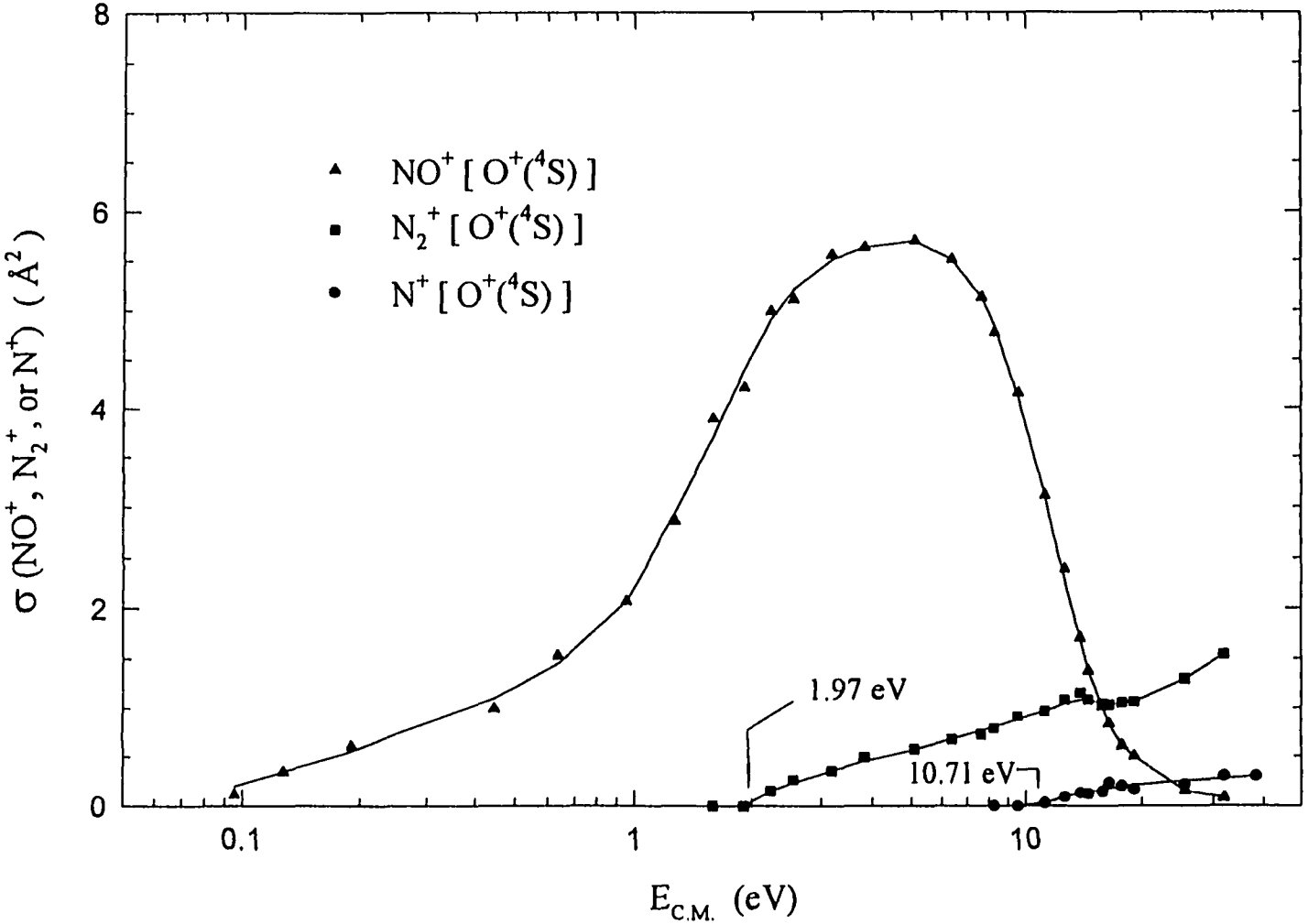
8
6
4
2
0
0.1
1
10
σ (NO^+, N_2^+, or N^+) ($Å^2$)
$E_{C.M.}$ (eV)
NO^+ [$O^+(^4S)$]
N_2^+ [$O^+(^4S)$]
N^+ [$O^+(^4S)$]
1.97 eV
10.71 eV

validates the DCT and DRP methods employed in the present study.

The cross sections for NO^+, which exhibit a broad maximum of 5.8 $Å^2$ at $E_{c.m.}$ = 5-6eV are in general agreement with those reported by Flesch and Ng and Burley *et al.*[12,13] As pointed out previously, the rapid decline in NO^+ cross section occurs at $E_{c.m.}$ close to the thermochemical threshold of 10.71 eV for reaction (4), indicating that further dissociation of excited NO^+ to $O^+ + N$ at $E_{c.m.} > 10.71$ eV may in part account for the sharp drop in NO^+ cross sections. Previous experiments reveal that the NO^+ cross section increases from $E_{c.m.} \approx 0.3$ eV toward lower $E_{c.m.}$. The NO^+ cross section curve of Fig. 2 does not exhibit such a feature. This may be due to the imprecision of the DRP method, which has a lower $E_{c.m.}$ limit of about 0.06 eV for this experiment. Furthermore, since the DRP method is basically a substraction technique, the S/N ratios are poorer for the low absolute NO^+ cross sections at $E_{c.m.} < 0.3$ eV.

The cross sections observed for the charge transfer product N_2^+ clearly reveal the thermochemical threshold of 1.97 eV for reaction (1), as marked in Fig. 2. As has been observed by Flesch and Ng,[12] the N_2^+ cross sections at $E_{c.m.} > 10.7$ eV do not decline rapidly, contrary to what Burley *et al.* have observed.[13] Instead, the cross sections slowly increase beyond $E_{c.m.} \approx 10.7$ eV and reach a value of ≈ 1.5 $Å^2$ at $E_{c.m.}$ = 32 eV, consistent with the observation of Ref. 12.

Since the N^+ signals at $E_{c.m.}$ below the threshold of reaction (4) are negligible, we conclude that reaction (3), which has a threshold of 4.17 eV, is not a likely channel for producing N^+. Also, as has been reported in Ref. 12, the cross section for N^+ increases from

Figure 3 Cross sections for N_2^+ (filled squares), NO^+ (filled triangles), and N^+ (filled circles) from $O^+(^2D)$ + N_2 in the $E_{c.m.}$ range of 0.06-40 eV. The rate constants (k in cm^3/s) for the charge transfer channel calculated using Eq. (17) and the corresponding $\sigma(N_2^+)$ are shown as hollow squares. The thermochemical threshold for reaction (10) is marked by the arrow.

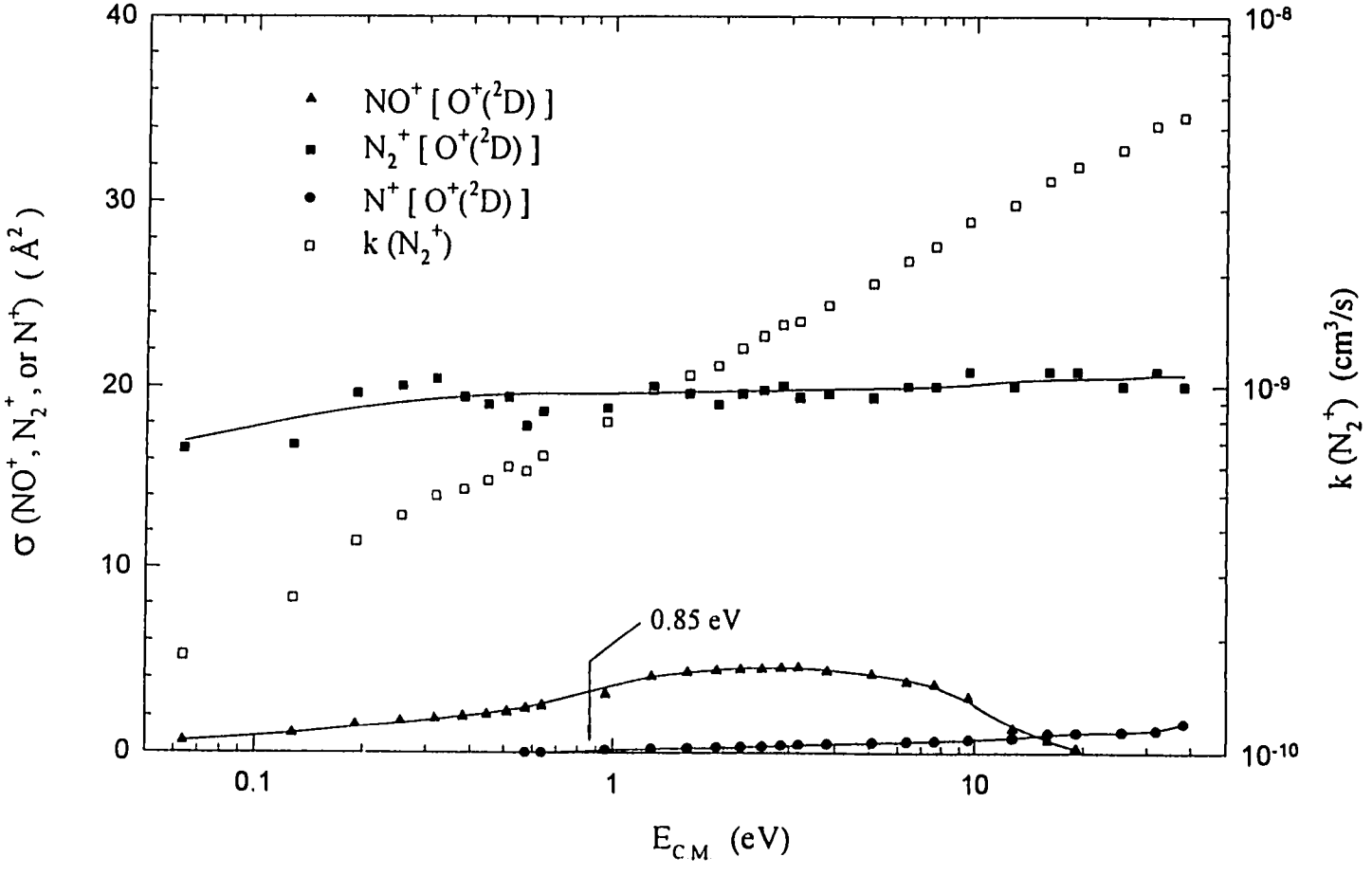
40
30
20
10
0
0.1
1
10
10^{-8}
10^{-9}
10^{-10}
NO^+ [$O^+(^2D)$]
N_2^+ [$O^+(^2D)$]
N^+ [$O^+(^2D)$]
k (N_2^+)
0.85 eV
σ (NO^+, N_2^+, or N^+) ($Å^2$)
k (N_2^+) (cm^3/s)
E_{CM} (eV)

the onset and becomes nearly constant at ≈0.4 Å^2 in the $E_{c.m.}$ range of 15-40 eV.

B. $O^+(^2D) + N_2$

Figure 3 shows the cross sections for NO^+ (solid triangles), N_2^+ (solid squares), and N^+ (solid circles) from $O^+(^2D) + N_2$ in the $E_{c.m.}$ range of 0.06-40 eV. Different from the $O^+(^4S) + N_2$ reaction, where NO^+ is the main product, the results of Fig. 3 show that the charge transfer channel dominates in the reaction of $O^+(^2D) + N_2$. The $N_2^+(A^2\Pi_u)$ state is 1.14 eV above the ground $N_2^+(X^2\Sigma_g^+)$ state.[16] Thus, the formation of $N_2^+(X^2\Sigma_g^+)$ as well as $N_2^+(A^2\Pi_u)$ in reactions (8a) and (8b) are exothermic. Rowe *et al.*[19] have proposed that the nearly energy resonant process

$$O^+(^2D) + N_2 \rightarrow N_2^+(A^2\Pi_u, v=1) + O(^3P) \qquad \Delta H^\circ = -0.02 \text{ eV} \qquad (16)$$

may account for the high charge transfer cross sections for $O^+(^2D) + N_2$. As shown in Fig. 3, the cross sections for N_2^+ are relatively constant at ≈20 Å^2 over the full $E_{c.m.}$ range of 0.06-40 eV. This value is lower than the values obtained in previous studies, which fall in the range of ≈25-40 Å^2.[22,24,27] Considering that the $O^+(^2D)$ ion beam formed by the DCT-OIT technique may contain up to 10% of $O^+(^4S)$ ions,[23] the values of 20 Å^2 for the charge transfer reaction of $O^+(^2D) + N_2$ obtained in the present study may be too low by ≈10%.

In accordance with the observation in previous studies,[22,24] the cross sections of NO^+ are significantly lower than that for the charge transfer channel in the reaction of $O^+(^2D) + N_2$. The $E_{c.m.}$ dependence for the cross section for NO^+ from $O^+(^2D) + N_2$ is different from that reported in Ref. 24, which is deduced from deconvolution procedures. This observation, together with the finding that the absolute cross sections for N_2^+ and NO^+ of Fig. 3 are similar

to those from the reactions of $O^+(^4S,^2D)$ + N_2 in the $E_{c.m.}$ range of 1.3-25 eV measured using a mixture of $O^+(^4S,^2D)$ reactant ions formed by reaction (6), indicates that the fraction of $O^+(^4S)$ assumed in Ref. 17 for the deconvolution procedures in arriving at the cross sections of NO^+ and N_2 from $O^+(^2D)$ + N_2 is too high.

It is interesting to observe that finite cross sections of N^+ exist well below the threshold of reaction (11), which produces N^+ + N + O. The N^+ signal is found to begin at $E_{c.m.} \approx 0.95$ eV which is close to the thermochemical threshold of 0.85 eV for reaction (10) as marked in Fig. 3. This observation is consistent with the conclusion that both channels (10) and (11) are viable.

The rate constant (k) can be calculated from the measured absolute cross section (σ) using the relation

$$k = v\sigma, \qquad (17)$$

where v [$= (2E_{c.m.}/\mu)^{1/2}$] is the relative velocity for the colliding O^+-N_2 pair with a reduced mass μ = 10.18 amu. The rate constants (hollow squares) for the charge transfer reaction calculated using the measured N_2^+ cross sections [$\sigma(N_2^+)$] for $O^+(^2D)$ + N_2 are included in Fig. 3. Since $\sigma(N_2^+)$ is nearly independent of $E_{c.m.}$, the plot of k versus $\ln E_{c.m.}$ is approximately linear. On the basis of linear extrapolation to thermal energies, i.e., assuming that the N_2^+ cross sections remain constant at ≈20 Å^2 down to thermal energies, we obtain an estimate of 1.5×10^{-10} cm^3/s for the charge transfer rate constant of $O^+(^2D)$ + N_2 at thermal energies. The latter value is comparable to that of the selected ion flow tube (SIFT) study by Glosik et al.[39] and that deduced from Atmosphere Explorer satellite data,[8,40] but significantly

lower than that of Rowe *et al.*[19] and the calculated gas-kinetic upper-limit of 9.7×10^{-10} cm^3/s.[41]

C. $O^+(^2P) + N_2$

The absolute cross sections for N_2^+, NO^+, and N^+ from the reaction of $O^+(^2P) + N_2$ in the $E_{c.m.}$ range of 0.06-40 eV are shown in Fig. 4. Similar to the observation for the $O^+(^2D) + N_2$ reaction, the charge transfer channel is overwhelmingly the major product channel. This may also be rationalized by the near energy resonant channel (12c) corresponding to the formation of $N_2^+(A^2\Pi_u) + O(^1D)$ with an endothermicity by 0.03 eV. The occurrence of channel (12c) may be confirmed by cross section measurements for N_2^+ in its threshold region, i.e., in $E_{c.m.}$ range $\leq$ 0.03 eV. Unfortunately we were not able to obtain reliable cross section data at $E_{c.m.} < 0.06$ eV by the DRP method[1]. Thus the threshold for process (12c) cannot be examined in this experiment. As shown in Fig. 4, the cross section for N_2^+ is nearly constant in the $E_{c.m.}$ range of 0.12-0.5 eV and increases slowly from about 26 Å^2 at ≈0.15 eV to ≈43 Å^2 at $E_{c.m.}$ = 30 eV. We note that the formation of $N_2^+(B^2\Sigma_u^+) + O$ [reaction (12e)] is endothermic by 0.13 eV. The rise in N_2^+ cross section at $E_{c.m.}$ ≈ 0.15 eV might correspond to the onset of process (12e). In a TPEPICO study, Lavollée and Henri[27] find that the charge transfer cross sections for $O^+(^2D) + N_2$ in the $E_{c.m.}$ range of 4.8-12.7 eV are larger than those for $O^+(^2P) + N_2$ with the ratio for $O^+(^2P)/O^+(^2D)$ ≈ 0.6 . Their estimate of the $O^+(^2D)$ cross section is ≈25 Å^2. Thus an $O^+(^2P)$ cross section of ≈15 Å^2 follows from their study, which is much lower than observed here. A possible explanation for this discrepancy is that the relatively high reactant gas pressure (Lavollée and Henri used a

Figure 4 Cross sections for N_2^+ (filled squares), NO^+ (filled triangles), and N^+ (filled circles) from $O^+(^2P) + N_2$ in the $E_{c.m.}$ range of 0.06-40 eV. The rate constants (k in cm^3/s) for the charge transfer channel calculated using Eq. (17) and the corresponding $\sigma(N_2^+)$ are shown as hollow squares.

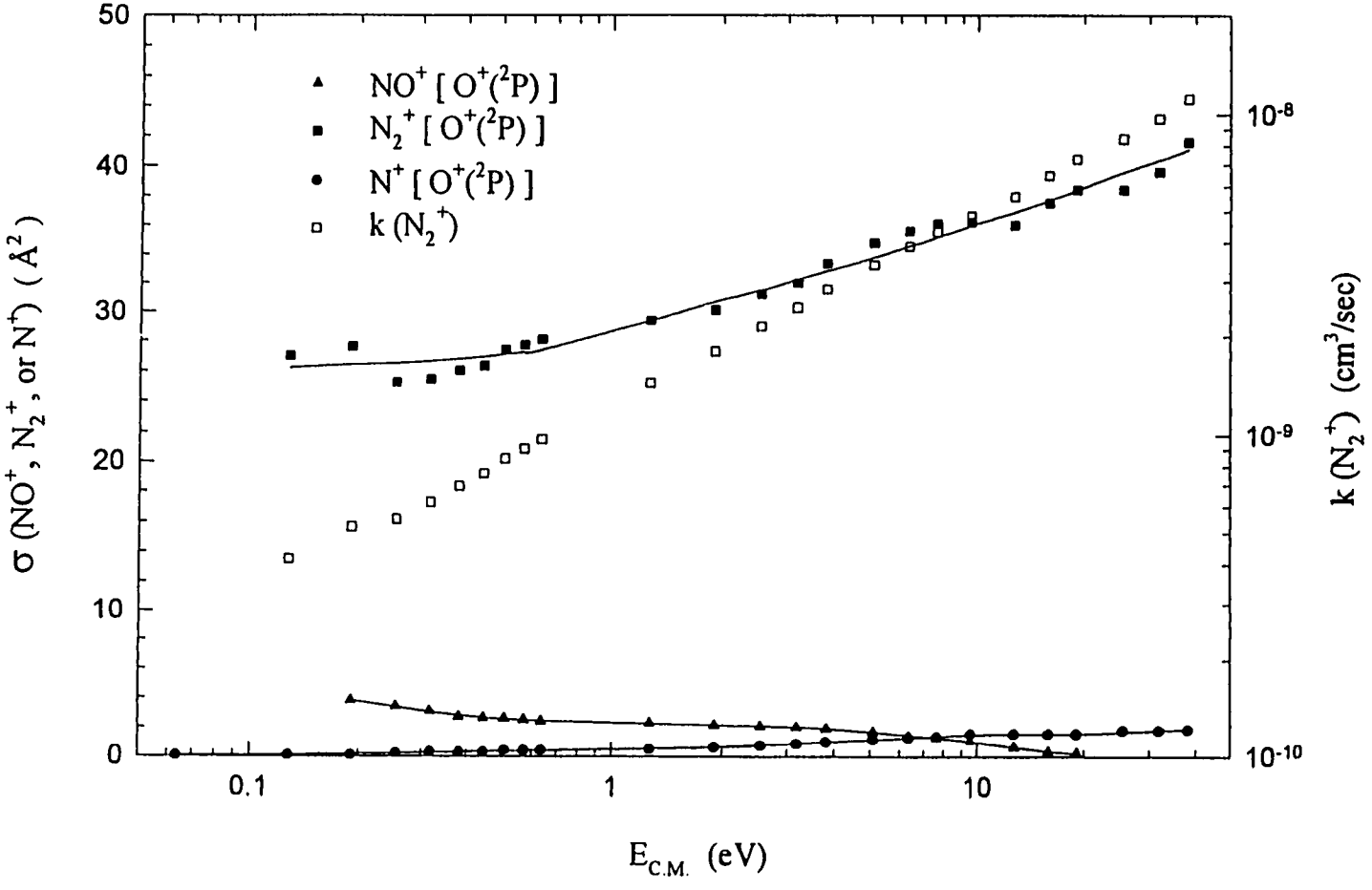
50
40
30
20
10
0
0.1
1
10
$E_{C.M.}$ (eV)
σ (NO^+, N_2^+, or N^+) ($Å^2$)
NO^+ [$O^+(^2P)$]
N_2^+ [$O^+(^2P)$]
N^+ [$O^+(^2P)$]
k (N_2^+)
10^{-8}
10^{-9}
10^{-10}
k (N_2^+) (cm^3/sec)

pressure of $\approx 10^{-3}$ Torr, compared to $\leq 2\times10^{-4}$ Torr used in our scattering gas cell) used at the ion-neutral scattering region in the TPEPICO experiment may cause collisional quenching processes according to the reactions

$$O^+(^2P) + N_2 \rightarrow O^+(^2D) + N_2 \quad (18)$$

$$O^+(^2P) + N_2 \rightarrow O^+(^4S) + N_2. \quad (19)$$

The rate constants (hollow squares in Fig. 4) for the charge transfer reaction of $O^+(^2P) + N_2$ have been calculated using Eq. (16) and the measured N_2^+ cross sections for $O^+(^2P) + N_2$. Since the rise in N_2^+ cross sections at $E_{c.m.} \geq 0.15$ eV is slow, the k versus $\ln E_{c.m.}$ is nearly linear. Assuming that the N_2^+ cross section at thermal energies is ≈ 26 Å^2, similar to those at $E_{c.m.} = 0.1$-0.5 eV, we obtain an estimate of 2.0×10^{-10} cm^{-3}/s for the rate constant of the charge transfer reaction $O^+(^2P) + N_2$ at thermal energies, which is larger than the value of 5.0×10^{-11} cm^{-3}/s from satellite measurements by Oppenheimer et al.[42] However, as noted in their publication, the thermosphere where the satellite measurements were taken has many mechanisms for the quenching process. Many of the rate constants of these quenching processes were not known and thus neglected in their deductions. So the value for thermal rate constant thus deduced may not be reliable. The SIFT study of Glosik, et al.[39] reports a rate constant of 1.35×10^{-10} cm^{-3}/s, which is in fair agreement with our estimate, within experimental errors.

The NO^+ cross section basically follows a decreasing pattern as the collision energy is increased. The cross section decreases from ≈ 4 Å^2 at $E_{c.m.} = 0.2$ eV to essentially zero at $E_{c.m.} \approx 20$ eV. Since the first excited $NO^+(a^3\Sigma^+)$ state is 6.47 eV above the ground

$NO^+(X^1\Sigma^+)$ state, the formation of excited $NO^+(a^3\Sigma^+)$ ions from reaction (13d) at $E_{c.m.} > 0.4$ eV should be possible.

The N^+ cross section for $O^+(^2P) + N_2$ increases slowly towards higher $E_{c.m.}$ just as it does for $O^+(^2D) + N_2$. The fact that we observe finite cross sections for N^+ down to $E_{c.m.} = 0.06$ eV suggests that channel (14) is open for $O^+(^2P) + N_2$, just as channel (10) is open for $O^+(^2D) + N_2$. Since the thermochemical threshold of channel (14) is -0.85 eV, this observation is not surprising.

We note that the cross sections for N_2^+, NO^+, and N^+ of Fig. 4 in the $E_{c.m.}$ of 1.8-21 eV are similar to those from $O^+(^4S,^2D,^2P) + N_2$ observed by Flesch and Ng,[24,43] where the $O^+(^4S,^2D,^2P)$ reactant ions are prepared by reaction (5). However, their conclusion that N_2^+ cross sections for $O^+(^2P) + N_2$ are lower than those for $O^+(^2D) + N_2$ is not supported by the present experiment. This discrepancy is due mostly to the erroneous fraction of $O^+(^4S)$ used in their deconvolution procedures for arriving at the cross sections for $O^+(^2D) + N_2$ and $O^+(^2P) + N_2$.

D. Comparison of N_2^+, NO^+, and N^+ cross sections from $O^+(^4S) + N_2$, $O^+(^2D) + N_2$ and $O^+(^2P) + N_2$

The cross sections for N_2^+, NO^+, and N^+ from reactions involving different O^+ electronic states in the $E_{c.m.}$ range of 0.06-40 eV are compared in Figs. 5(a), 5(b), and 5(c), respectively. As shown in Fig. 5(a), it is obvious that the charge transfer efficiencies of $O^+(^2P)$ and $O^+(^2D)$ to N_2 are significantly greater than that for $O^+(^4S)$ to N_2. The ratio of the N_2^+ cross section for $O^+(^2D) + N_2$ to that for $O^+(^2P)$ varies from ≈0.75 at $E_{c.m.} \approx 0.1$ eV to

Fgure 5 Comparison of (a) N_2^+, (b) NO^+, and (c) N^+ cross sections from reactions involving different $O^+(^4S, ^2D, ^2P)$ electronic states.

σT (Å2)
50
40
30
20
10
0
σT [O+(4S)]
σT [O+(2D)]
σT [O+(2P)]
kT [O+(4S)]
kT [O+(2D)]
kT [O+(2P)]
0.1
1
10
ECM. (eV)
10-8
10-9
10-10
kT (cm3/sec)

0.5 at $E_{c.m.}$ = 40 eV. This fact has been utilized to characterize the O^+ electronic states in our state selection study.[23]

Figure 5(b) shows that the profiles for the cross sections of NO^+ from $O^+(^4S) + N_2$ and $O^+(^2D) + N_2$ are similar except that the profile from $O^+(^2D) + N_2$ is shifted to lower $E_{c.m.}$ by ≈ 3 eV. It is interesting to note that the energy level of $O^+(^2D)$ is 3.3 eV higher than that of $O^+(^4S)$. The profile for the NO^+ cross section from $O^+(^2P) + N_2$ is different from those from $O^+(^4S,^2D) + N_2$, and reveals a decreasing trend as $E_{c.m.}$ is increased. The NO^+ cross sections from $O^+(^4S,^2D,^2P) + N_2$ become negligible at $E_{c.m.} > 25$ eV.

The N^+ cross sections for $O^+(^4S) + N_2$, $O^+(^2D) + N_2$, and $O^+(^2P) + N_2$ shown in Fig. 5(c) all exhibit an increasing trend as a $E_{c.m.}$ is increased. The profiles for the N^+ cross section curves associated with the excited states are shifted to lower $E_{c.m.}$'s with respect to that for the ground $O^+(^4S)$ state. As pointed out above, the N^+ cross section curves for $O^+(^4S) + N_2$ and $O^+(^2D) + N_2$ reveal distinct thresholds for reactions (4) and (10), respectively.

We have calculated the sum (σ_T) of the absolute cross sections for all products (N_2^+, NO^+, and N^+) channels in the $E_{c.m.}$ range of 0.06-40 eV for the individual reactions of $O^+(^4S) + N_2$, $O^+(^2D) + N_2$, and $O^+(^2P) + N_2$. Figure 6 compares the σ_T, i.e., $\sigma(N_2^+ + NO^+ + N^+)$, from $O^+(^4S) + N_2$, $O^+(^2D) + N_2$, and $O^+(^2P) + N_2$. The total rate constants (k_T) for these reactions calculated using Eq. (17) and the σ_T values are also depicted in Fig. 6. This comparison shows that the maximum σ_T values for $O^+(^2D) + N_2$ and $O^+(^2P) + N_2$ are relatively insensitive to $E_{c.m.}$. While the maximum σ_T value for $O^+(^4S) + N_2$ is only about 30% of the σ_T values for $O^+(^2D) + N_2$, the σ_T values for $O^+(^2P) + N_2$ are 50-100% greater

Figure 6 Comparison of σ_T's for the reactions $O^+(^4S) + N_2$ (solid circles), $O^+(^2D) + N_2$ (solid squares), and $O^+(^2P) + N_2$ (solid triangles). Here $\sigma_T = \sigma(N_2^+ + NO^+ + N^+)$. The total rate constant (k_T) calculated using Eq. (17) and corresponding σ_T's are also included. (hollow circles): $k_T[O^+(^4S)]$; (hollow squares): $k_T[O^+(^2D)]$; and (hollow triangles): $k_T[O^+(^2P)]$.

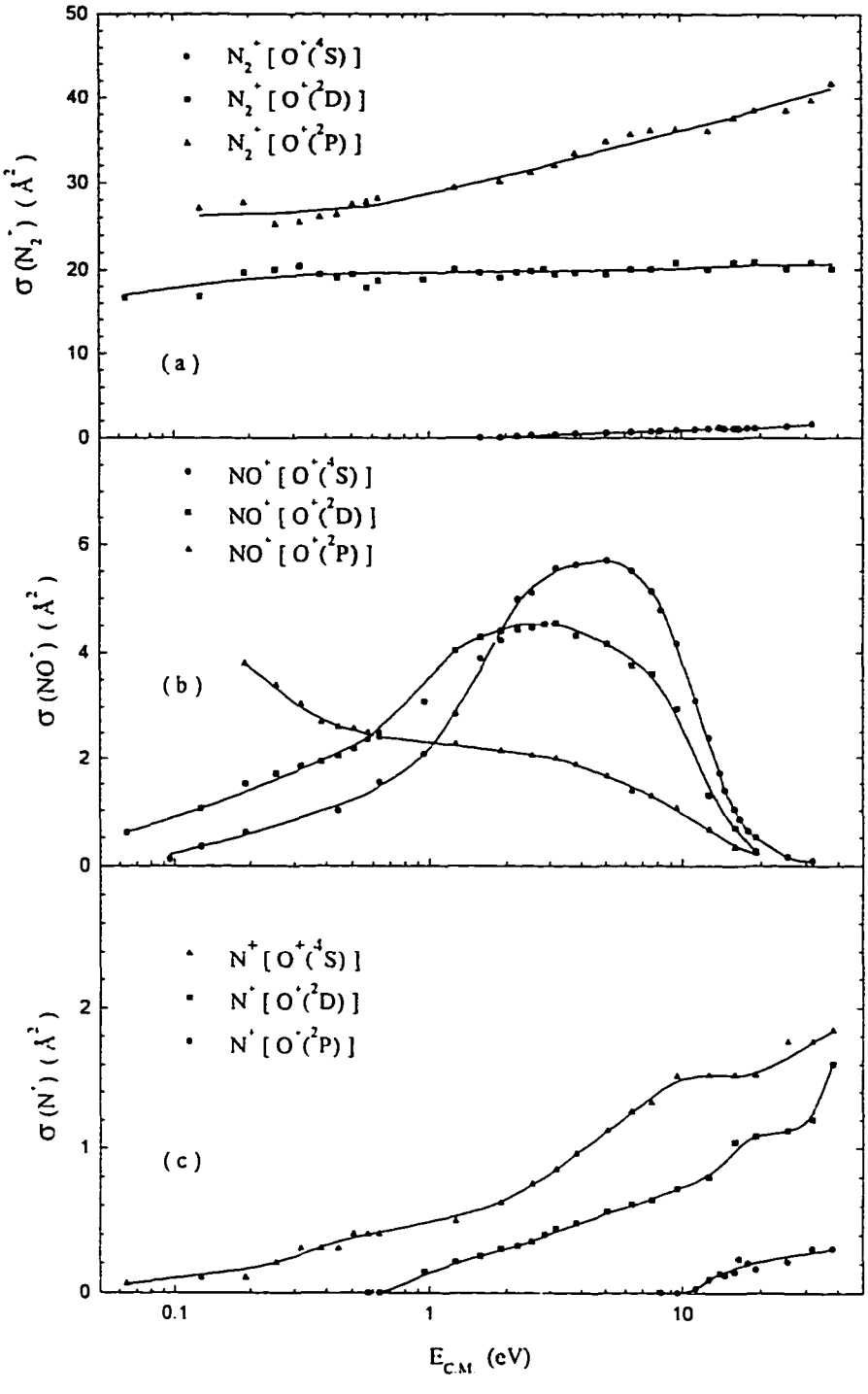
$N_2^+ [O^+(^4S)]$
$N_2^+ [O^+(^2D)]$
$N_2^+ [O^+(^2P)]$
(a)
$\sigma(N_2^+)$ (Å^2)
$NO^+ [O^+(^4S)]$
$NO^+ [O^+(^2D)]$
$NO^+ [O^+(^2P)]$
(b)
$\sigma(NO^+)$ (Å^2)
$N^+ [O^+(^4S)]$
$N^+ [O^+(^2D)]$
$N^+ [O^+(^2P)]$
(c)
$\sigma(N^+)$ (Å^2)
$E_{C.M.}$ (eV)

than those for $O^+(^2D)$ + N_2. The higher cross sections observed for reactions involving the excited states can be understood by the increased number of open product channels. This rationalization requires detailed theoretical support. It is our hope that the cross section data presented here will stimulate rigorious theoretical studies of the $[O+N_2]^+$ ion-molecule reaction system.

IV. Conclusions

Using the DCT reactions (5)-(7) to prepare reactant $O^+(^4S,^2D,^2P)$ ions, the differential retarding potential method for reaching to the lower collision energy region, and the state selection scheme to enrich single electronic state O^+ ions; we have been able to examine the cross sections of reactions (1)-(4) and (8)-(15) in the $E_{c.m.}$ range from 0.06 to 40 eV. The charge transfer channels for $O^+(^2P)$ and $O^+(^2D)$ are found to be much more efficient than that for $O^+(^4S)$, making N_2 an excellent quenching gas for metastable $O^+(^2D,^2P)$ ions in the Earth's ionosphere. Contrary to the observations of earlier studies[24,27], the charge transfer cross sections for $O^+(^2D)$ + N_2 are less than those for $O^+(^2P)$ + N_2. Further experimental investigations and theoretical interpretations are required to resolve this discrepancy. The channels producing NO^+ and N^+ from $O^+(^2P)$ and $O^+(^2D)$ are much less efficient than the charge transfer channel. For the channels producing N^+, we find that the channel of producing N^+ + NO is inaccessible for $O^+(^4S)$ + N_2 but is open for $O^+(^2D,^2P)$ + N_2.

Acknowledgements:

This work was supported by the National Science Foundation Grant No. ATM-9200785 and ATM-9521558.

References

1. P. M. Banks and G. Kockarts, *Aeronomy, Part A* (Academic, New York, 1973), pp. 14, 257.
2. A. Dalgarno and J. L. Fox, in "Unimilocular and Bimolecular Ion-Molecule Reaction Dynamics", edited by C. Y. Ng, T. Baer, and I. Powis, *Wiley Series in Ion Chem. and Phys.* (Wiley, Chichester, 1994), p. 1.
3. E. E. Ferguson, F. C. Fehsenfeld, and D. L. Albritton, in *Gas Phase Ion Chemistry*, edited by M. T. Bowers (Academic, New York, 1979), Vol. 1, p. 45.
4. M. R. Torr and D. G. Torr, *Rev. Geophys. Space Phys.* **20**, 91 (1982).
5. A. Dalgarno and M. B. McElroy, *Planet. space Sci.* **13**, 947 (1965).
6. R. J. W. Henry, *Astrophys. J.* **161**, 1153 (1970).
7. J. L. Kohl, G. P. Lafyatis, H. P. Palenius, and W. H. Parkinson, *Phys. Rev. A* **18**, 571 (1978).

8a D. G. Torr and N. Orsini, *Planet. Space Sci.* **25**, 1171 (1977).

8b. D. G. Torr and N. Orsini, *Geophys. Res. Lett.* **5**, 657 (1978).

9. M. R. Torr and D. G. Torr, *Geophys. Res. Lett.* **7**, 103 (1980).
10. A. Dalgarno, *Adv. At. Mol. Phys.* **15**, 37 (1979).
11. D. R. Bates and H. S. W. Massey, *Proc. R. Soc. London Ser. A* **192**, 1(1947)
12. G. D. Flesh and C.Y. Ng, *J. Chem. Phys.* **92**, 3235 (1990); and references therein.
13. J. D. Burley, K. M. Ervin and P. B. Armentrout, *J. Chem. Phys.* **86**, 1944 (1987).
14. S. G. Lias, J. E. Bartmess, J. F. Liebman, J. L. Holmes, R. D. Levin, and W. G. Mallard,

J. Phys. Chem. Ref. Data, **17** (1988), Suppl. No. 1.

15. H. M. Rosenstock, K. Draxl, B. W. Steiner, and J. T. Herron, *J. Phys. Chem. Ref. Data* **6**, 1 (1977); D. C. Frost and C. A. McDowell, *Proc. Roy. Soc. (London)* **A236**, 278 (1956).
16. K. P. Huber and G. Herzberg, "Molecular Spectra and Molecular Structure: Constants of Diatomic Molecules" (van Nostrand Reinhold, New York, 1979).
17. B. R. Turner, J. A. Rutherford and D. M. J. Compton, *J. Chem. P hys.* **48**, 1602(1968)
18. B. M. Hughes and T. O. Tiernan, *J. Chem. Phys.* **55**, 3419 (1971).
19. B. R. Rowe, D. W. Fahey, F. G. Fehsenfeld and D. L. Albritton, *J. Chem. Phys.* **73**, 194(1980)
20. R. Johnsen and M. A. Biondi, *J. Chem. Phys.* **73**, 190(1980)
21. R. Johnsen and M. A. Biondi, *Geophys. Res. Lett.* **7**, 401(1980)
22. J. A. Rutherford and D. A. Vroom, *J. Chem. Phys.* **55**, 5622(1971)
23. X. Li, Y.-L. Huang, G. D. Flesch and C.Y. Ng, *Rev. Sci. Instrum.* **66**, 2871(1995)
24. G. D. Flesch and C.Y. Ng, *J. Geophys. Res.* **96**, 21407 (1991).
25. G. Bischof and F. Linder, *Z. Phys. D.* **1**, 303(1986)
26. D. Gerlich, *State-Selected and State-to-State Ion Molecule Reaction Dynamics I: Experiment*, edited by C.Y. Ng and M. Baer, pp.1-176, John Wiley, New York(1991); M. Scherbarth, Diplom thesis, University of Freiburg, 1988.
27. M. Lavollée and M. Henri, *J. Phys. B: At. Mol. Opt. Phys.* **22**, 2019 (1989).
28. X. Li, Y.-L. Huang, G. D. Flesch and C.Y. Ng, *Rev. Sci. Instrum.* **65**, 3724 (1994).

29. X. Li, Y.-L. Huang, G. d. Flesch, and C. Y. Ng, *J. Chem. Phys.* submitted.

30. G. D. Flesch, S. Nourbakhsh, and C. Y. Ng, *J. Chem. Phys.* **92**, 3590 (1990).

31. G. D. Flesch and C. Y. Ng, *J. Chem. Phys.* **92**, 3235 (1990).

32. G. D. Flesch and C. Y. Ng, *J. Chem. Phys.* **89**, 3381 (1988).

33. G. D. Flesch and C. Y. Ng, *J. Chem. Phys.* **92**, 2876 (1990).

34. N. R. Daly, *Rev. Sci. Instrum.* **31**, 264 (1960).

35. G. O. Brink, *Rev. Sci. Instrum.* **37**, 857, 1626 (1966).

36. These values correspond to Ne^+ formed in the $^2P_{1/2}$ spin-orbit excited state.

37. G. D. Flesch, S. Nourbakhsh, and C. Y. Ng, *J. Chem. Phys.* **95**, 3381 (1991).

38. G. D. Flesch, S. Nourbakhsh, and C. Y. Ng, *J. Chem. Phys.* **92**, 3590 (1990).

39. J. Glosik, A. B. Rakshit, N. D. Twiddy, N. G. Adams and D. Smith, *J. Phys. B* **11**, 3365 (1978)

40. D. G. Torr, *Rev. Geophys. Space Phys.* **17**, 510(1979)

41. G. Gioumousis and D. P. Stevenson, *J. Chem. Phys.* **29**, 294(1958)

42. M. Oppenheimer, A. Dalgarno and H. C. Brinton *J. Geophys. Res.* **81**, 3762(1976)

43. We note that the labels for the NO^- and N^+ cross sections shown in Figs. 1(a) and 1(b) of Ref. 24 should be switched.

CHAPTER IV

ABSOLUTE STATE-SELECTED TOTAL CROSS SECTIONS FOR THE ION-MOLECULE REACTIONS $O^+(^4S,^2D,^2P)$ + H_2 (D_2)

A paper submitted to the Journal of Chemical Physics

X. Li, Y.-L. Huang, G. D. Flesch and C. Y. Ng

Abstract:

Absolute total cross sections for the state-selected reactions of $O^+(^4S,^2D,^2P)+H_2$ (D_2) have been measured in the center-of-mass collision energy ($E_{c.m.}$) range of 0.02-12 eV. The cross sections for OH^+ (OD^+) from $O^+(^2D)$ + H_2 (D_2) are slightly higher than those from $O^+(^4S)+H_2$ (D_2), whereas the OH^+ (OD^+) cross sections from $O^+(^2P)+H_2$ (D_2) are $\approx$40% lower than those from $O^+(^4S)+H_2(D_2)$ and $O^+(^2D)+H_2(D_2)$. At $E_{c.m.}<0.5$ eV, the total cross sections for OH^+ (OD^+) from $O^+(^4S)$ + H_2 (D_2) and $O^+(^2D)+H_2$ (D_2) are in accord with those predicted by the Langevin-Gioumousis-Stevenson model. Significantly higher cross sections are observed for $H^+(D^+)$ and H_2^+ (D_2^+) from $O^+(^2D)+H_2(D_2)$ and $O^+(^2P)$ $+H_2(D_2)$, as compared to those from $O^+(^4S)$ + $H_2(D_2)$. The exothermic nature of the $O^+(^2D,^2P)$ + H_2 (D_2) charge transfer collisions accounts for the high cross sections observed for H_2^+

(D_2^+). While the H^+ (D^+) ions observed in the $O^+(^4S)$ + H_2 (D_2) reaction are identified with the H^+ (D^+) + O + H channel, the H^+ (D^+) ions from the reactions involving $O^+(^2D)$ and $O^+(^2P)$ are associated mostly with the H^+ (D^+) + OH (OD) channel, the formation of which obeys the spin-conservation rule. The comparison of the sum (σ_T) of cross sections for OH^+ (OD^+), H_2^+ (D_2^+), and H^+ (D^+) from $O^+(^4S)$ + H_2 (D_2) to those from $O^+(^2D)$ + H_2 (D_2) and $O^+(^2P)$ + H_2 (D_2) shows that the σ_T's for $O^+(^4S)$ + H_2 (D_2), $O^+(^2D)$ + H_2 (D_2), and $O^+(^2P)$ + H_2 (D_2) at $E_{c.m.} < 0.5$ eV are comparable. At $E_{c.m.} > 0.5$ eV, the σ_T's for $O^+(^2P)$ + H_2 (D_2) are greater than those for $O^+(^2D)$ + H_2 (D_2), which in turn are greater than those for $O^+(^4S)$ + H_2 (D_2). This observation is attributed to the increase in the number of accessible product channels for reactions involving the excited $O^+(^2D)$ and $O^+(^2P)$ reactant ions.

I. INTRODUCTION

In addition to producing the ground $O^+(^4S)$ state ions, excited $O^+(^2D)$ and $O^+(^2P)$ ions are also formed in abundance by solar vacuum ultraviolet (VUV) photoionization, dissociative electron ionization, and charge exchange processes in atmospheric and astrophysical plasmas.[1,2] For example, the branching ratios for $O^+(^4S)$:$O^+(^2D)$:$O^+(^2P)$ formed by VUV photoionization of atomic oxygen in the ionosphere[5] are estimated to be 0.43:0.29:0.28.[3-6] Since the $O^+(^2D)$ and $O^+(^2P)$ ions are metastable with relatively long lifetimes of 3.6 hours and 4.57 seconds, respectively, the ion-molecule reactions involving these excited atomic ions are important for modeling the ion chemistry of planetary ionospheres.[7-10]

The ion-molecule reaction O^+ + H_2 is relevant to the study of H_2-rich interstellar clouds where product OH^+ ions further react with H_2 to yield H_2O^+ and H_3O^+ molecular

ions.[1,11-13] Due to their simplicity, the $O^+ + H_2$ (D_2) reactions are model systems for detailed studies of ion-molecule reaction dynamics and have been the subject of many experimental[14-25] and theoretical investigations.[26-38] These studies have provided considerable insight into the dynamics and potential energy surfaces of the $[O + H_2]^+$ reaction system.[26-33,36]

Previous experimental investigations have been focused mostly on the reactions of $O^+(^4S) + H_2$ (D_2).[14-25] The possible product channels and their energetics[39] are summarized below.

$O^+(^4S) + H_2$	$\rightarrow OH^+(X^3\Sigma^-) + H$	$\Delta H^\circ = -0.54$ eV	(1a)
	$\rightarrow OH^+(^1\Delta) + H$	$\Delta H^\circ = 1.66$ eV	(1b)
	$\rightarrow OH^+(A^3\Pi) + H$	$\Delta H^\circ = 2.99$ eV	(1c)
	$\rightarrow H_2^+ + O$	$\Delta H^\circ = 1.80$ eV	(2)
	$\rightarrow H^+ + O + H$	$\Delta H^\circ = 4.48$ eV	(3)
	$\rightarrow H^+ + OH(X^2\Pi)$	$\Delta H^\circ = 0.06$ eV	(4)
$O^+(^4S) + D_2$	$\rightarrow OD^+(X^3\Sigma^-) + D$	$\Delta H^\circ = -0.51$ eV	(5a)
	$\rightarrow OD^+(^1\Delta) + D$	$\Delta H^\circ = 1.69$ eV	(5b)
	$\rightarrow OD^+(A^3\Pi) + D$	$\Delta H^\circ = 3.02$ eV	(5c)
	$\rightarrow D_2^+ + O$	$\Delta H^\circ = 1.83$ eV	(6)
	$\rightarrow D^+ + O + D$	$\Delta H^\circ = 4.51$ eV	(7)
	$\rightarrow D^+ + OD(X^2\Pi)$	$\Delta H^\circ = 0.09$ eV	(8)

Unless specified, the atomic and molecular neutrals and ions involved in reactions (1)-(8) are assumed to be in their ground states. The previous theoretical studies suggest that the formation of $OH^+(^3\Sigma^-)$ + H from $O^+(^4S)$ + H_2 [reaction (1a)] proceed via a nearly collinear $O^+\cdots$H-H geometry on the ground attractive potential energy surface.[14,15,27-35,38] On the basis of the ion-neutral beam[14] and ion-gas cell[15] scattering studies, a spectator stripping mechanism[40] is proposed for the formation of OH^+ from reaction (1) in the center-of-mass (c.m.) kinetic energy ($E_{c.m.}$) range of 0.8-8.0 eV. The scattering[14,15] and luminescence[15] experiments show that $OH^+(^1\Delta)$ [channel (1b)] and $OH^+(A^3\Pi)$ [channel (1c)] are also formed when sufficient $E_{c.m.}$ is available.

Detailed absolute total cross sections for OH^+, H_2^+, and H^+ formed in reactions (1a-1c), (2), and (3), respectively, have been reported.[19,20,23] It has been shown that at $E_{c.m.} < 0.5$ eV, experimental rate constants[16-19] and total cross sections[19] for OH^+ formed in reaction (1a) are in excellent agreement with predictions based on the Langevin-Gioumousis-Stevenson (LGS) model[41]. This model gives a general estimate of the magnitude and energy dependence of the total absolute cross section for an exothermic ion-molecule reaction. At $E_{c.m.} > 0.5$ eV, the cross sections deviate from the LGS predictions, partly attributed to angular momentum constraints.[19,37] Furthermore, previous experiments indicate that OH^+ formed at high $E_{c.m.}$ may contain significant internal energies, resulting in spontaneous fragmentation to yield O^- + H and/or H^+ + O [reaction (3)]. Reaction (4), which is nearly thermal neutral, was found to be unimportant in the experimental study of Flesch and Ng.[23] For $O^+(^4S)$ + D_2, the absolute cross sections for the OD^+ formation from reactions (5a-5c) have also been

reported.[19] However, the formation of D_2^+ and D^+ from reactions (6)-(8) has not been examined previously.

Since the $O^+(^2D)$ and $O^+(^2P)$ excited states are 3.32 and 5.02 eV, respectively, higher than the $O^+(^4S)$ ground state, we expect that the reactivities for these excited states are quite different from that of the ground state.[42] However, due to the difficulty in preparing state-selected $O^+(^2D)$ and $O^+(^2P)$ ion beams, the absolute total cross sections or rate constants for the reactions of $O^+(^2D) + H_2$ (D_2) and $O^+(^2P) + H_2$ (D_2) have not been examined in detail. We note that absolute cross sections have been reported[21,22,24,25] for the $O^+ + H_2$ charge transfer collisions at high kinetic energies using a mixture of $O^+(^2D)$ and $O^+(^2P)$ reactant ions.

By using dissociative charge transfer (DCT) reactions

$$Ne^+ + O_2 \rightarrow Ne + O^+(^4S,^2D) + O \qquad (9)$$

$$He^+ + O_2 \rightarrow He + O^+(^4S,^2D,^2P) + O \qquad (10)$$

and octopole ion trap (OIT) techniques, we have recently succeeded in preparing state-specific $O^+(^2D)$ and $O^+(^2P)$ ion beams with sufficiently high intensities for scattering experiments.[43] In order to improve the kinetic energy resolution for $O^+(^2D)$ and $O^+(^2P)$ ion beams prepared by the DCT-OIT method, we have also developed a differential retarding potential (DRP) scheme[44]. Applying the DCT-OIT and DRP methods, we have obtained absolute cross sections for a series of atmospheric ion-molecule reactions involving $O^+(^2D)$ and $O^+(^2P)$. Here, we report the results for the $O^+(^2D) + H_2$ (D_2) and $O^+(^2P) + H_2$ (D_2) reactions. Cross

sections for these reactions are compared to those for $O^+(^4S)$ + H_2 (D_2).[19,23]

II. EXPERIMENT

The experimental arrangement and procedures for cross section measurements using the triple-quadruple double-octopole (TQDO) apparatus (Fig. 1) have been described in detail[45-48]. The TQDO apparatus essentially consists of, in sequential order, a VUV photoionization ion source or an electron impact ionization ion source (1), a reactant quadruple mass spectrometer (QMS) (5), a lower radio frequency (RF) octopole ion guide reaction gas cell (RFOIGGC) [(6) + (7)], a middle QMS (10), an upper RFOIGGC [(11) + (14)], a product QMS (15), and a Daly-type scintillation ion detector[49] [(17) + (19) + (20)]. The electron impact ionization ion source used here is of the Brink design[50] and has been added to the TQDO apparatus recently. The TQDO apparatus is partitioned into five chambers which are separately evacuated by liquid nitrogen- or freon-trapped diffusion pumps. The differential pumping arrangement is important for the reactant ion preparation scheme and the cross section measurement experiments described here.

Here $O^+(^4S)$ reactant ions are produced by dissociative photoionization of O_2 at 640 Å and a wavelength resolution of 2.5 Å (FWHM). When the VUV photon source is used to produce $O^+(^4S)$ ions, the lower gas cell is empty and the lower octopole and reactant QMS just serve as ion passing devices. Absolute cross section measurements are made using the upper octople reaction gas cell.[23]

If $O^+(^2D)$ and $O^+(^2P)$ are needed, these ions are produced by DCT processes (9) and (10), respectively. Basically, rare gas ions (Ne^+, He^+) are generated in the ionization region

Figure 1 Schematic diagram of the TQDO apparatus. (1) electron impact ionization ion source, (2) atomic or molecular nozzle beam, (3) to freon-trapped 6" diffusion pump (DP), (4) to liquid-nitrogen (LN_2)-trapped 6" DP, (5) reactant QMS, (6) lower RF octopole ion guide, (7) lower RFOIGGC, (8) to LN_2-trapped 6" DP, (9) the lower RF octopole ion guide chamber, (10) middle QMS, (11) upper RF octopole ion guide, (12) to LN_2-trapped 4" DP, (13) upper RF octopole ion guide chamber, (14) upper RFOIGGC, (15) product QMS, (16) detector chamber, (17) plastic scintillator window, (18) to LN_2-trapped 2" DP, (19) photomultiplier tube, (20) aluminum ion target.

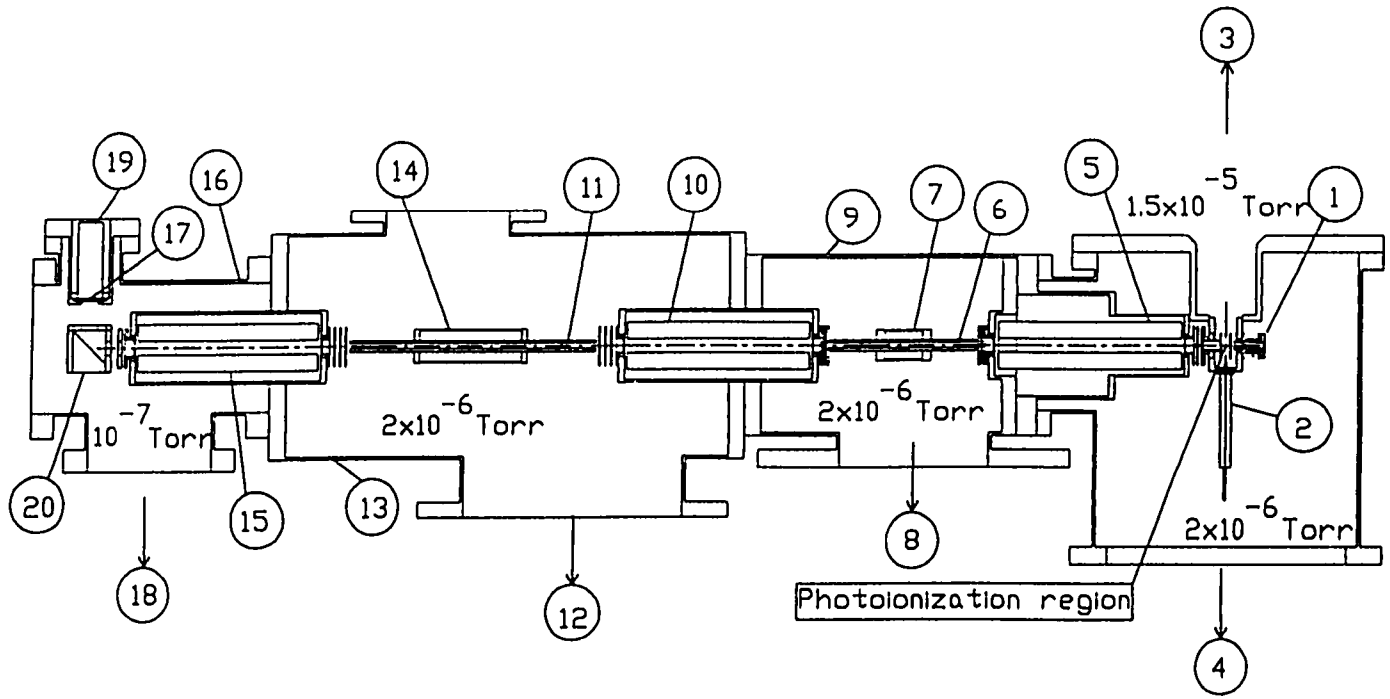
3
19
16
14
11
10
9
7
6
5
1.5x10 -5 Torr
1
17
2x10 -6 Torr
2x10 -6 Torr
10 -7 Torr
2
20
15
13
8
2x10 -6 Torr
18
12
Photoionization region
4

by electron impact. These ions are then extracted from the ionization region and mass-selected by the reactant QMS. The DCT reactions (9) and (10) take place in the lower gas cell, into which oxygen gas has been introduced. In reaction (10), which is exothermic, a mixture of $O^+(^4S)$, $O^+(^2D)$, and $O^+(^2P)$ are produced with well resolved kinetic energy distributions.[51,52] At $E_{c.m.}$ = 1-2 eV, $O^+(^2P)$ ions have lower kinetic energies than those for $O^+(^4S)$ and $O^+(^2D)$, and are found to be the dominant product channel with a branching ratio of 50-60%. The idea of the state-selection method is to lower the trapping voltage of the lower RF octopole so that energetic $O^+(^4S)$ and $O^+(^2D)$ ions escape from the octopole trap and slow $O^+(^2P)$ ion remain trapped. This is essentially is an $O^+(^2P)$ enrichment scheme. Under the present experimental conditions which maximize the transmission fraction for $O^+(^2P)$, we estimate that the $O^+(^2P)$ ion beam has a purity of 89%, with the remaining fraction about 5% each for $O^+(^4S)$ and $O^+(^2D)$. The formation of $O^+(^2D)$ and $O^+(^2P)$ from reaction (9) is endothermic by 0.48 (0.38)[53] and 2.18 (2.10)[53] eV, respectively. Thus, the formation of $O^+(^2P)$ can be avoid at $E_{c.m.} < 2.1$ eV. The $E_{c.m.}$ dependence of the cross section for reaction (9) reveals a sharp onset at the thermochemical threshold for the formation of $O^+(^2D)$, indicating that the formation of $O^+(^2D)$ is efficient,[54] in accordance with the DCT mechanism.[47,55,56] By choosing $E_{c.m.}$ = 0.73 eV, and by lowering the effective trapping potential of the RF octopole ion trap to lose the $O^+(^4S)$ ions, we estimate that the $O^+(^2D)$ ion beam used in the present experiment has a purity ≥90%.

The state-selected $O^+(^2D)$ [$O^+(^2P)$] ions thus formed are mass-selected by the middle QMS and transmitted into the upper gas cell where the reactions between $O^+(^2D)$ [$O^+(^2P)$] and

$H_2(D_2)$ occur. The $H_2(D_2)$ gas cell pressures used in this experiment are $\leq 2\times10^{-4}$ Torr. The product ions are detected using the upper QMS and the Daly-type scintillation ion detector. At each $E_{c.m.}$, the product ion collection efficiency is maximized by carefully optimizing the transmission of the ion lenses, product QMS, and the octopole ion guide.

The uncertainties for absolute cross sections reported here are estimated to be $\leq$ 25%. However, the uncertainties for relative cross sections are believed to be smaller than 10%.

III. RESULTS AND DISCUSSION

The possible channels and their energetics resulting from the reactions $O^+(^2D,^2P)$ + H_2 and $O^+(^2D,^2P)$ + D_2^+ are:

$$O^+(^2D) + H_2 \rightarrow OH^+(X^3\Sigma^-) + H \qquad \Delta H° = -3.84 \text{ eV} \qquad (11a)$$

$$\rightarrow OH^+(^1\Delta) + H \qquad \Delta H° = -1.66 \text{ eV} \qquad (11b)$$

$$\rightarrow OH^+(A^3\Pi) + H \qquad \Delta H° = -1.01 \text{ eV} \qquad (11c)$$

$$\rightarrow H_2^+ + O \qquad \Delta H° = -1.51 \text{ eV} \qquad (12)$$

$$\rightarrow H^+ + O + H \qquad \Delta H° = 1.18 \text{ eV} \qquad (13)$$

$$\rightarrow H^+ + OH(X^2\Pi) \qquad \Delta H° = -1.1 \text{ eV} \qquad (14a)$$

$$\rightarrow H^+ + OH(A^2\Sigma^+) \qquad \Delta H° = 2.95 \text{ eV} \qquad (14b)$$

$$O^+(^2P) + H_2 \rightarrow OH^+(X^3\Sigma^-) + H \qquad \Delta H° = -5.38 \text{ eV} \qquad (15a)$$

$$\rightarrow OH^+(^1\Delta) + H \qquad \Delta H° = -3.17 \text{ eV} \qquad (15b)$$

$$\rightarrow OH^+(A^3\Pi) + H \qquad \Delta H° = -2.55 \text{ eV} \qquad (15c)$$

$$\rightarrow H_2^+ + O \qquad \Delta H° = -3.05 \text{ eV} \qquad (16)$$

$$\rightarrow H^+ + O + H \qquad \Delta H° = -0.36 \text{ eV} \qquad (17)$$

$$\rightarrow OH(X^2\Pi) + H^+ \qquad \Delta H^\circ = -2.7 \text{ eV} \qquad (18a)$$

$$\rightarrow OH(A^2\Sigma^+) + H^+ \qquad \Delta H^\circ = 1.35 \text{ eV} \qquad (18b)$$

$$O^+(^2D) + D_2 \rightarrow OD^+(X^3\Sigma^-) + D \qquad \Delta H^\circ = -3.81 \text{ eV} \qquad (19a)$$

$$\rightarrow OD^+(^1\Delta) + D \qquad \Delta H^\circ = -1.63 \text{ eV} \qquad (19b)$$

$$\rightarrow OD^+(A^3\Pi) + D \qquad \Delta H^\circ = -0.98 \text{ eV} \qquad (19c)$$

$$\rightarrow D_2^+ + O \qquad \Delta H^\circ = -1.48 \text{ eV} \qquad (20)$$

$$\rightarrow D^+ + O + D \qquad \Delta H^\circ = 1.21 \text{ eV} \qquad (21)$$

$$\rightarrow D^+ + OD(X^2\Pi) \qquad \Delta H^\circ = -1.08 \text{ eV} \qquad (22a)$$

$$\rightarrow D^+ + OD(A^2\Sigma^+) \qquad \Delta H^\circ = 2.98 \text{ eV} \qquad (22b)$$

$$O^+(^2P) + D_2 \rightarrow OD^+(X^3\Sigma^-) + D \qquad \Delta H^\circ = -5.35 \text{ eV} \qquad (23a)$$

$$\rightarrow OD^+(^1\Delta) + D \qquad \Delta H^\circ = -3.14 \text{ eV} \qquad (23b)$$

$$\rightarrow OD^+(A^3\Pi) + D \qquad \Delta H^\circ = -2.52 \text{ eV} \qquad (23c)$$

$$\rightarrow D_2^+ + O \qquad \Delta H^\circ = -3.02 \text{ eV} \qquad (24)$$

$$\rightarrow D^+ + O + D \qquad \Delta H^\circ = -0.33 \text{ eV} \qquad (25)$$

$$\rightarrow D^+ + OD(X^2\Pi) \qquad \Delta H^\circ = -2.67 \text{ eV} \qquad (26a)$$

$$\rightarrow D^+ + OD(A^2\Sigma^+) \qquad \Delta H^\circ = 1.38 \text{ eV} \qquad (26b)$$

In the calculations of the ΔH° values for these reactions, the neutrals and ions are assumed to be in their ground states unless specified otherwise.[39,42,57] Since the previous experiments suggest that the $OH^+(^1\Delta)$, $OH^+(A^3\Pi)$, and $OH(A^2\Sigma^+)$ states are populated in the $E_{c.m.}$ range of the present experiment,[14,15] we have also included these excited product channels. We note that an excited $OH^+(^1\Sigma^+)$ state, which lies $\approx$3.6 eV above the ground $OH^+(X^3\Sigma^-)$ state, may

also be populated.[57] However, the 2nd excited OH($B^2\Sigma^+$) state, known to be 8.65 eV above the ground OH($X^2\Pi$) state,[57] is not likely to be involved in this experiment. Furthermore, since the excited O(^1D) state is 1.97 eV above the ground O(^3P) state, excited O(^1D) as well as ground O(^3P) atoms may also be formed in the charge transfer collisions of $O^+(^2D) + H_2$ (D_2) and $O^+(^2P) + H_2$ (D_2).

A. OH^+ formed by the reactions of $O^+(^4S,^2D,^2P) + H_2$

The absolute cross sections for OH^+ from $O^+(^2D) + H_2$ [reactions (11a-11c)] and $O^+(^2P) + H_2$ [reactions (15a-15c)] in the $E_{c.m.}$ range of 0.02-7.00 eV are depicted in Fig. 2. As a calibration of the absolute cross sections for reactions (11a-11c) and (15a-15c), we have also re-measured the absolute cross sections for OH^+ from reaction (1a) in the $E_{c.m.}$ range of 0.02-0.4 eV. These absolute cross sections are found to be in excellent agreement with those reported in previous studies.[19] The LGS cross sections [$\sigma_L(E_{c.m.})$] shown by the dashed line in Fig. 2 are calculated according to the equation,[41]

$$\sigma_L(E_{c.m.}) = \pi e(2\alpha/E_{c.m.})^{1/2}, \tag{27}$$

where e is the charge of the electron and α (= 0.790 Å^3)[58] is the polarizability of the H_2 molecule. In accord with the observations of Burley et al.,[19] the cross sections for reaction (1a) at $E_{c.m.} < 0.4$ eV agree with the LGS predictions.

As shown in Fig. 2, the absolute cross sections for OH^+ formed from $O^+(^2D) + H_2$ is slightly higher than those from $O^+(^4S) + H_2$. However, taking into account the experimental uncertainties, the cross sections for OH^+ from $O^+(^2D) + H_2$ at $E_{c.m.} < 0.5$ eV are considered to be in agreement with the σ_L values. The $E_{c.m.}$ dependence of the cross

Figure 2 The cross sections for OH^+ from $O^+(^4S) + H_2$ (solid circles), $O^+(^2D) + H_2$ (solid triangles), and $O^+(^2P) + H_2$ (solid squares) in the Ec.m. range of 0.02-7 eV. The LGS cross sections calculated using the polarizability $\alpha(H_2) = 0.790$ Å^3 are given by the dashed line.

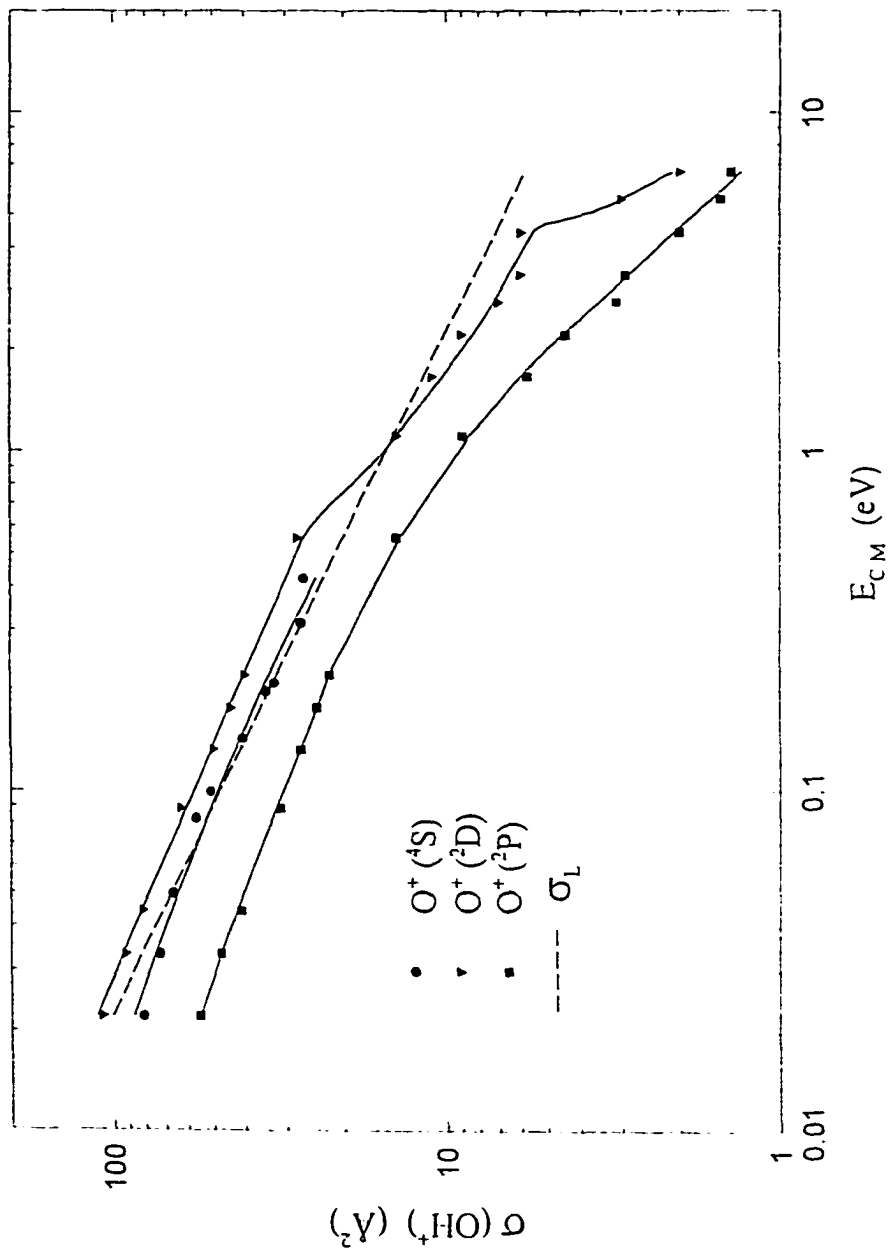
σ (OH+) (Å2)
100
10
1
0.01
0.1
1
10
E CM (eV)
O+ (4S)
O+ (2D)
O+ (2P)
σL

section for reactions (11a-11c) is similar to that for reactions (1a-1c) observed previously, with breaks in slope at $E_{c.m.}$ ≈ 0.5 and 5 eV. Since the dissociation energies for OH^+ to $O + H^+$ and $O^+ + H$ are 4.99 and 5.01 eV,[39] respectively, the decline in cross sections at $E_{c.m.} > 5$ eV can be partly attributed to the further dissociation of internally excited OH^+. We note that the dissociation of OH^+ corresponds to the formation of $O^+ + H + H$, a product channel which cannot be detected in the present experiment because the mass for the product O^+ ion is the same as the reactant ion. The excited $OH^+(^1\Delta)$ and $OH^+(A^3\Pi)$ states are 2.20 and 2.85 eV above the $OH^+(X^3\Sigma^-)$ state.[42] Thus, the formation of $OH^+(^1\Delta)$ and $OH^+(A^3\Pi)$ from $O^+(^2D) + H_2$ [reactions (11b) and (11c)] is energetically allowed, with exothermicities of 1.66 and 1.01 eV, respectively. The correlation diagram constructed for a collinear $O^+\cdots$H-H reaction configuration indicates that the $O^+(^2D) + H_2$ reactant state correlates to the $OH^+(^1\Delta) + H$ product state.[4] However, taking into account higher order interactions, such as spin-orbit coupling, the $OH^+(X^3\Sigma^-, A^3\Pi)$ should also be accessible to the reactants. The excited product channels $OH^+(^1\Delta) + H$ and $OH^+(A^3\Pi) + H$, available to the reaction of $O^+(^2D) + H_2$ at low collision energies, may account for the slightly higher cross sections for OH^+ from $O^+(^2D) + H_2$ at $E_{c.m.} < 0.5$ eV compared to those from $O^+(^4S) + H_2$.

At corresponding $E_{c.m.}$'s, the absolute cross sections for OH^+ formed from $O^+(^2P) + H_2$ are more than 40% lower than those from $O^+(^4S) + H_2$. Considering that reactions (15a), (15b), and (15b) are all exothermic, it is most likely that the collisions of $O^+(^2P)$ and H_2 produce OH^+ in the excited $OH^+(^1\Delta)$ and $OH^+(A^3\Pi)$ states as well as the ground $OH^+(X^3\Sigma^-)$ state. Since the exothermicity of 5.38 eV for reaction (15a) is higher than the respective

dissociation energies of 4.99 and 5.01 eV for $OH^+(X^3\Sigma^-)$ into $H^+ + O$ and $O^+ + H$, the lower cross sections for OH^+ from $O^+(^2P) + H_2$ is thus rationalized by the further dissociation of highly excited OH^+. As shown below, the relatively high cross sections observed for the formation of H^+ are consistent in part with this rationalization.

B. H_2^+ and H^+ formed by the reactions of $O^+(^4S,^2D,^2P) + H_2$

Figure 3 depicts the absolute cross sections of H_2^+ and H^+ from $O^+(^2D) + H_2$ and $O^+(^2P) + H_2$ in the $E_{c.m.}$ range of 0.02-7 eV. The absolute cross sections for H_2^+ and H^+ from $O^+(^4S) + H_2$ obtained previously in our laboratory are also included in Fig. 3.[23] The appearance energies for H_2^+ and H^+ formed in the $O(^4S) + H_2$ reaction are consistent with the thermochemical thresholds for the formation of $H_2^+ + O$ [reaction (2)] and $H^+ + O + H$ [reaction (3)], respectively. The fact that negligible H^+ ions are observed below $E_{c.m.} < 4.5$ eV indicates that reaction (4) is not important. This observation is rationalized by the fact that reaction (4) violates the spin-conservation rule.[19,23]

The thermochemical threshold for the formation of $H^+ + O + H$ from $O^+(^2D) + H_2$ is 1.18 eV. As shown in Fig. 3, the cross sections for H^+ from $O^+(^2D) + H_2$ are in the range of ≈0.5-1.5 Å^2 at $E_{c.m.}$ = 0.02-7 eV, which are nearly an order of magnitude greater that those for reaction (3) in the $E_{c.m.}$ range of 4-7 eV. This indicates that the H^+ ions observed are mostly due to reaction (14a), which is exothermic by 1.1 eV. The cross section for H^+ from $O^+(^2P) + H_2$ decreases from 8 Å^2 at $E_{c.m.}$ = 0.04 eV to 2 Å^2 at $E_{c.m.}$ ≈7 eV. These cross sections are 2-8 fold greater than those for reaction (14a). Since the $H^+ + O + H$ and $H^+ + OH$ channels from $O^+(^2P) + H_2$ are exothermic by 0.36 and 2.7 eV, respectively, both

Figure 3 Cross sections for H^+ and H_2^+ from the reactions of $O^+(^4S) + H_2$, $O^+(^2D) + H_2$, and $O^+(^2P) + H_2$ in the $E_{c.m.}$ range of 0.02-7 eV. Note that the cross sections for H^+ and H_2^+ from $O^+(^4S) + H_2$ have been multiplied by 50 and 10, respectively.

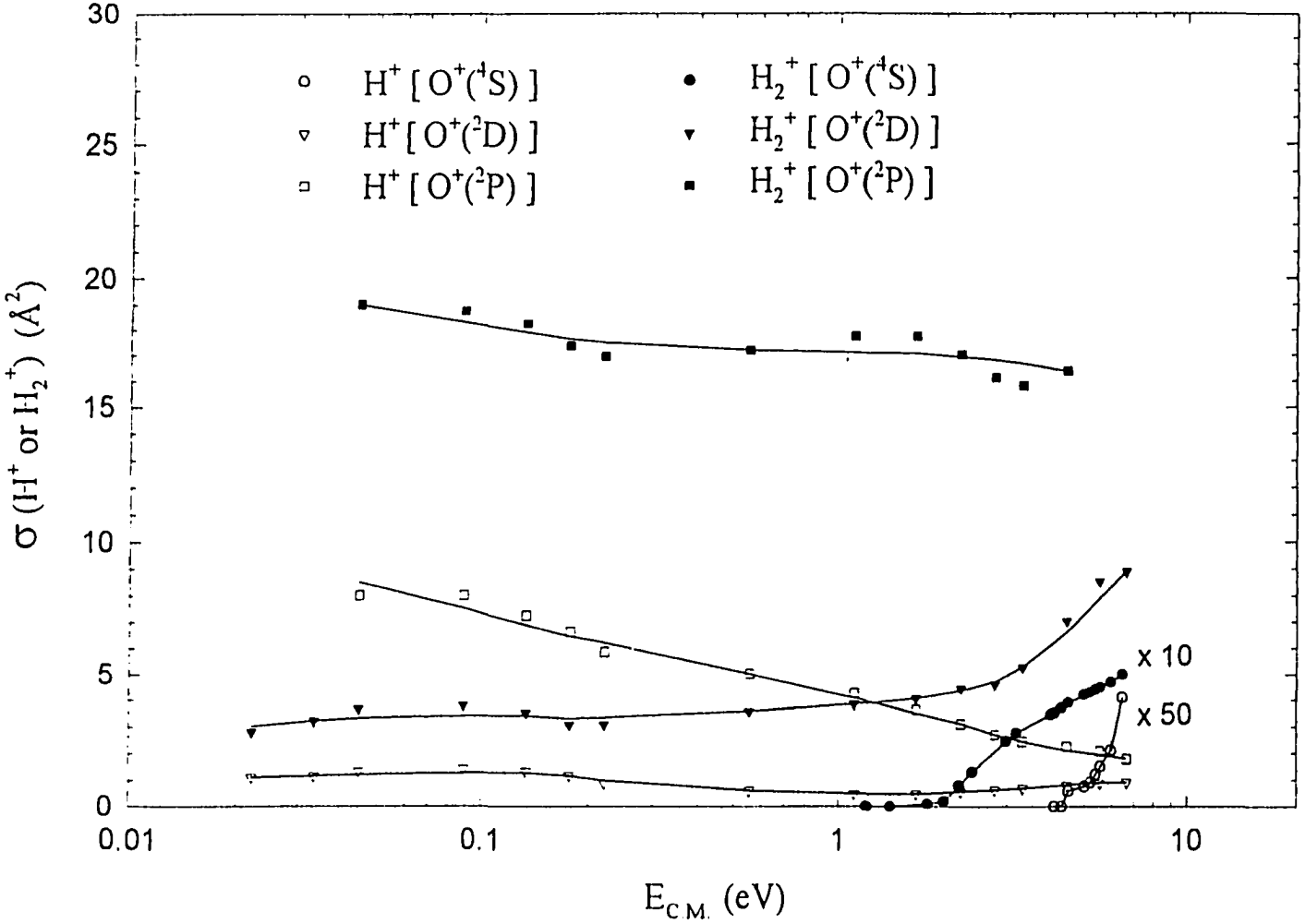
30
25
20
15
10
5
0
0.01
0.1
1
10
σ (H+ or H2+) (Å2)
E c.m. (eV)
H+ [O+(4S)]
H+ [O+(2D)]
H+ [O+(2P)]
H2+ [O+(4S)]
H2+ [O+(2D)]
H2+ [O+(2P)]
x 10
x 50

reactions (17) and (18a) may contribute to the H^+ ions observed here. We note that both reactions (14a) and (18a) obey the spin-conservation rule. The formation of $OH(X^2\Pi) + H^+$ by the reaction of $O^+(^2D) + H_2$ is also supported by the correlation diagram.[14,15] The previous luminescence experiment[15] suggests that excited $OH(A^2\Sigma^+)$ $[OD(A^2\Sigma^+)]$ is also formed in the reaction of $O^+(^2D,^2P) + H_2$ (D_2).

The cross sections for H_2^+ from $O^+(^2D) + H_2$ and $O^+(^2P) + H_2$ are significantly higher than the corresponding H^+ cross sections. The cross section for H_2^+ from $O^+(^2D) + H_2$ increases from ≈3 Å^2 at $E_{c.m.}$ ≈ 0.02 eV to 9 Å^2 at $E_{c.m.}$ ≈ 7 eV. The H_2^+ cross sections for $O^+(^2P) + H_2$ in the $E_{c.m.}$ range of 0.04-5 eV are nearly constant with values of 16-19 Å^2. The relatively large charge transfer cross sections observed are rationalized by the fact that reactions (12) and (16) are exothermic. As pointed out above, the formation of $O(^1D)$, together with H_2^+, from $O^+(^2D) + H_2$ and $O^+(^2P) + H_2$ are possible. Previous studies at higher $E_{c.m.}$ using a mixture of $O^+(^2D)$ and $O^+(^2P)$ reactant ions report charge transfer cross sections of ≈10 Å^2.[21,24,25] Xu *et al.*[21] propose that the near energy resonance processes,

$$O^+(^2D) + H_2 \rightarrow H_2^+(X^2\Sigma_g^+, v'=7) + O(^3P) \qquad \Delta H^\circ = 0.071 \text{ eV} \qquad (28)$$

$$O^+(^2P) + H_2 \rightarrow H_2^+(X^2\Sigma_g^+, v'=5) + O(^1D), \qquad \Delta H^\circ = -0.039 \text{ eV} \qquad (29)$$

which have energy defects of 0.071 eV and -0.039 eV, respectively, may account for the high charge transfer cross sections. In both reactions (28) and (29), the H_2^+ products are vibrationally excited. The formation of vibrationally excited H_2^+ in these charge transfer reactions has also been observed by Rowe *et al.*[59]

Figure 4 The cross sections for OD^+ from the reactions of $O^+(^4S) + D_2$ (solid circles), $O^+(^2D) + D_2$ (solid triangles), and $O^+(^2P) + D_2$ (solid squares) in the $E_{c.m.}$ range of 0.02-12 eV. The LGS cross sections calculated using the polarizibility $\alpha(D_2) = 0.775$ Å^3 are given by the dashed line.

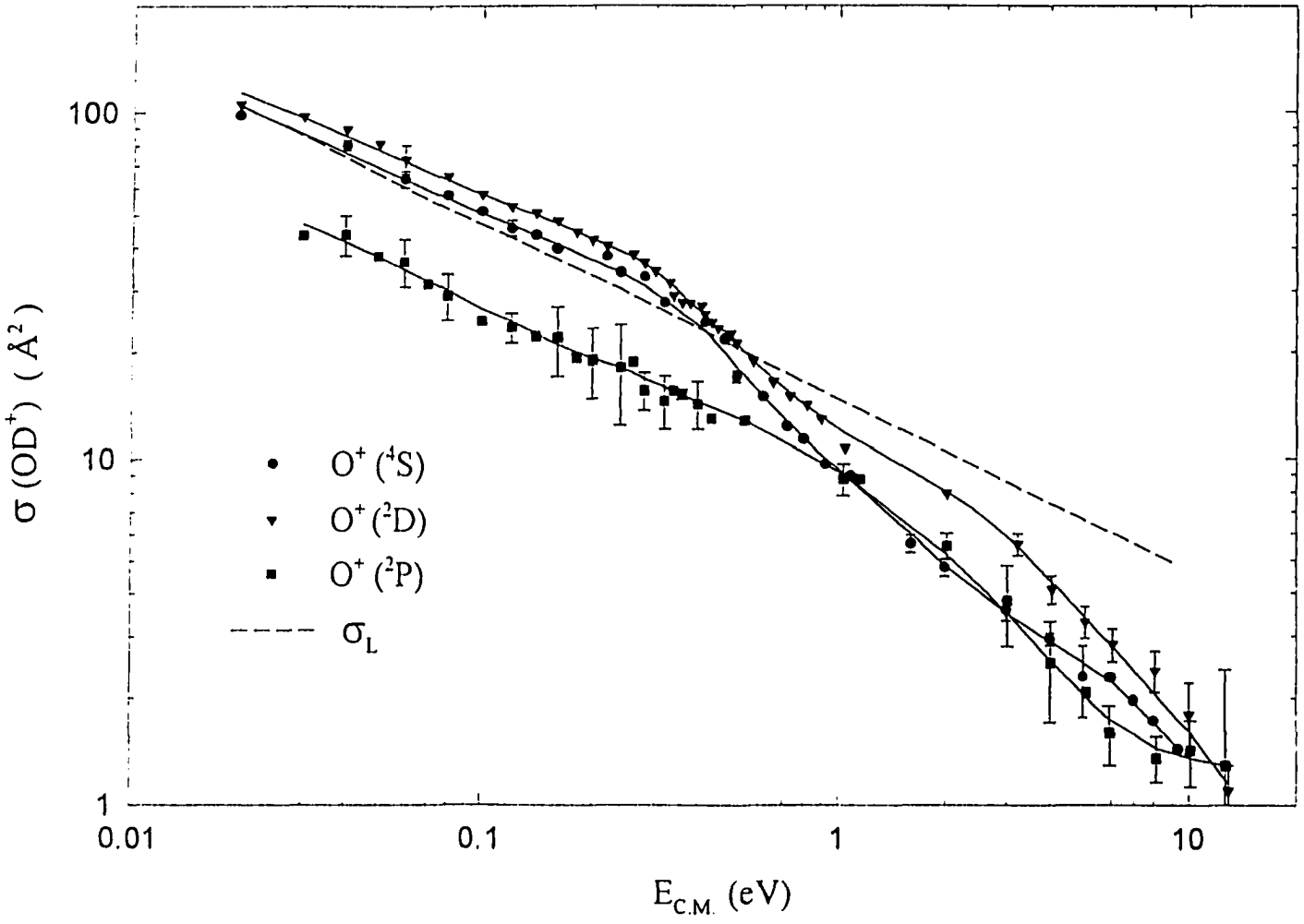
100
10
1
0.01
0.1
1
10
σ (OD+) (Å2)
E C.M. (eV)
O+ (4S)
O+ (2D)
O+ (2P)
σL

C. OD^+ formed by the reactions of $O^+(^4S,^2D,^2P) + D_2$

The absolute cross sections for OD^+ from reactions (5a-5c), (19a-19c), and (23a-23c) in the $E_{c.m.}$ range of 0.01-10 eV are depicted in Fig. 4, together with the dashed line calculated by the LGS model using averaged polarizability[58] of $\alpha(D_2) = 0.775$ Å^3. The cross sections for OD^+ from $O^+(^4S) + D_2$ obtained here are in agreement with those reported by Burley *et al.*[19] Again, we observe good agreement between the σ_L values and experimental cross sections for reaction (5a) at $E_{c.m.} < 0.4$ eV. The observed trend of absolute cross sections for OD^+ from $O^+(^4S,^2D,^2P) + H_2$ are similar to those for OH^+ from $O^+(^4S,^2D,^2P) + H_2$ shown in Fig. 2. That is, at $E_{c.m.} = 0.02$-0.6 eV the cross sections for reactions (19a-19c) are slightly higher than those for reaction (5a), and the cross sections for OD^+ from $O^+(^2P) + D_2$ are significantly lower than those for reactions (5a) and (19a-19c). The $E_{c.m.}$ dependencies of the experimental cross sections in Fig. 4 are also similar to those observed in the $O^+(^4S,^2D,^2P) + H_2$ reactions. Thus, the rationalization presented above to account for the observed $E_{c.m.}$ dependencies of these cross section in the case of $O^+(^4S,^2D,^2P) + H_2$ also holds for the reactions $O^+(^4S,^2D,^2P) + D_2$.

D. D_2^+ and D^+ formed by the reactions $O^+(^4S,^2D,^2P) + D_2$

The cross sections for D_2^+ and D^+ from the reactions of $O^+(^4S,^2D,^2P) + D_2$ in the $E_{c.m.}$ range of 0.03-12 eV are plotted in Fig. 5. The D^+ and D_2^+ cross sections from $O^+(^4S) + D_2$ are comparable to those for H_2^+ and H^+ from $O^+(^4S) + H_2$ obtained by Flesch and Ng.[23] The thresholds shown for both D_2^+ and D^+ agree well with the

Figure 5 Cross sections of D^+ and D_2^+ from the reactions of $O^+(^4S) + D_2$, $O^+(^2D) + D_2$, and $O^+(^2P) + D_2$ in the $E_{c.m.}$ range of 0.02-12 eV. Note that the cross sections for D^+ and D_2^+ from $O^+(^4S) + D_2$ have been multiplied by 10.

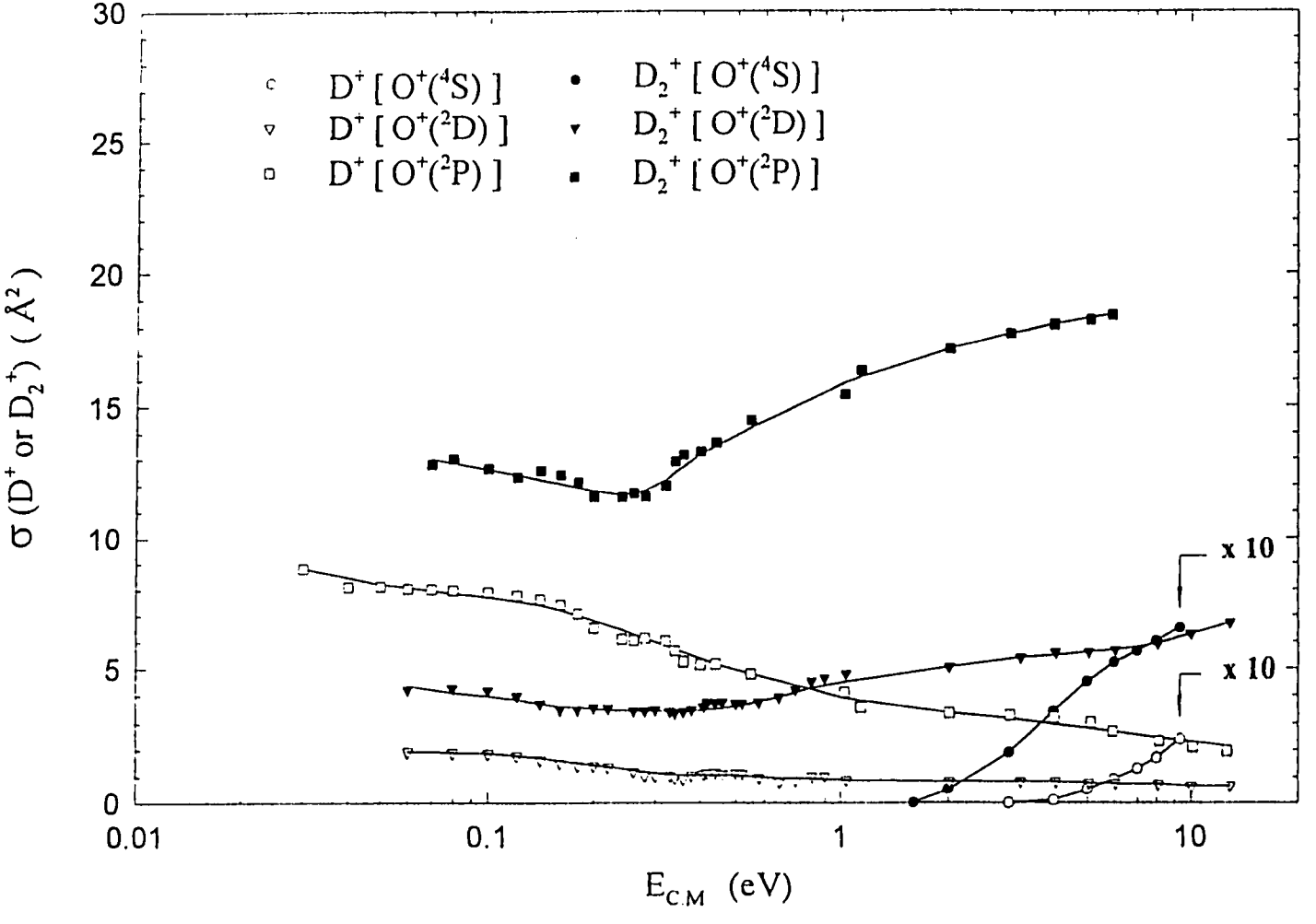
30
25
20
15
10
5
0
0.01
0.1
1
10
σ (D+ or D2+) (Å2)
E C.M (eV)
D+ [O+(4S)]
D+ [O+(2D)]
D+ [O+(2P)]
D2+ [O+(4S)]
D2+ [O+(2D)]
D2+ [O+(2P)]
x 10
x 10

respective thermochemical thresholds of (6) and (7). The negligible D^+ observed at $E_{c.m.}$ < 4.5 eV is taken as evidence that reaction (8) is not important. The D^+ cross sections from the $O^+(^2D)$ + D_2 and $O^+(^2P)$ + D_2 reactions are also similar to those shown in Fig. 3 from $O^+(^2D)$ + H_2 and $O^+(^2P)$ + H_2, respectively. The D^+ cross sections for the excited reactions involving the excited $O^+(^2D,^2P)$ states are significantly higher than those associated with the ground $O^+(^4S)$ state. The observation of finite D^+ cross sections at $E_{c.m.}$ below the thermochemical threshold of 1.21 eV for reaction (21), indicates that D^+ resulting from the collisions of $O^+(^2D)$ + D_2 at $E_{c.m.}$ < 1.2 eV are solely due to reaction (22a). In the case of $O^+(^2P)$ + D_2, both reactions (25) and (26a) are exothermic and may contribute to the D^+ formation at $E_{c.m.}$ = 0.03-12 eV. As pointed out above, both reactions (22a) and (26a) are spin-allowed, whereas the similar reaction (8) is spin-forbidden.

The cross sections for D_2^+ and the $E_{c.m.}$ dependence for reaction (20) are also comparable to those for reaction (12). However, the cross section profiles for the charge transfer reactions of $O^+(^2P)$ + D_2 [reaction (24)] and $O^+(^2P)$ + H_2 [reaction (6)] are different. The cross section for reaction (24) exhibits a slight minimum at $E_{c.m.}$ ≈ 0.25 eV. The efficient production of D_2^+ by reactions (20) and (24) are also ascribed to the near resonant charge transfer processes (30) and (31) leading to vibrationally excited D_2^+.

$$O^+(^2D) + D_2 \rightarrow D_2^+(X^2\Sigma_g^+, v'=10) + O(^3P) \qquad \Delta H^\circ = -0.04 \text{ eV} \qquad (30)$$

$$O^+(^2P) + D_2 \rightarrow D_2^+(X^2\Sigma_g^+, v'=8) + O(^1D) \qquad \Delta H^\circ = 0.03 \text{ eV} \qquad (31)$$

These reactions are similar to reactions (28) and (29). However, because the difference of the reduced masses for D_2^+ and H_2^+ gives rise to different vibrational excitation frequencies, the

vibrational excitation levels of D_2^+ in (30) and (31) are slightly higher than those in (28) and (29), respectively.

It was suggested in previous experiments that the reaction rate constants measured at thermal energies for the $O^+ + H_2$ reaction are significantly lower when a significant fraction of metastable $O^+(^2D,^2P)$ ions are present. We have calculated the sum (σ_T) of the absolute cross sections for all product (OH^+, H_2, and H^+) channels in the $E_{c.m.}$ range of 0.02-7 eV for the individual reactions of $O^+(^4S) + H_2$ (D_2), $O^+(^2D) + H_2$ (D_2), and $O^+(^2P) + H_2$ (D_2). The calculations use the absolute cross sections for OH^+ from $O^+(^4S) + H_2$ at $E_{c.m.} > 0.44$ eV obtained by Burley *et al.*[19] and the absolute cross sections for H_2^+ and H^+ from $O^+(^4S) + H_2$ reported by Flesch and Ng.[23] For the H_2^+ (D_2^+) and H^+ (D^+) cross sections from $O^+(^2D) + H_2$ (D_2) and $O^+(^2P) + H_2$ (D_2) at $E_{c.m.} < 0.04$ (0.06) eV, which are not measured in the present experiment, we use estimated values obtained by extrapolation. Figure 6 compares the σ_T, i.e., $\sigma(OH^+ + H_2 + H^+)$, for the $O^+(^4S) + H_2$, $O^+(^2D) + H_2$, and $O^+(^2P) + H_2$ reactions. The comparison between the σ_T values for the $O^+(^4S) + D_2$, $O^+(^2D) + D_2$, and $O^+(^2P) + D_2$ reactions is shown in Fig. 7. It is interesting to note that although the OH^+ (OD^+) cross sections from $O^+(^2P) + H_2$ (D_2) are significantly lower than those from $O^+(^4S) + H_2$ (D_2) and $O^+(^2D) + H_2$ (D_2), the σ_T values for the $O^+(^4S) + D_2$, $O^+(^2D) + D_2$, and $O^+(^2P) + D_2$ reactions at $E_{c.m.} < 0.4$ eV agree to within 25%. This observation does not support the previous assertion that the reaction rate constants at thermal energies for the $O^+ + H_2$ reaction involving excited $O^+(^2D,^2P)$ states are significantly lower than those associated with the ground $O^+(^4S)$ state.

Figure 6 Comparison of σ_T's for the reactions $O^+(^4S) + H_2$ (solid circle), $O^+(^2D) + H_2$ (solid triangles), and $O^+(^2P) + H_2$ (solid squares). Here σ_T is the sum of the absolute cross sections for OH^+, H_2^+, and H^+.

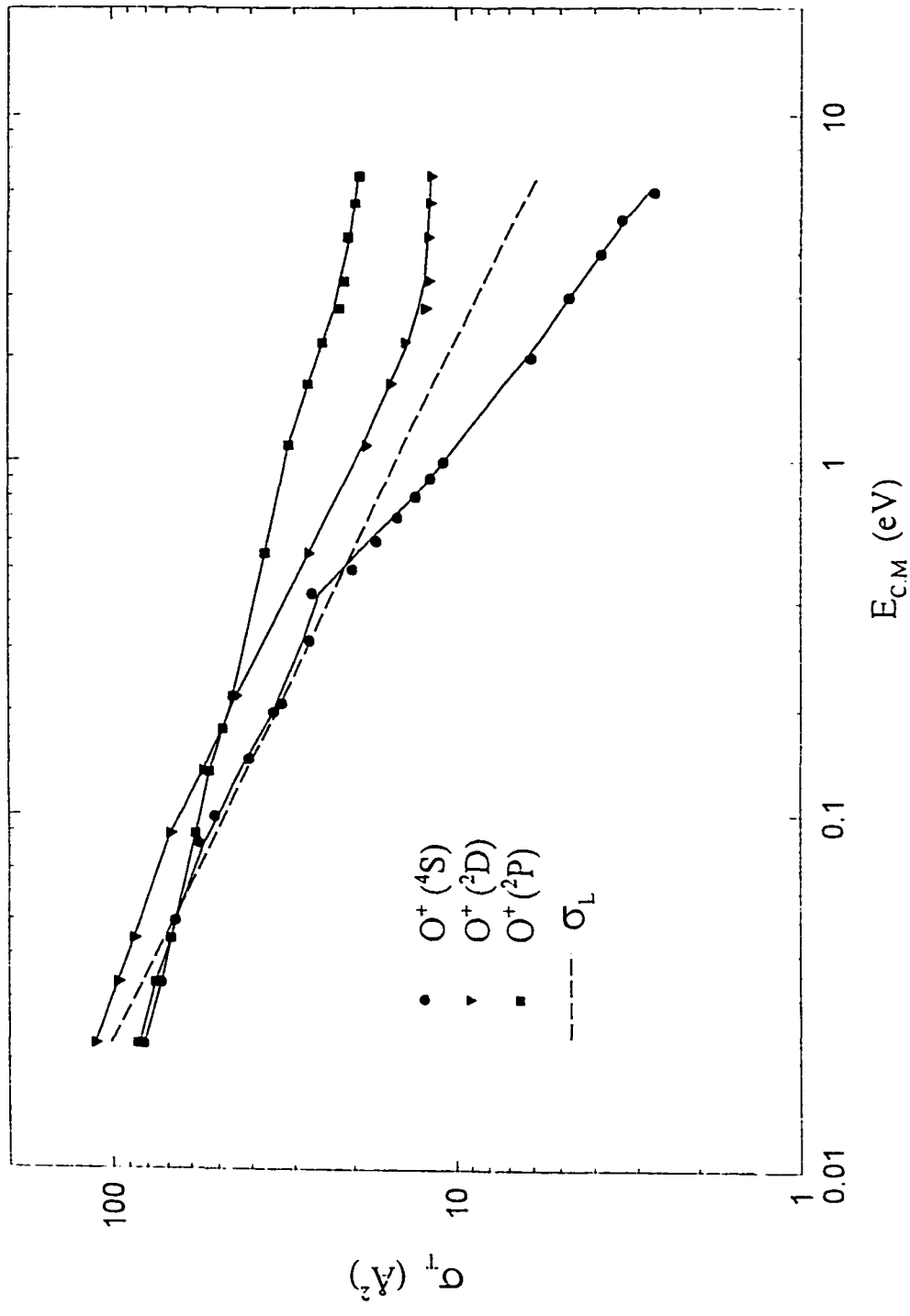
q_T (Å^2)
100
10
1
0.01
0.1
1
10
$E_{C.M}$ (eV)
$O^+(^4S)$
$O^+(^2D)$
$O^+(^2P)$
σ_L

Figure 7 Comparison of σ_T's for the reactions $O^+(^4S) + D_2$ (solid circles), $O^+(^2D) + D_2$ (solid triangles), and $O^+(^2P) + D_2$ (solid squares). Here σ_T is the sum of the absolute cross sections for OD^+, D_2^+, and D^+ at a given $E_{c.m.}$.

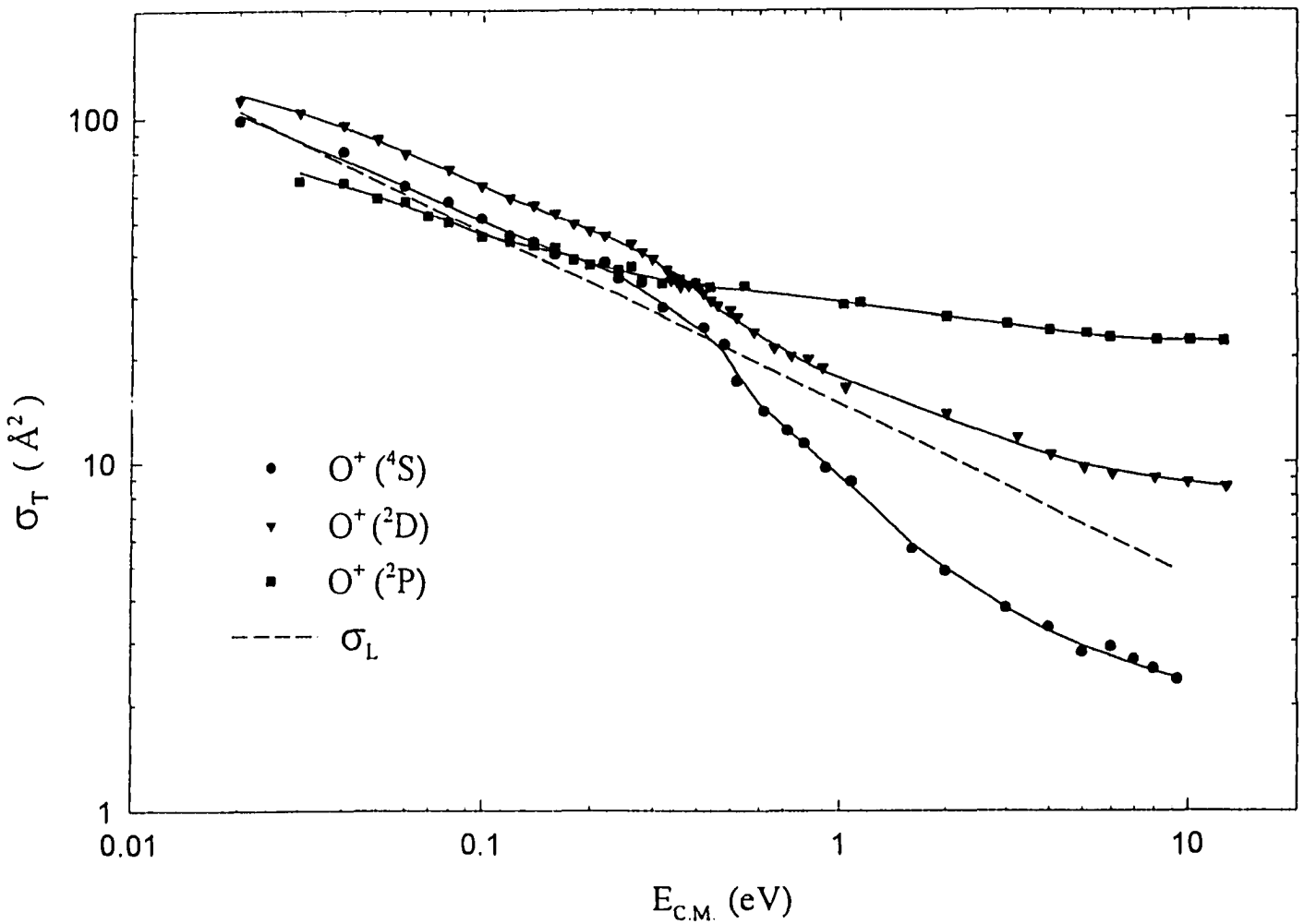
100
10
1
0.01
0.1
1
10
σ_T (Å^2)
$E_{C.M.}$ (eV)
O^+ (^{4}S)
O^+ (^{2}D)
O^+ (^{2}P)
σ_L

At $E_{c.m.}$ > 0.4 eV, the σ_T values for $O^+(^4S)$ + H_2 (D_2) [$\sigma_T(O^+(^4S)$] are lower than those for $O^+(^2D)$ + H_2 (D_2) [$\sigma_T(O^+(^2D)$], which in turn are lower than those for $O^+(^2P)$ + H_2 (D_2) [$\sigma_T(O^+(^2D)$]. The higher σ_T values for the reactions involving the excited $O^+(^2D)$ and $O^+(^2P)$ are expected due to the increase in the number of available product channels compared to those for the reactions associated with the $O^+(^4S)$ ground state. It is interesting that the LGS model, which does not take into account the electronic structure of the reactant ion, has provided reasonable predictions for the cross sections for OH^+ (OD^+) from $O^+(^4S,^2D,^2P)$ + H_2 (D_2). We hope that this experiment will stimulate further theoretical investigations of the $O^+(^4S,^2D,^2P)$ + H_2 (D_2) ion-molecule reaction system.

IV. CONCLUSIONS

Using the TQDO photoionization apparatus, together with DCT-OIT and DRP methods developed recently in our laboratory, we have measured the absolute cross sections for OH^+ (OD^+), H_2^+ (D_2^+), and H^+ (D^+) formed in the reactions of $O^+(^4S)$ + H_2 (D_2), $O^+(^2D)$ + H_2 (D_2), and $O^+(^2P)$ + H_2 (D_2) in the $E_{c.m.}$ range of 0.02-12 eV. While the observed cross sections for OH^+ (OD^+) from $O^+(^4S)$ + H_2 (D_2) and $O^+(^2D)$ + H_2 (D_2) at $E_{c.m.}$ < 0.5 eV are in accord with the predictions of the LGS model, the OH^+ (OD^+) from $O^+(^2P)$ + H_2 (D_2) are significantly lower than the LGS predictions. As expected, due to the exothermic nature of the charge transfer reactions involving $O^+(^2D)$ and $O^+(^2P)$, the cross sections for H_2^+ (D_2^+) from $O^+(^2D)$ + H_2 (D_2) and $O^+(^2P)$ + H_2 (D_2) are significantly higher than those from $O^+(^4S)$ + H_2 (D_2). The H^+ (D^+) cross sections from $O^+(^2P)$ + H_2 (D_2) and $O^+(^2D)$ + H_2 (D_2) are also significantly higher than those from $O^+(^4S)$ + H_2 (D_2). The $E_{c.m.}$ dependencies observed

for H^+ (D^+) suggest that the H^+ (D^+) ions from $O^+(^2D)$ and $O^+(^2P)$ are identified mostly with the H^+ (D^+) + OH (OD) channel, whereas the H^+ (D^+) ions from $O^+(^4S)$ are due to the H^+ (D^+) + O + H (D) channel. The higher cross sections for H^+ (D^+) from $O^+(^2D)$ + H_2 (D_2) and $O^+(^2P)$ + H_2 (D_2) are attributed to the exothermic nature of reactions (14a), (18a), (22a), and (26a). Furthermore, the latter reactions also obey the spin-conservation rule.

The σ_T values for $O^+(^4S)$ + H_2 (D_2), $O^+(^2D)$ + H_2 (D_2), and $O^+(^2P)$ + H_2 (D_2) at $E_{c.m.} < 0.5$ eV are found to agree within 25%, whereas at $E_{c.m.} > 0.5$ eV the σ_T values are in the order: $\sigma_T[O^+(^2P)] > \sigma_T[O^+(^2D)] > \sigma_T[O^+(^2S)]$. The higher σ_T values for $O^+(^2D)$ and $O^+(^2P)$ are ascribed to the increased number of accessible product channels for the reactions involving excited $O^+(^2D)$ and $O^+(^2P)$ ions.

Acknowledgments:

This work was supported by the National Science Foundation Grant No. ATM-9521558.

References

1. A. Dalgarno and J. L. Fox, in "Unimolecular and Bimolecular Ion-Molecule Reaction Dynamics", edited by C. Y. Ng, T. Baer, and I. Powis, *Wiley Series in Ion Chem. and Phys.* (Wiley, Chichester, 1994), p. 1.
2. P. M. Banks and G. Kockarts, *Aeronomy, Part A* (Academic, New York, 1973), pp. 14, 257.
3. M. R. Torr and D. G. Torr, *Rev. Geophys. Space Phys.* 20, 91 (1982).
4. A. Dalgarno and M. B. McElroy, *Planet. space Sci.* 13, 947 (1965).

5. R. J. W. Henry, *Astrophys. J.* 161, 1153 (1970).

6. J. L. Kohl, G. P. Lafyatis, H. P. Palenius, and W. H. Parkinson, *Phys. Rev. A* 18, 571 (1978).

7. D. G. Torr and N. Orsini, *Planet. Space Sci.* 25, 1171 (1977).

8. D. G. Torr and N. Orsini, *Geophys. Res. Lett.* 5, 657 (1978).

9. M. R. Torr and D. G. Torr, *Geophys. Res. Lett.* 7, 103 (1980).

10. E. E. Ferguson, F. C. Fehsenfeld, and D. L. Albritton, in *Gas Phase Ion Chemistry*, edited by M. T. Bowers (Academic, New York, 1979), Vol. 1, p. 45.

11. M. Mendillo, G. S. Hawkins and J. A. Klobuchar, *J. Geophys. Res.* **80**, 2217 (1975).

12. W. D. Watson, *Accounts Chem. Res.* **10**, 221 (1977).

13. W. W. Duley and D. A. Williams, *Interstellar Chemistry* (Academic Press, New York, 1984).

14. K. T. Gillen, B. H. Mahan and J. S. Winn, *J. Chem. Phys.* **58**, 5373 (1973); **59**, 6380 (1973).

15. H. H. Harris and J. J. Leventhal, *J. Chem. Phys.* **58**, 2333 (1973); **64**, 3185 (1976).

16. F. C. Fehsenfeld, A. L. Schmeltekopf and E. E. Ferguson, *J. Chem. Phys.* **46**, 2802 (1967).

17. J. K. Kim, L. P. Thread and W. J. Huntress, Jr., *J. Chem. Phys.* **62**, 45 (1975).

18. D. H. Smith, N. G. Adams and T. M. Miller, *J. Chem. Phys.* **69**, 308 (1978).

19. J. D. Burley, K. M. Ervin and P. B. Armentrout, Int. *J. Mass Spectrom. Ion Proc.* **80**, 153 (1987).

20.L. S. Sunderlin and P. B. Armentrout, *Chem. Phys. Lett.* **167**, 188 (1990).

21.Y. Xu, E. W. Thomas and T. F. Moran, *J. Phys. B: At. Mol. Opt. Phys.* **23**, 1235 (1990).

22.T. F. Moran and J. B. Wilcox, *J. Chem. Phys.* **69**, 1397(1978).

23.G. D. Flesch and C. Y. Ng, *J. Chem. Phys.* **94**, 2372 (1991).

24.J. M. Hoffman, G. H. Miller, and G. J. Lockwood, *Phys. Rev. A* **25**, 1930 (1982).

25.W. L. Nutt, R. W. McCullough, and H. B. Gilbody, *J. Phys. B* **12**, L157 (1978).

26.R. A. Rouse, *J. Chem. Phys.* **64**, 1244 (1976).

27.G. Chambaud, P. Millie and B. Levy, *J. Phys. B* **11**, L211 (1978).

28.M. Gerard-Ain, *J. Phys. B* **17**, L505 (1984).

29.C. F. Jackels, *J. Chem. Phys.* **72**, 4873 (1980).

30.D. M. Hirst, *J. Phys. B* **17**, L505 (1984).

31.M. Gonzalez, A. Aguilar and J. Virgili, *Chem. Phys. Lett.* **113**, 179 (1985).

32.M. Gonzalez, A. Aguilar and M. Gilibert, *Chem. Phys.* **131**, 335 (1989);**131**, 347 (1989).

33.J. C. Leclerc, J. A. Horsley and J. C. Lorquet, *Chem. Phys.* **4**, 337 (1974).

34.A. J. Lorquet and J. C. Lorquet, *Chem. Phys.* **4**, 353 (1974).

35.J. A. Smith, P. Jorgensen and Y. Ohrn, *J. Chem. Phys.* **62**, 1285 (1975).

36.F. O. Ellison and M. L. McCandlish, *J. Phys. B* **15**, L229 (1982).

37.C. E. Dateo and D. C. Clary, *J. Chem. Soc. Faraday Trans.* **II 85**, 1685 (1989).

38.F. Fiquet-Fayard and P.-M. Guyon, *Mol. Phys.* **11**, 17 (1966).

39.S. G. Lias, J. E. Bartmess, J. F. Liebman, J. L. Holmes, R. D. Levin, and W. G. Mallard, *J. Phys. Chem. Ref. Data*, **17** (1988), Suppl. No. 1.

40.A. Henglein, *Molecular Beams and Reaction Kinetics* edited by Ch. Schlier (Academic Press, New York, 1970), p. 154.

41.G. Gioumousis and D. P. Stevenson, *J. Chem. Phys.* 29, 294 (1958).

42.H. M. Rosenstock, K. Draxl, B. W. Steiner, and J. T. Herron, *J. Phys. Chem. Ref. Data* **6**, 1 (1977).

43.X. Li, Y.-L. Huang, G.D. Flesch and C.Y. Ng, *Rev. Sci. Instrum.* **66**, 2871 (1995).

44.X. Li, Y.-L. Huang, G.D. Flesch and C.Y. Ng, *Rev. Sci. Instrum.* **65**, 3724 (1994).

45.G. D. Flesch, S. Nourbakhsh, and C. Y. Ng, *J. Chem. Phys.* **92**, 3590 (1990).

46.G. D. Flesch and C. Y. Ng, *J. Chem. Phys.* **92**, 3235 (1990).

47.G. D. Flesch and C. Y. Ng, *J. Chem. Phys.* **89**, 3381 (1988).

48.G. D. Flesch and C. Y. Ng, *J. Chem. Phys.* **92**, 2876 (1990).

49.N. R. Daly, *Rev. Sci. Instrum.* **31**, 264 (1960).

50.G. O. Brink, *Rev. Sci. Instrum.* **37**, 857, 1626 (1966).

51.G. Bischof and F. Linder, *Z. Phys. D* 1, 303 (1986).

52.D. Gerlich, in "State-to-State Ion-Molecule Reaction Dynamics I: Experiment", edited by C. Y. Ng and M. Baer, *Adv. Chem. Phys.*, **82** (Wiley, New York, 1992), p. 1; M. Scherbarth, Diplom thesis, University of Freiburg, 1988.

53.These values correspond to Ne^+ formed in the $^2P_{1/2}$ spin-orbit excited state.

54.G. D. Flesch and C. Y. Ng, *J. Geophys. Res.* **96**, 21407 (1991).

55.G. D. Flesch, S. Nourbakhsh, and C. Y. Ng, *J. Chem. Phys.* **95**, 3381 (1991).

56.G. D. Flesch, S. Nourbakhsh, and C. Y. Ng, *J. Chem. Phys.* **92**, 3590 (1990).

57.K. P. Huber and G. Herzberg, "Molecular Spectra and Molecular Structure: Constants of Diatomic Molecules" (van Nostrand Reinhold, New York, 1979).

58.J. O. Hirschfelder, C. R. Curtiss and R. B. Burd, *Molecular Theory of Gases and Liquids* (Wiley, New York, 1954), p. 94.

59.B. R. Rowe, D. W. Fahey, F. C. Fehsenfeld and D. L. Albritton, *J. Chem. Phys.* **73**, 194 (1980)

CHAPTER V

A STATE-SELECTED STUDY OF THE ION-MOLECULE REACTIONS $O^+(^2D,^2P) + H_2O$

A paper submitted to the Journal of Chemical Physics

X. Li, Y.-L. Huang, G. D. Flesch, and C. Y. Ng

Abstract:

State-selected absolute cross sections for H_2O^+ and OH^+ formed by the $O^+(^2D,^2P)$ + H_2O reactions have been measured in the center-of-mass collision energy ($E_{c.m.}$) range of $\approx$0.10-30 eV. The charge transfer cross sections for $O^+(^2D)$ + H_2O are significantly higher than those for $O^+(^4S)$ + H_2O. This observation is attributed to the increased number of accessible exothermic product channels for $O^+(^2D)$ + H_2O. While the H_2O^+ cross sections for $O^+(^2P)$ + H_2O are comparable to those from $O^+(^4S)$ + H_2O at $E_{c.m.} \geq 1$ eV, the H_2O^+ cross sections for $O^+(^2P)$ + H_2O at $E_{c.m.} < 1$ eV are substantially lower than those for $O^+(^4S)$ + H_2O. The lower H_2O^+ cross sections observed for $O^+(^2P)$ + H_2O are rationalized as due to further dissociation of excited charge transfer H_2O^+ ions and/or the efficient competition of the OH^+ + OH product channel. The cross sections for OH^+ from $O^+(^2D,^2P)$ + H_2O are significantly greater than those from $O^+(^4S)$ + H_2O. The majority of OH^+ ions from $O^+(^2D,^2P)$ + H_2O are associated with exothermic channels corresponding to the formation $OH^+(X^3\Sigma^-,^1\Delta,A^3\Pi)$ + OH. The comparison of the sum (σ_T) of the cross

sections for H_2O^+ and OH^+ from $O^+(^4S)$ + H_2O to those from $O^+(^2D)$ + H_2O and $O^+(^2P)$ + H_2O shows that σ_T's for $O^+(^4S)$ + H_2O and $O^+(^2P)$ + H_2O are comparable, whereas the σ_T values for $O^+(^2D)$ + H_2O are greater than those for $O^+(^4S)$ + H_2O and $O^+(^2P)$ + H_2O. The σ_T values are found to conform with the $1/E_{c.m.}$ dependence at low $E_{c.m.}$'s, indicating that the ion-dipole interaction plays an important role in the formation of the long-lived collision complexes. The high cross sections for H_2O^+ and OH^+ from $O^+(^2D,^2P)$ + H_2O observed here suggest that these reactions should be included in the simulation of the H_2O^+ and H_3O^+ ion density data obtained in space-borne mass spectrometric experiments.

I. INTRODUCTION

The flights of large space vehicles, such as the space shuttle, are strong perturbers of the ambient plasma environment of the ionosphere.[1-3] Space-borne mass spectrometric experiments reveal high densities of H_2O^+ and H_3O^+ in the vicinity of the shuttle.[2,4,5] Since O^+ comprises more than 90% of the ionic constituents of the ionosphere at low-Earth-orbit altitudes,[6-9] it is generally recognized that the primary source of observed H_2O^+ ions is due to charge transfer collisions between atmospheric O^+ ions and H_2O molecules, which are the main constituents of the contaminant cloud surrounding the space shuttle.[1-5,10-13] Taking into account the speed of the spacecraft, these ion-molecule reactions, which essentially involve collisions of O^+ ions with H_2O on the surface of the shuttle, takes place in the center-of-mass collision energy ($E_{c.m.}$) range of 2-9 eV.[1] The H_3O^+ ions result from subsequent reactions between H_2O^+ and H_2O.

The charge transfer reaction of O^+ + H_2O has been the subject of many previous studies.[10,13-19] Recent experiments[10,15-19] have been stimulated by the interest of understanding the atmospheric plasma environment due to spacecraft-atmosphere interactions. The modeling of ion density data from space-borne mass spectrometric experiments[1,10-13] requires accurate cross sections or rate coefficients for the reaction of O^+ + H_2O. Since H_2O has

a large dipole moment (μ = 1.85 D), the ion-dipole interaction is expected to dominate in the long range. Thus, accurate absolute cross sections for this reaction measured as a function $E_{c.m.}$ should be useful for testing theoretical schemes beyond the Langevin-Gioumousis-Stevens model, which is only applicable to ion-molecule reaction systems involving a pure ion-induced dipole potential.[20] The absolute cross sections for the ground state reactions,

$$O^+(^4S) + H_2O \rightarrow H_2O^+ + O \qquad \Delta H° = -1.01 \text{ eV} \qquad (1)$$

$$\rightarrow OH^+ + OH \qquad \Delta H° = 0.11 \text{ eV} \qquad (2)$$

$$\rightarrow OH^+ + O + H, \qquad \Delta H° = 4.55 \text{ eV} \qquad (3)$$

have been measured previously in the $E_{c.m.}$ range of 0.10-50 eV.[14-19] The heats of reaction ($\Delta H°$) for processes (1)-(3) are calculated assuming that the atomic and molecular neutrals and ions are in their ground states.[21,22] In addition to the charge transfer channel, the recent experiment of our laboratory[19] has identified channels (2) and (3) despite their cross sections being significantly lower than that for channel (1).

To our knowledge, studies on the reactions of $O^+(^2D) + H_2O$ and $O^+(^2P) + H_2O$ have not been made previously. It is well known that the O^+ ions formed by solar vacuum ultraviolet (VUV) photoionization of O atoms in the ionosphere consist of three states with branching ratios of $O^+(^4S):O^+(^2D):O^+(^2P)$ = 0.43:0.29:0.28.[6-9,23] Since the excited $O^+(^2D)$ and $O^+(^2P)$ states are metastable with radiative lifetimes of 3.6 hr and 4.57 s, respectively, the reactions involving these metastable O^+ ions should also play an important role for modeling the H_2O^+ and H_3O^+ ion density data observed in space-borne mass spectrometric experiments.[24-26]

By using the dissociative charge transfer (DCT) reactions,

$$Ne^+ + O_2 \rightarrow Ne + O^+(^4S,^2D) + O \quad (4)$$

$$He^+ + O_2 \rightarrow He + O^+(^4S,^2D,^2P) + O, \quad (5)$$

together with octopole ion trap (OIT) techniques, we have recently succeeded in preparing state-specific $O^+(^2D)$ and $O^+(^2P)$ ion beams with sufficiently high intensities for scattering experiments.[27] In order to improve the kinetic energy resolution for $O^+(^2D)$ and $O^+(^2P)$ ion beams prepared by the DCT-OIT method, we have also developed a differential retarding potential (DRP) scheme[28]. Applying the DCT-OIT and DRP methods, we have obtained absolute cross sections for a series of atmospheric ion-molecule reactions involving $O^+(^2D)$ and $O^+(^2P)$.[29,30] Here, we report the results for the $O^+(^2D) + H_2O$ and $O^+(^2P) + H_2O$ reactions. Cross sections for these reactions are compared to those for $O^+(^4S) + H_2O$.[19]

II. EXPERIMENT

The experimental arrangement and procedures for cross section measurements using the triple-quadruple double-octopole (TQDO) apparatus have been described in detail[31-34]. The TQDO apparatus essentially consists of, in sequential order, a VUV photoionization ion source or an electron impact ionization ion source, a reactant quadruple mass spectrometer (QMS), a lower radio frequency (RF) octopole ion guide reaction gas cell (RFOIGGC), a middle QMS, an upper RFOIGGC, a product QMS, and a Daly-type scintillation ion detector.[35] The electron impact ionization ion source used here is of the Brink design[36] and has been added to the TQDO apparatus recently. The TQDO apparatus is partitioned into five chambers which are separately evacuated by liquid nitrogen- or freon-trapped diffusion pumps. The differential pumping arrangement is important for the reactant ion preparation scheme and the cross section measurement experiments described here.

The principle and procedures for the preparation of $O^+(^2D)$ and $O^+(^2P)$ reactant ion beams have been described in detail.[27] Briefly, $O^+(^2D)$ and $O^+(^2P)$ are produced by DCT

processes (4) and (5), respectively. Basically, rare gas ions (Ne^+, He^+) are generated in the ionization region by electron impact. These ions are then extracted from the ionization region and mass-selected by the reactant QMS. The DCT reaction (4) or (5) take place in the lower gas cell, into which oxygen gas has been introduced. In reaction (5), which is exothermic, a mixture of $O^+(^4S)$, $O^+(^2D)$, and $O^+(^2P)$ are produced with well resolved kinetic energy distributions.[37,38] At $E_{c.m.}$ = 1-2 eV, $O^+(^2P)$ ions have lower kinetic energies than those for $O^+(^4S)$ and $O^+(^2D)$, and are found to be the dominant product channel, with a branching ratio of 50-60%. The idea of the state-selection method is to lower the trapping voltage of the lower RF octopole so that energetic $O^+(^4S)$ and $O^+(^2D)$ ions escape from the octopole trap and slow $O^+(^2P)$ ions remain trapped. This essentially is an $O^+(^2P)$ enrichment scheme. Under the present experimental conditions which maximize the transmission fraction for $O^+(^2P)$, we estimate that the $O^+(^2P)$ ion beam has a purity of 89%, with the remaining fraction about 5% each for $O^+(^4S)$ and $O^+(^2D)$. The formation of $O^+(^2D)$ and $O^+(^2P)$ from reaction (4) is endothermic by 0.48 (0.38)[39] and 2.18 (2.10)[39] eV, respectively. Thus, the formation of $O^+(^2P)$ can be avoided at $E_{c.m.} < 2.1$ eV. The $E_{c.m.}$ dependence of the cross section for reaction (4) reveals a sharp onset at the thermochemical threshold for the formation of $O^+(^2D)$, indicating that the formation of $O^+(^2D)$ is efficient,[28] in accordance with the DCT mechanism.[33,40,41] By choosing $E_{c.m.}$ = 0.73 eV, and by lowering the effective trapping potential of the RF octopole ion trap to lose the $O^+(^4S)$ ions, we estimate that the $O^+(^2D)$ ion beam used in the present experiment has a purity $\geq$90%.

The state-selected $O^+(^2D)$ [$O^+(^2P)$] ions thus formed are mass-selected by the middle QMS and transmitted into the upper gas cell where the reactions between $O^+(^2D)$ [$O^+(^2P)$] and H_2O occur. We find that H_3O^+ ions are produced by the reaction of the slow charge transfer product H_2O^+ and the H_2O in the gas cell. In order to minimize the formation of secondary H_3O^+, the H_2O gas cell pressure used in this experiment is $<6\times10^{-5}$ Torr.

Calculations of the absolute cross sections for H_2O^+ reported here have taken into account this secondary process. The product ions are detected using the upper QMS and the Daly-type scintillation ion detector. At each $E_{c.m.}$, the product ion collection efficiency is maximized by carefully optimizing the transmission of the ion lenses, product QMS, and the octopole ion guide. The uncertainties for absolute cross sections reported here are estimated to be $\leq$ 25%. However, the uncertainties for relative cross sections are believed to be smaller than 10%.

In the $E_{c.m.}$ range above 1.2 eV, the laboratory kinetic energies for the Ne^+, He^+ and O^+ ion beams are measured by the retarding potential method, which has been detailed previously.[32,42] Because of the relatively large energy spread of $O^+(^2D)$ and $O^+(^2P)$ reactant ions generated by reactions (4) and (5), respectively, the DRP method is used to improve the kinetic energy resolution of the O^+ reactant ion beam in the $E_{c.m.}$ range below 1.2 eV. The energy resolution thus achieved for $E_{c.m.}$ in this study is ± 0.1 eV.

III. RESULTS AND DISCUSSION

The possible channels and their energetics[21,22,43] resulting from the reactions of $O^+(^2D)$ + H_2O and $O^+(^2P)$ + H_2O are:

$$O^+(^2D) + H_2O \rightarrow H_2O^+(\tilde{X}^2B_1) + O(^3P) \qquad \Delta H^\circ = -4.33 \text{ eV} \qquad (6a)$$

$$\rightarrow H_2O^+(\tilde{X}^2B_1) + O(^1D) \qquad \Delta H^\circ = -2.36 \text{ eV} \qquad (6b)$$

$$\rightarrow H_2O^+(\tilde{X}^2B_1) + O(^1S) \qquad \Delta H^\circ = -0.14 \text{ eV} \qquad (6c)$$

$$\rightarrow H_2O^+(\tilde{A}^2A_1) + O(^3P) \qquad \Delta H^\circ = -3.22 \text{ eV} \qquad (6d)$$

$$\rightarrow H_2O^+(\tilde{A}^2A_1) + O(^1D) \qquad \Delta H^\circ = -1.25 \text{ eV} \qquad (6e)$$

$$\rightarrow OH^+(X^3\Sigma^-) + OH \qquad \Delta H^\circ = -3.21 \text{ eV} \qquad (7a)$$

$$\rightarrow OH^+(^1\Delta) + OH \qquad \Delta H^\circ = -1.01 \text{ eV} \qquad (7b)$$

$$\rightarrow OH^+ + O + H \qquad \Delta H^\circ = 1.23 \text{ eV} \qquad (8)$$

$$O^+(^2P) + H_2O \rightarrow H_2O^+(\tilde{X}^2B_1) + O(^3P) \quad \Delta H^\circ = -6.03 \text{ eV} \quad (9a)$$

$$\rightarrow H_2O^+(\tilde{X}^2B_1) + O(^1D) \quad \Delta H^\circ = -4.06 \text{ eV} \quad (9b)$$

$$\rightarrow H_2O^+(\tilde{X}^2B_1) + O(^1S) \quad \Delta H^\circ = -1.84 \text{ eV} \quad (9c)$$

$$\rightarrow H_2O^+(\tilde{A}^2A_1) + O(^3P) \quad \Delta H^\circ = -4.91 \text{ eV} \quad (9d)$$

$$\rightarrow H_2O^+(\tilde{A}^2A_1) + O(^1D) \quad \Delta H^\circ = -2.94 \text{ eV} \quad (9e)$$

$$\rightarrow H_2O^+(\tilde{A}^2A_1) + O(^1S) \quad \Delta H^\circ = -0.72 \text{ eV} \quad (9f)$$

$$\rightarrow H_2O^+(\tilde{B}^2B_2) + O(^3P) \quad \Delta H^\circ = -1.47 \text{ eV} \quad (9g)$$

$$\rightarrow OH^+(X^3\Sigma^-) + OH \quad \Delta H^\circ = -4.91 \text{ eV} \quad (10a)$$

$$\rightarrow OH^+(^1\Delta) + OH \quad \Delta H^\circ = -2.71 \text{ eV} \quad (10b)$$

$$\rightarrow OH^+(A^3\Pi) + OH \quad \Delta H^\circ = -1.38 \text{ eV} \quad (10c)$$

$$\rightarrow OH^+(X^3\Sigma^-) + OH(A^2\Sigma^+) \quad \Delta H^\circ = -0.86 \text{ eV} \quad (10d)$$

$$\rightarrow OH^+ + O + H \quad \Delta H^\circ = -0.47 \text{ eV} \quad (11)$$

In the calculation of ΔH° values for these reactions, the neutrals and ions are assumed to be in their ground states unless specified otherwise. In the $E_{c.m.}$ range of interest to the present experiment, the charge transfer product H_2O^+ ions may be formed in the excited $H_2O^+(\tilde{A}^2A_1)$ [reactions (6d), (6e), and (9d-9f)] and $H_2O^+(\tilde{B}^2B_2)$ [reaction (9g)] states. The accompanying O atoms can be produced in the excited $O(^1D)$ [reactions (6b), (6e), (9b), (9e)] and $O(^1S)$ [reactions (6c), (9c), (9f)] states. Furthermore, excited $OH^+(^1\Delta)$ [reactions (7b) and (10b)], $OH^+(A^3\Pi)$ [reaction (10c)], and $OH(A^2\Sigma^+)$ [reaction (10d)] may also be formed in H-abstraction processes. We note that since metastable $O^+(^2D)$ and $O^+(^2P)$ states are above the ground $O^+(^4S)$ state by 3.32 and 5.02 eV,[22] all these reactions which produce excited H_2O^+, OH^+, O, and OH species are exothermic. Within the sensitivity of the present experiment, H^+ ions were not observed in the reactions of $O^+(^4S,^2D,^2P) + H_2O$.[19]

A. H_2O^+ formed by the reactions of $O^+(^4S,^2D,^2P) + H_2O$

Figure 1 compares the absolute cross sections (σ) for H_2O^+ from the charge transfer reactions of $O^+(^4S) + H_2O$, $O^+(^2D) + H_2O$, and $O^+(^2P) + H_2O$ in the $E_{c.m.}$ range of 0.15-50 eV. The cross sections for H_2O^+ from $O^+(^4S) + H_2O$ have been measured recently in our laboratory.[19] The charge transfer cross sections for these reactions are found to be >100 Å^2 at 0.15 eV and to decrease rapidly as $E_{c.m.}$ is increased. This observation is consistent with the conclusion that the ion-molecule reactions of $O^+(^4S,^2D,^2P) + H_2O$ take place via a long-lived complex mechanism at low $E_{c.m.}$'s.

At $E_{c.m.} < 0.5$ eV, the cross sections for H_2O^+ from $O^+(^2D) + H_2O$ are about 10% higher than those from $O^+(^4S) + H_2O$. This difference increases to $\approx$60-100% in the $E_{c.m.}$ range of 1-30 eV. The higher charge transfer cross sections for $O^+(^2D) + H_2O$ compared to those for $O^+(^4S) + H_2O$ can be rationalized by the fact that exothermic product channels (6b)-6(e) available to $O^+(^2D) + H_2O$ are energetically inaccessible to $O^+(^4S) + H_2O$ at low $E_{c.m.}$'s.

While the cross sections for H_2O^+ from $O^+(^2P) + H_2O$ are comparable to those from $O^+(^4S) + H_2O$ at $E_{c.m.} \geq 1$ eV, the cross sections for H_2O^+ from $O^+(^2P) + H_2O$ are significantly lower than those from $O^+(^4S) + H_2O$ at $E_{c.m.} < 1$ eV. Considering that the exothermicity of 6.09 eV for reaction (9a) is greater than the dissociation energy of 5.69 eV for the OH^+-H bond,[21] it is likely that $OH^+ + H$ are formed from spontaneous dissociation of a fraction of the excited H_2O^+ ions resulting from the charge transfer collisions of $O^+(^2P) + H_2O$. As shown below, this rationalization is supported in part by the high cross sections for OH^+ from $O^+(^2P) + H_2O$ at low $E_{c.m.}$'s. The mechanism for the production of OH^+ from excited H_2O^+ ions may involve the predissociative $H_2O^+(\tilde{B}^2B_2)$ electronic state formed in reaction (9g). The predissociation of $H_2O^+(\tilde{B}^2B_2)$ is known to yield both OH^+ and H^+.[44] However, since H^+ ions are not found in the collisions of $O^+ + H_2O$,[19] the involvement of

Figure 1 Comparison of the cross sections for H_2O^+ from $O^+(^4S) + H_2O$ (solid circles), $O^+(^2D) + H_2O$ (solid squares), and $O^+(^2P) + H_2O$ (solid triangles) in the $E_{c.m.}$ range of 0.15-50 eV.

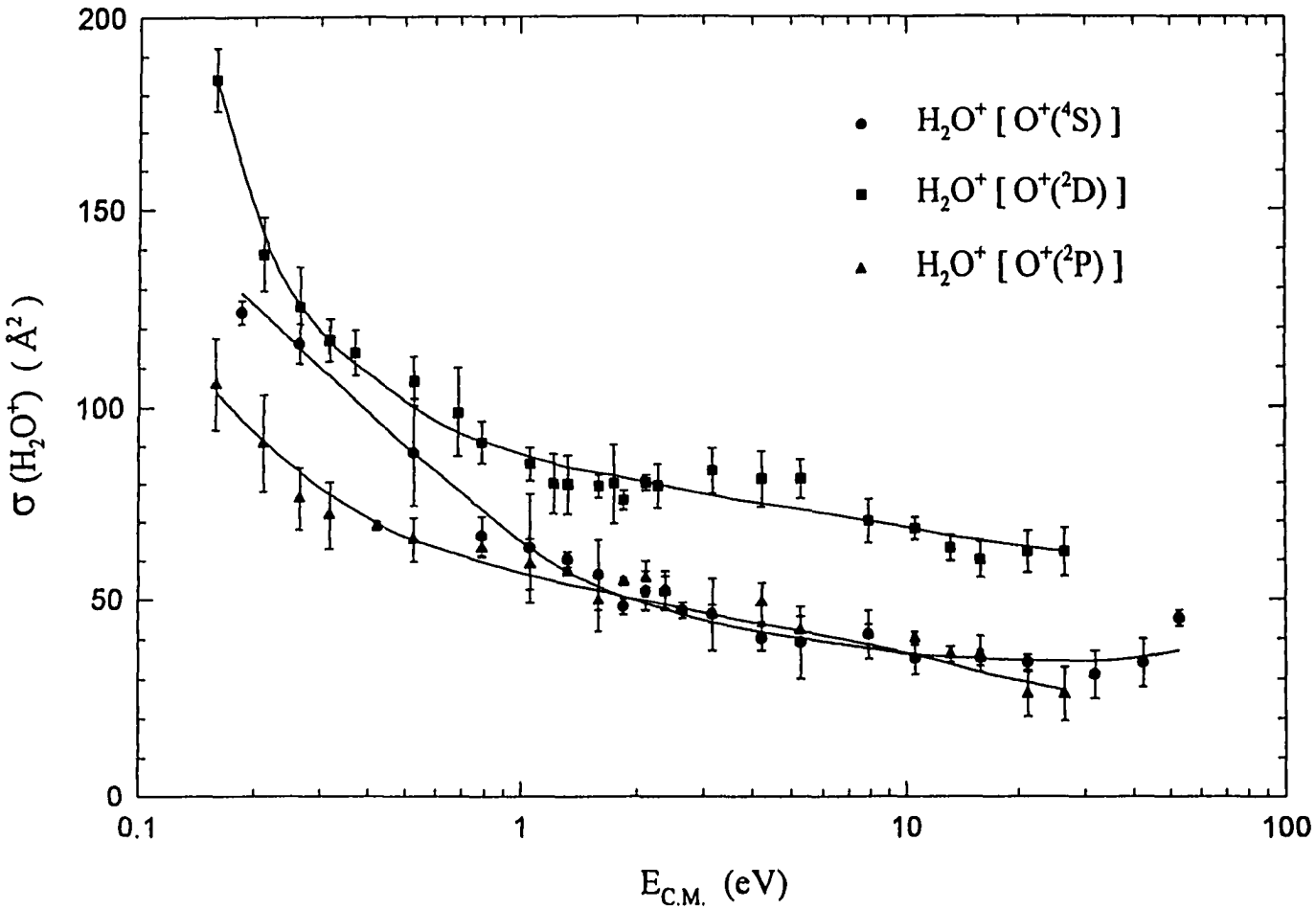
200
150
100
50
0
0.1
1
10
100
σ (H2O+) (Å2)
EC.M. (eV)
H2O+ [O+(4S)]
H2O+ [O+(2D)]
H2O+ [O+(2P)]

$H_2O^+(\tilde{B}^2B_2)$ as a predissociative state for the formation of OH^+ remains to be confirmed.

B. OH^+ formed by the reactions of $O^+(^4S,^2D,^2P) + H_2O$

The cross sections for OH^+ from $O^+(^4S) + H_2O$ [reactions (2) and (3)], $O^+(^2D) + H_2O$ [reactions (7a), (7b) and (8)], and $O^+(^2P) + H_2O$ [reactions (10a-10d) and (11)] are compared in Fig. 2. The cross sections for OH^+ from $O^+(^4S) + H_2O$ are taken from Ref. 19. As shown in the figure, the OH^+ cross sections from both $O^+(^2D) + H_2O$ and $O^+(^2P) + H_2O$ are significantly higher than those from $O^+(^4S) + H_2O$. This observation indicates that the formation of OH^+ from $O^+(^2D,^2P) + H_2O$ should be included in the analysis of ion density data observed in space shuttle surroundings in the ionosphere.[2,4,5] The $E_{c.m.}$ dependencies of the OH^+ cross section curves of the three O^+ reactant states are different. The OH^+ cross section curve associated with $O^+(^2D)$ gradually rises from $E_{c.m.} = 0.1$ eV and shows a broad peak at ≈ 0.8 eV, only to decrease slowly towards higher $E_{c.m.}$'s. Stemming from the fact that significant intensities of OH^+ are observed at $E_{c.m.}$ below the thermochemical threshold for reaction (8), we conclude that the exothermic channels (7a) and (7(b) play an important role in the production of OH^+. As observed in the reaction of $O^+(^4S) + H_2O$, the endothermic channel, which involves the production of $OH^+ + O + H$, is expected to be minor. The decrease in the OH^+ cross section at higher $E_{c.m.}$ (> 1.74 eV)[44] may be accounted for in part by the further dissociation of internally excited OH^+ into $O^+ + H$.

The OH^+ cross sections for $O^+(^2P) + H_2O$ are relatively high, reaching a value >30 $Å^2$ in the thermal energy range. We note that the production of $OH^+ + OH$ [reactions (10a-10d)] and that of $OH^+ + O + H$ [reaction (11)] from $O^+(^2P) + H_2O$ are both exothermic. The $E_{c.m.}$ dependencies for the OH^+ and H_2O^+ cross section from $O^+(^2P) + H_2O$ are similar, and characteristic of an exothermic process occurring via a long-lived complex mechanism. As pointed out above, the drop off in the OH^+ cross section at higher $E_{c.m.}$'s may be due in

Figure 2 Comparison of the cross sections for OH^+ from $O^+(^4S) + H_2O$ (solid circles), $O^+(^2D) + H_2O$ (solid squares), and $O^+(^2P) + H_2O$ (solid triangles) in the $E_{c.m.}$ range of 0.10-50 eV.

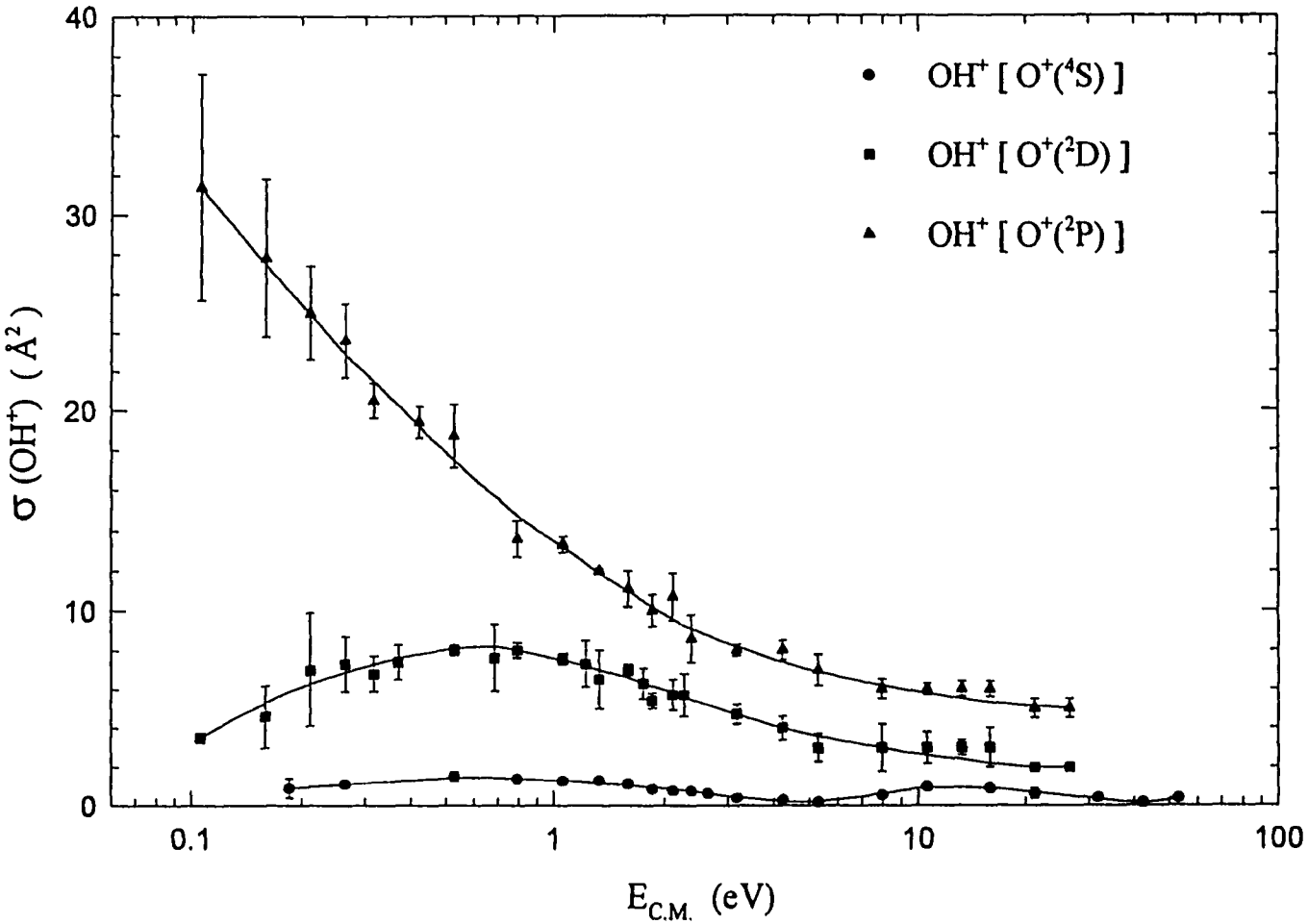
40
30
20
10
0
0.1
1
10
100
σ (OH+) (Å2)
EC.M. (eV)
OH+ [O+(4S)]
OH+ [O+(2D)]
OH+ [O+(2P)]

part to the further dissociation of the excited OH^+ product. We note that the exothermicity of reaction (10a), 4.91 eV, is only slightly lower than the O^+-H bond dissociation energy, 5.01 eV. The competition of the $OH^+ + OH$ product channel may also account for the low cross sections for H_2O^+ from $^+(^2P) + H_2O$.

C. Comparison of the sums of cross sections for H_2O^+ and OH^+ from $O^+(^4S,^2D,^2P)$

Figure 3 compares σ_T values for $O^+(^4S) + H_2O$ to those from $O^+(^2D) + H_2O$ and $O^+(^2P) + H_2O$ in the $E_{c.m.}$ range of 0.15-50 eV, where σ_T is the sum of the absolute cross sections for H_2O^+ and OH^+. The cross section data used for $O^+(^4S) + H_2O$ are from Ref. 19. As shown in the figure, the σ_T values for $O^+(^4S) + H_2O$ and $O^+(^2P) + H_2O$ are comparable. However, the σ_T values for $O^+(^2D) + H_2O$ are significantly higher than those for $O^+(^4S) + H_2O$ and $O^+(^2D) + H_2O$. The σ_T curve for $O^+(^2D) + H_2O$ exhibits a minor maximum at $E_{c.m.} \approx 4$ eV, similar to the H_2O^+ cross section curve.

As pointed out above, H_2O has a large dipole moment. The leading two terms of the long range potential for the O^+-H_2O system is

$$V(r) = -\alpha q^2/(2r^4) - (\mu q/r^2)\cos\theta, \qquad (12)$$

where α is the isotropic dipole polarizability of H_2O, q is the charge of O^+, and θ is the angle between the dipole axis and the line connecting the centers of gravity of the two colliding partners. The first term is the ion-induced dipole potential and the second term is the ion-dipole potential. The capture cross sections corresponding to the ion-induced dipole and ion-dipole potentials are $\pi q(2\alpha/E_{c.m.})^{1/2}$ and $\pi q(\mu/E_{c.m.})\cos\theta$, respectively.[1] For large impact parameter interactions, the ion-dipole potential dominates and the capture cross section is proportional to $1/E_{c.m.}$. This condition is expected at sufficiently low $E_{c.m.}$'s, where the ion-dipole interaction plays a dominant role in the formation of long-lived collision

Figure 3 Comparison of the sums [$\sigma_T = \sigma(H_2O^+ + OH^+)$] of cross sections for H_2O^+ and OH^+ from $O^+(^4S) + H_2O$ (solid circles), $O^+(^2D) + H_2O$ (solid squares), and $O^+(^2P) + H_2O$ (solid triangles) in the $E_{c.m.}$ range of 0.15-50 eV.

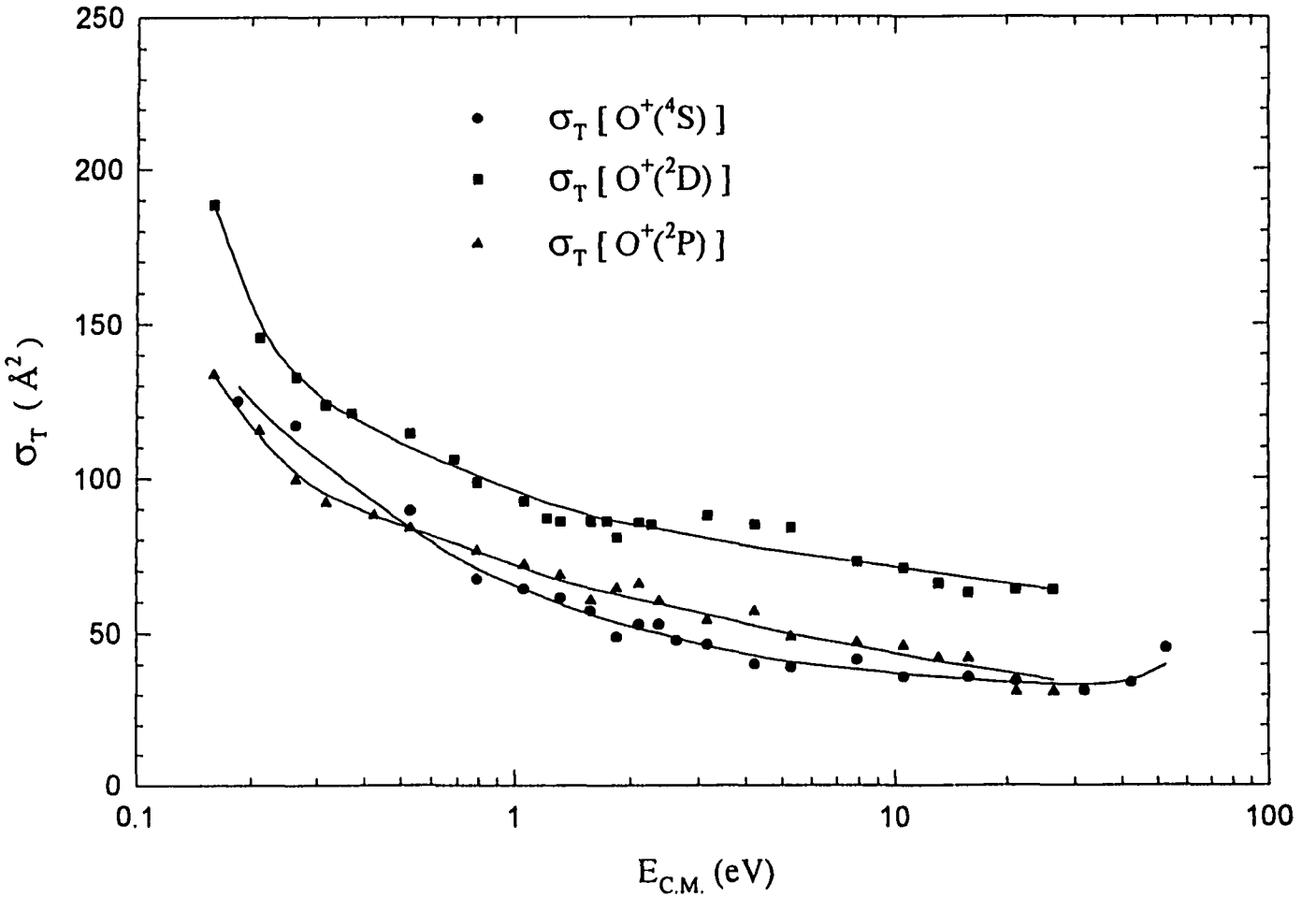
250
200
150
100
50
0
0.1
1
10
100
σ_T (Å^2)
$E_{C.M.}$ (eV)
σ_T [$O^+(^4S)$]
σ_T [$O^+(^2D)$]
σ_T [$O^+(^2P)$]

complexes and the dipole is oriented to maximize the ion-dipole interaction during the collision. Figure 4 compares the plots of σ_T versus $1/E_{c.m.}$ for $O^+(^4S) + H_2O$, $O^+(^2D) + H_2O$, and $O^+(^2P) + H_2O$ in the $E_{c.m.}$ range of 0.15-10 eV. The solid lines are the linear least square fits to the data sets. As shown in the figure, these data sets conform reasonably well with the linear fits after taking into account the experimental uncertainties. However, we note that the fits of cross section data at $E_{c.m.} > 1$ eV are likely fortuitous because the collision times at these $E_{c.m.}$'s are too short for the molecule to reorient during the collision.

IV. CONCLUSIONS

Applying the DCT-OIT technique for state-selection of $O^+(^2D)$ and $O^+(^2P)$ and the DRP scheme to improve the resolution for the reactant O^+ ion beam kinetic energy, we have measured the absolute cross sections for H_2O^+ and OH^+ from $O^+(^2D) + H_2O$ and $O^+(^2P) + H_2O$ in the $E_{c.m.}$ range of 0.10-30 eV. These cross sections are compared to those from $O^+(^4S) + H_2O$ measured recently in our laboratory. The charge transfer cross sections for $O^+(^2D) + H_2O$ are found to be significantly higher than those for $O^+(^4S) + H_2O$ and $O^+(^2P) + H_2O$. At $E_{c.m.} < 1$ eV, the lower charge transfer cross sections for $O^+(^2P) + H_2O$, compared to those for $O^+(^4S) + H_2O$, are attributed in part to the further dissociation of excited H_2O^+ ions and to the efficient competition of the exothermic product channel $OH^+ + OH$. The cross sections for OH^+ from $O^+(^2D) + H_2O$ and $O^+(^2P) + H_2O$ are found to be significantly greater than those from $O^+(^4S) + H_2O$. This observation is consistent with the exothermic nature of the product channels $OH^+ + OH$ and $OH^+ + O + H$ for the $O^+(^2D,^2P) + H_2O$ reactions.

The σ_T values for $O^+(^4S) + H_2O$, $O^+(^2D) + H_2O$ and $O^+(^2P) + H_2O$ are found to roughly conform with the $1/E_{c.m.}$ dependence at low $E_{c.m.}$'s, indicating that ion-dipole interactions plays an important role in the formation of the long-lived collision complexes.

The high cross sections observed for H_2O^+ and OH^+ from $O^+(^2D,^2P) + H_2O$ suggest

Figure 4 Plots of σ_T versus $1/E_{c.m.}$ in the $E_{c.m.}$ range of 0.15-10 eV. $O^+(^4S) + H_2O$: solid circles; $O^+(^2D) + H_2O$: solid squares; and $O^+(^2P) + H_2O$: solid triangles.

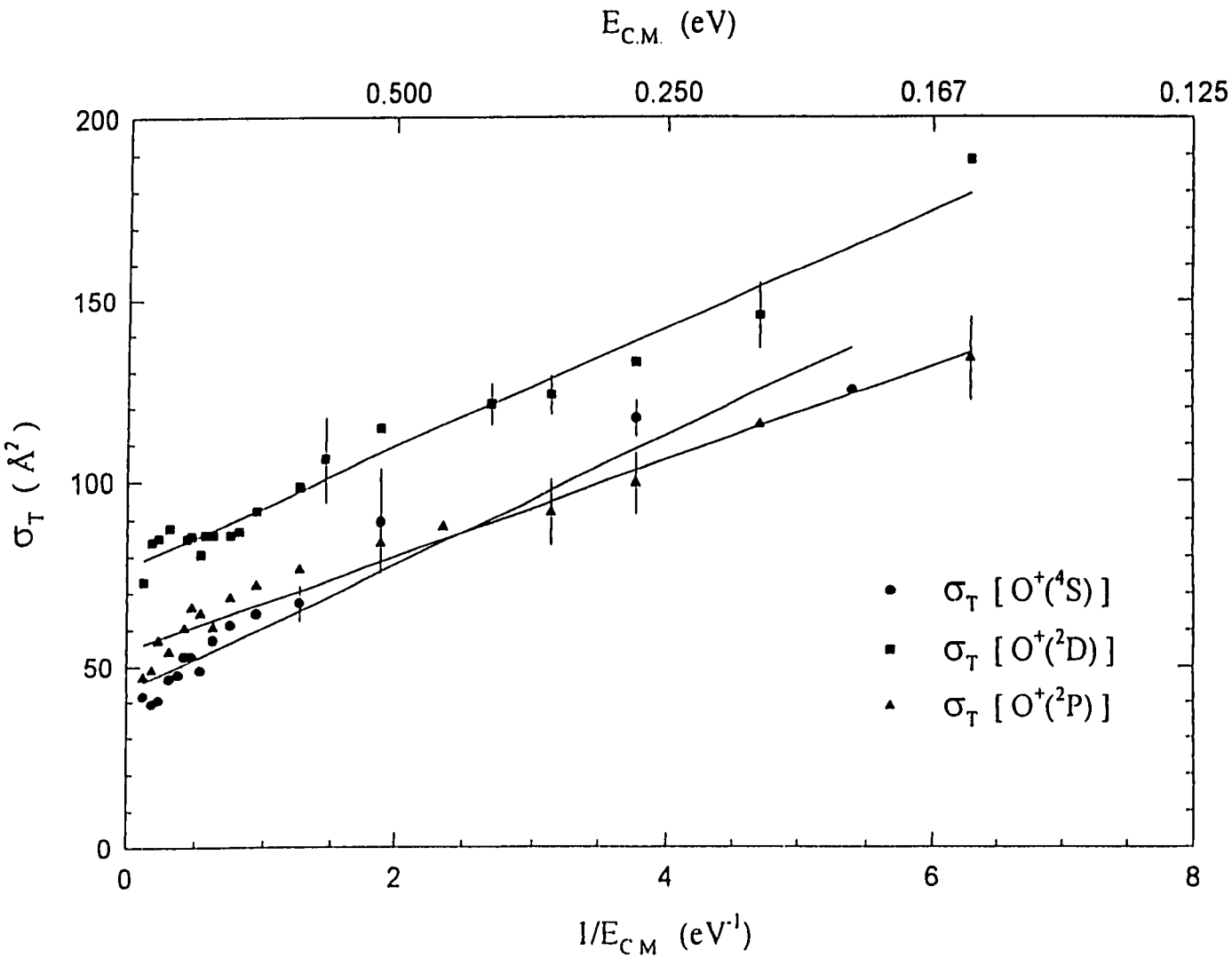
$E_{C.M.}$ (eV)
0.500
0.250
0.167
0.125
200
150
100
50
0
σ_T (A^2)
0
2
4
6
8
$1/E_{C.M.}$ (eV^{-1})
σ_T [$O^+(^4S)$]
σ_T [$O^+(^2D)$]
σ_T [$O^+(^2P)$]

that these reactions should be included in the modeling of the H_2O^+ and H_3O^+ ion density data measured in the vicinity of the space shuttle in the ionosphere. It is also our hope that the cross section data presented here will stimulate rigorous theoretical studies of the $[O+H_2O]^+$ ion-molecule reaction system.

Acknowledgements:

This work is supported by the National Science Foundation Grant Numbers: ATM-9200785 and ATM-9521558.

References

(1) R. A. Dressler and E. Murad, in "Unimolecular and Bimolecular Ion-Molecule Reaction Dynamics", edited by C. Y. Ng, T. Baer, and I. Powis, *Wiley Series in Ion Chem. & Phys.* (Wiley, Chichester, 1994), Chapter 2, p. 87.

(2) J. M. Grebowsky, H. A. Taylor, Jr., M. W. Pharo III, and N. Reese, *Planet. Space Sci.* **35**, 501 (1987); ibid. **35**, 1463 (1987).

(3) D. E. Hastings, N. A. Gatsonis, and T. Mogstad, *J. Geophys. Res.* **A93**, 1961 (1988).

(4) W. R. Paterson and L. A. Frank, *J. Geophys. Res.* **94**, 3721 (1989).

(5) R. S. Narcisi, E. Trzcinski, G. Federico, L. Wlodyka, and D. Delorey, *Proc. AIAA*, AIAA-83-2659, Washington, D. C. (Oct. 1983).

(6) M. R. Torr and D. G. Torr, *Rev. Geophys. Space Phys.* **20**, 91 (1982).

(7) A. Dalgarno and M. B. McElroy, *Planet. Space Sci.* **13**, 947 (1965).

(8) R. J. W. Henry, *Astrophys. J.* **161**, 1153 (1970).

(9) E. E. Ferguson, F. C. Fehsenfeld, and D. L. Albritton, in "Gas Phase Ion Chemistry", edited by M. T. Bowers (Academic, New York, 1979), Vol. 1, p.45.

(10) R. A. Dressler, J. A. Gardner, D. L. Cooke, and E. Murad, *J. Geophys. Res.* **96**, 13,795 (1991).

(11) E. Murad, Planet. Space Sci. **33**, 421 (1985).

(12) G. E. Caledonia, J. C. Person, and D. E. Hastings, *J. Geophys. Res.* **92**, 273 (1987).

(13) D. E. Hunton and J. M. Calo, *Planet. Space Sci.* **33**, 945 (1985).

(14) B. R. Turner and J. R. Rutherford, *J. Geophys. Res.* **21**, 6751 (1968).

(15) E. Murad and S. T. F. Lai, *Chem. Phys. Lett.* **126**, 427 (1986).

(16) M. Heninger, S. Fenistein, G. Mauclaire, R. Marx, and E. Murad, *Geophys. Res. Lett.* **16**, 139 (1989).

(17) R. A. Dressler, J. A. Gardner, R. H. Salter, F. J. Wodarczyk, and E. Murad, *J. Chem. Phys.* **92**, 1117 (1990).

(18) R. A. Dressler, R. H. Salter, and E. Murad, *Planet. Space Sci.* **40**, 1695 (1992).

(19) X. Li, Y.-L. Huang, G. D. Flesch, and C. Y. Ng, *J. Chem. Phys.* **102**, 5100 (1995).

(20) G. Gioumousis and D. P. Stevenson, *J. Chem. Phys.* **29**, 294 (1958).

(21) S. G. Lias, J. E. Bartmess, J. F. Liebman, J. L. Holmes, R. D. Levin and W. G. Mallard, *J. Phys. Chem. Ref. Data* **17**, suppl. 1 (1988).

(22) H. M. Rosenstock, K. Draxl, B. W. Steiner, and J. T. Herron, *J. Phys. Chem. Ref. Data* **6**, 1 (1977).

(23) J. L. Kohl, G. P. Lafyatis, H. P. Palenius, and W. H. Parkison, *Phys. Rev.* **A18**, 571 (1978).

(24) D. G. Torr and N. Orsini, *Planet. Space Sci.* **25**, 1171 (1977).

(25) D. G. Torr and N. Orsini, *Geophys. Res. Lett.* **5**, 657 (1978).

(26) M. R. Torr and D. G. Torr, *Geophys. Res. Lett.***7**, 103 (1980).

(27) X. Li, Y.-L. Huang, G.D. Flesch and C.Y. Ng, *Rev. Sci. Instrum.* **66**, 2871(1995)

(28) X. Li, Y.-L. Huang, G.D. Flesch and C.Y. Ng, *Rev. Sci. Instrum.* **65**, 3724(1994)

(29) X. Li, Y.-L. Huang, G.D. Flesch and C.Y. Ng, *J. Chem. Phys.*, submitted.

(30) X. Li, Y.-L. Huang, G.D. Flesch and C.Y. Ng, *J. Chem. Phys.*, submitted.

(31) G. D. Flesch, S. Nourbakhsh, and C. Y. Ng, *J. Chem. Phys.* **92**, 3590 (1990).

(32) G. D. Flesch and C. Y. Ng, *J. Chem. Phys.* **92**, 3235 (1990).

(33) G. D. Flesch and C. Y. Ng, *J. Chem. Phys.* **89**, 3381 (1988).

(34) G. D. Flesch and C. Y. Ng, *J. Chem. Phys.* **92**, 2876 (1990).

(35) N. R. Daly, *Rev. Sci. Instrum.* **31**, 264 (1960).

(36) G. O. Brink, *Rev. Sci. Instrum.* **37**, 857, 1626 (1966).

(37) G. Bischof and F. Linder, *Z. Phys. D.* **1**, 303(1986)

(38) D. Gerlich, *State-Selected and State-to-State Ion Molecule Reaction Dynamics I: Experiment*, edited by C.Y. Ng and M. Baer, pp.1-176, John Wiley, New York(1991); M. Scherbarth, Diplom thesis, University of Freiburg, 1988.

(39) These values correspond to Ne^+ formed in the $^2P_{1/2}$ spin-orbit excited state.

(40) G. D. Flesch, S. Nourbakhsh, and C. Y. Ng, *J. Chem. Phys.* **95**, 3381 (1991).

(41) G. D. Flesch, S. Nourbakhsh, and C. Y. Ng, *J. Chem. Phys.* **92**, 3590 (1990).

(42) C. Y. Ng, in "State-Selected and State-to-State Ion-Molecule Reaction Dynamics I: Experiment", edited by C. Y. Ng and M. Baer, p.401-500.

(43) K. P. Huber and G. Herzberg, "Molecular Spectra and Molecular Structure: Constants of Diatomic Molecules" (van Nostrand Reinhold, New York, 1979).

(44) K. Norwood, A. Ali, and C. Y. Ng, *J. Chem. Phys.* **95**, 8029 (1991) and references therein.

(45) Using the energetic information from Ref. 21, the dissociation energy for $OH^+ \rightarrow O^+ + H$ is calculated to be 4.95 eV.

GENERAL CONCLUSION

Using the unique triple-quadrupole double-octopole(TQDO) photoionization and electron-impact apparatus developed in our laboratory, the absolute state-selected cross sections for the ion-molecue reactions involving $O^+(^4S,^2D,^2P)$ and many neutral molecules of importance in the ionosphere such as N_2, H_2, D_2, and H_2O are measured over a collision energy range from near thermal energy to above 10eV. Good agreement with other people's results are found. A simple method to isolate $O^+(^2D)$ and $O^+(^2P)$ is developed. Because of the nature of the TQDO apparatus, the kinetic energy spread of the prepared ions is around 1eV, which is not good enough for the study of low-energy ion-molecule collision processes. A differential retarding potential method is developed for improving the kinetic energy resolution. With this method, the cross sections for reactions with collision energy below 0.1eV can be studied. Some interesting findings are observed resulting from applying these two methods. Some can be explained by simple scientific reasoning and theories. Others demand further investigation by both theoretical and experimental chemists. Further studies should help us understand more of the underlying laws and mechanisms of ion-molecule reactions.

APPENDIX

THE APPLICATION OF PC-BASED INSTRUMENTATION AND DATA ACQUISITION IN ION-MOLECULE REACTION RESEARCH

Abstract

In this paper, we outline some recent applications of PC-based instrumentation and data acquisition techniques to physical chemistry research. The programming language LabVIEW is briefly introduced and its applications are examined. The configuration of a timer and counter plug-in DAQ board for data acquisition and instrument control is explained. The coupling of an analog output plug-in DAQ board to the TQDO apparatus to control the voltages of the electrostatic lenses is illustrated in detail. And finally, some of the LabVIEW programs we developed on a Pentium computer for data acquisition and interfacing are explained. Their ease of coding and use is emphasized.

Introduction

In the last 50 years, instruments have seen fundamental changes fueled by the rapid advancement of general purpose technologies. This trend still continues, as the personal computer revolution changes the way instruments are built and used[1,2].

Over the years, instruments have evolved in both flexibility and the degree to which they are integrated into systems. The first generation of instruments were basically analog instruments manually controlled from the front panels[3,4]. In the context of electronics, these were stand-alone boxes that accepted input signals, performed a few designated functions, and then

displayed outputs that reflected some analysis or manipulation of the inputs. The users had little flexibility in interface design, measurement capabilities, or computational features.

With the advent of digital instruments[5,6] and the General Purpose Interface Bus(GPIB) standard[7], users now can control the instruments not only manually, but also programmatically. Each GPIB instrument is still a stand-alone instrument designed in the factory to perform a specific function. But with the added ability to communicate with a computer through the GPIB interface, a number of GPIB instruments could be "stacked" together to form a complete functional system under the control of a single computer. The computer controls the system by sequencing through pre-written commands acceptable by the target instrument to perform the complete set of measurement, analysis and presentation.

The implementation of computers into the world of instrumentation has generated an ever-more popular term "virtual instrumentation"[8]. A virtual instrument is a layer of software and/or hardware added to a general purpose computer in such a fashion that users can interact with the computer as though it were a custom-designed traditional electronic instrument. A virtual instrument user can use a wide variety of instrument hardware in a system, and can completely customize the instrument's functionality and user interface through high-level graphics-oriented application software. In a word, with a virtual instrument the user, rather than the vendor, defines the ultimate purpose of the instrument to exactly match the needs of the experiment.

Instruments today combine general-purpose computers with both traditional and new-generation instrument hardware. These modern instruments achieve new levels of flexibility and performance by combining the ever-increasing processing power and state-of-the-art

software of computers with new classes of instrument hardware.

The GPIB instruments and the later RS-232[9] (different communication standards from GPIB) instruments are the first type of virtual instruments. The communication between a GPIB or RS-232 instrument and its controlling computer is through a so-called message-based technique. The instrument does not operate at maximum performance since the instrument's internal processor must interpret the message command sent from the computer during the run time. Besides, the user can only work within the confinement of the vendor-defined, built-in functions of the instrument. One has to seek another instrument if the current one does not perform the desired functions. These are limitations of GPIB or RS-232 instruments.

In response to this situation, the second phase of virtual instrumentation has been the emergence of two new approaches to instrument hardware: (1) plug-in data acquisition (DAQ) boards[10], and (2) VXIbus[11] instrument-on-a-card standard. In this phase, register-based communication is the main technique. Another feature of this phase of virtual instrumentation is that the instrument no longer has a physical front panel because control of the instrument resides in the computer. The plug-in DAQ boards install into the expansion slots of desktop computers and thus attach directly to the parallel bus of the processor itself. Its onboard registers are mapped into the memory address space of the computer. The computer, therefore, can perform binary control of the plug-in board at very high speeds, just as inside a traditional instrument. Direct hardware interrupts notify the processor of status and the need for service, and cause the processor to branch immediately to execute the appropriate machine code to handle the interrupts. Data can be transferred to/from the board

in binary form, in parallel, and at very high speeds. The transfer can be performed not only by the processor itself, but also by dedicated direct-memory-access hardware also built into the PC. As evidence of the flexibility and cost-effectiveness of this approach, Figure 1 shows the trend of this second particular phase of virtual instrumentation. This phase has opened the architecture of instruments.

The third phase of virtual instrumentation has been in object-oriented software technology[12]. Now that instrument users build a virtual instrument front panel and communicate with and control the instrument through a computer, software technology has become the key. Recent development in programming language has been the revolutionary transition from structure-oriented programming[13] to object-oriented programming. Object-oriented software makes it easier for the virtual instrument user to build a single, unified, user-friendly environment. A variety of object-oriented programming languages have emerged in the past few years. Among them, LabWindows and LabVIEW from National Instrument are the object-oriented software development frameworks that are designed specifically for building virtual instruments with a computer. We found them easy to learn and to use.

In this report, we discuss the construction of some virtual instruments using two plug-in DAQ boards and the graphical programming language LabVIEW on a Pentium PC, and their applications in the TQDO apparatus in our laboratory.

The Construction of Virtual Instruments With the TQDO Apparatus

1. Equipment Requirements

The triple quadrupole-double octopole(TQDO) apparatus[14,15] is used to measure absolute cross sections for ion-molecule reactions. The principles and procedures for absolute cross section measurements using the TQDO apparatus have been described in detail previously[16-21]. Nevertheless, the schematic diagram for the TQDO apparatus is shown in Figure 1 for readers' convenience. The TQDO apparatus essentially consists of, in sequential order, a VUV photonionization ion source or an electron impact ionization ion source(1), a reactant quadrupole mass spectrometer(QMS) (3), a lower radio frequency(RF) octopole ion guide reaction gas cell(RFOIGGC) [(4)+(5)], a middle QMS(6), an upper RFOIGGC [(7)+(8)], a product QMS(9), and a Daly-type scintillation ion detector [(10)+(11)+(12)].

The VUV photonionization device consists of a discharge lamp, a 0.2m VUV monochromator (McPherson 234), and a tungsten photoelectric VUV light detector. The grating of the VUV monochromator is driven by a stepping motor. The rotation of the stepping motor depends on the number of TTL(Transistor-Transistor Logic. Signal logical 0=0.0 to 0.8V and logical 1=2.0 to 5.0 V) pulses received by the motor. The direction of a particular rotation depends on the logical state of the control input. Both the TTL pulses and control input can be generated by a TTL pulse generator, which is exactly what an old home-built microprocessor does. A new way to generate TTL pulses is to use a plug-in Timer and Counter DAQ board. We will show later how this is done.

As shown in Figure 1, the ions produced in the ionization region are first pulled or

Figure 1 Schematic of the tandem mass spectrometer arrangement for absolute total cross section measurements. (1) electron impact ionization ion source, (2) nozzle, (3) reactant QMS, (4) lower RF octopole ion guide, (5) lower RFOIGGC, (6) middle QMS, (7) upper RF octopole ion guide, (8) upper RFOIGGC, (9) product QMS, (10) scintillator, (11) photo multiplier tube, (12) aluminum ion target. Note that the Daly-type scintillation detector consists of items (10), (11), and (12). The intermediate aperture lenses *a*, *b*, *c*, and *d* have the same aperture size (0.89 cm in diameter and 0.14 cm in thickness).

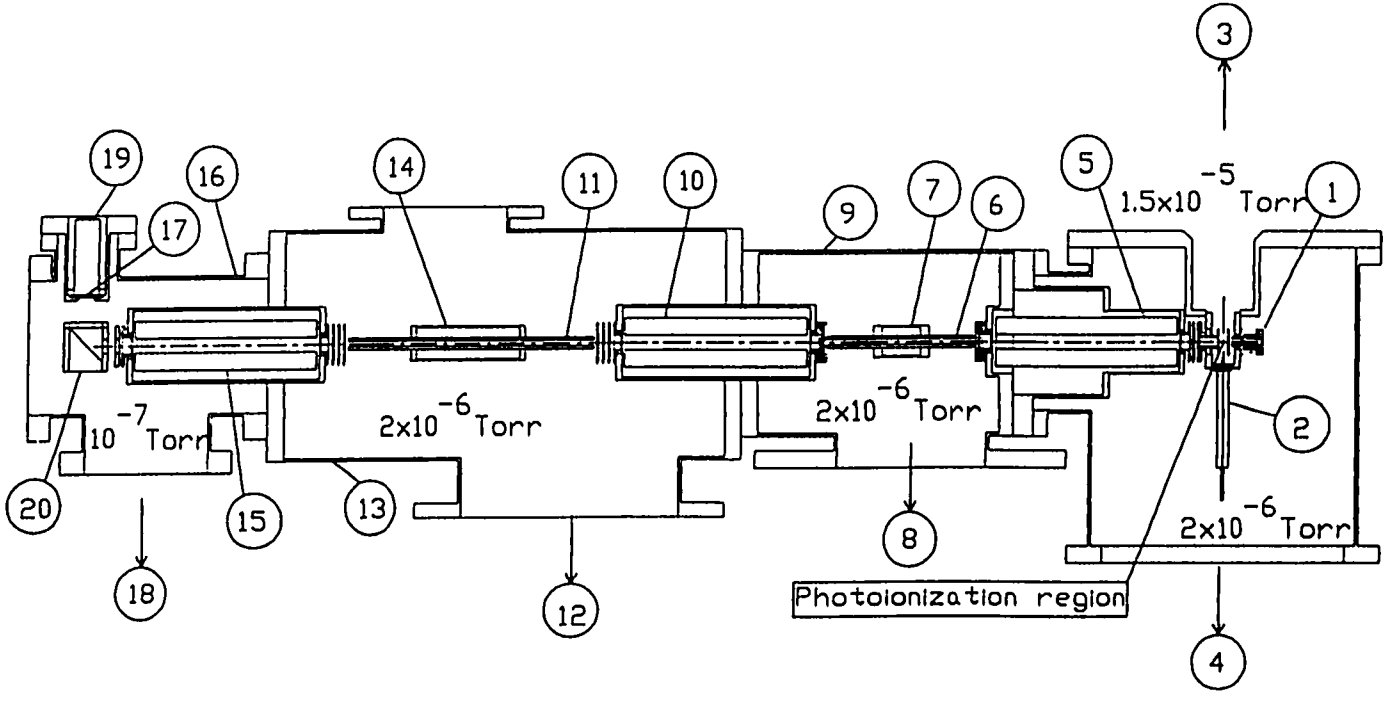
3
19
16
14
11
10
9
7
6
5
1.5x10 -5 Torr
1
17
10 -7 Torr
2x10 -6 Torr
2x10 -6 Torr
2
20
15
13
8
2x10 -6 Torr
18
12
Photoionization region
4

pushed out the ionization region by extracting or repelling electrostatic lenses. There are many electrostatic lenses along the ion path for guiding and focussing the ions. These lenses have a voltage sweep of -300 to +300V. Practically, voltages of the majority of the lenses are between -50 and +50V. The voltages of these lenses are supplied from potentiometers driven by two power supplies, one supplying +300V and the other supplying -300V. The lens voltages are individually adjusted to maximize ion transmission. From the first two sections of this thesis, we know that the lens settings are crucial in ion beam focussing, kinetic energy variation and mass selection resolution. Because of this and the manual fine-tuning process, tuning the electrostatic lenses is usually the most time consuming procedure in the measurement of absolute cross sections vs. collision energies. In applying the differential retarding potential method[22] to obtain low-collision energy results, the situation becomes even more tedious because the operator must change the voltages of certain lenses repeatedly during the data acquisition process. Furthermore, this kind of study demands accuracy and stability of the whole system over a substantial period of time. Manually changing the voltages during run-time not only results in re-setting inaccuracy but also takes more time. This motivated us to use the computer to automatically configure and update the voltages of the lens system as needed. A plug-in analog output DAQ board is the first step towards this end.

The three quadrupole mass spectrometers in the TQDO apparatus are operated from three Extranuclear Laboratories quadrupole controls. These three EL quadrupole controls accept analog voltage inputs for mass selection and sweeping. The analog voltage inputs had been generated by D/A converters in a home-built microprocessor unit. A simple plug-in

analog DAQ board can be configured to do the same thing.

Overall, we find that at the current stage only two plug-in DAQ boards are required. One generates analog voltage outputs (National Instrument AT-AO-10) and the other generates TTL pulses (National Instrument PC-TIO-10). LabVIEW has been selected for the software environment in which to develop the virtual instruments because of its ease of use and graphical nature. In the paragraphs below, we discuss some of the hardware and software issues that we encountered in constructing our virtual instruments.

2. Coupling The Analog Outputs to The Lens System and The Mass Spectrometers

The AT-AO-10 is a high-performance analog output and digital I/O board for the PC. It has ten double-buffered, multiplying, 12-bit digital-to-analog converters(DAC) and thus has ten independent output channels. The board can be configured to output either unipolar or bipolar voltages. The user has a choice of using either an onboard DAC reference voltage of 10V or an external reference voltage between -10V and +10V. For the timing purposes, this board has an onboard timer/counter interfaced to the National Instruments RTSI bus. Using this bus, National Instruments AT series boards can send timing signals to each other. The AT-AO-10 is ideal for applications such as automation and process control, instrumentation, and electronic test signal generation. The analog voltage outputs can be used for functions such as 12-bit resolution voltage sourcing, analog function generation, and control signal output.

Unfortunately, the output voltage is limited to -20V to +20V. Compared to the much larger voltage range of -300V to +300V needed for the electrostatic lens system, a single AT-AO-10 board insufficient voltage range to be a completely computer controlled voltage

setting system. However, in examining the differential retarding potential method used in low-energy cross section measurement, we find that the voltage variation required for the related lenses (including the intermediate lenses a+b, and the upper RFOIGGC, see Figure 1.) is actually within 0V to 10V. As a first step towards total automatic control, we can add the voltage outputs of 0V to 10V from the AT-AO-10 to the manually tuned voltages obtained at the potentiometers of some selected electrostatic lenses. For example, if the desired voltage of lenses a+b (electrically connected to form a thick retarding lens in order to remove the slower ions more efficiently) is in the range of 10V to 20V, we first manually set the output voltage of the potentiometer to 10V and then use the computer to programmatically adjust the analog voltage output from the AT-AO-10 between 0V and 10V. The summation of these voltages gives a variable range of 10V to 20V. The realization of this coupling is illustrated in Figure 2. In this schematic diagram, the normally grounded end of the potentiometer is connected to a 5V relay-driven switch. When the switch is off, the low voltage end of the potentiometer is grounded, giving the same configuration as before. When the switch is on, the low voltage end of the potentiometer is connected to a particular output channel of the AT-AO-10. Thus the output voltage obtained from the wiper of the potentiometer is changed by changing the output voltage from the computer board. This gives us computer control over the lens system setting. The differential retarding potential method can now be carried out automatically by the computer during run-time. The encouraging prospectives in this first stage of PC-based instrumentation certainly gives us more confidence in developing future project.

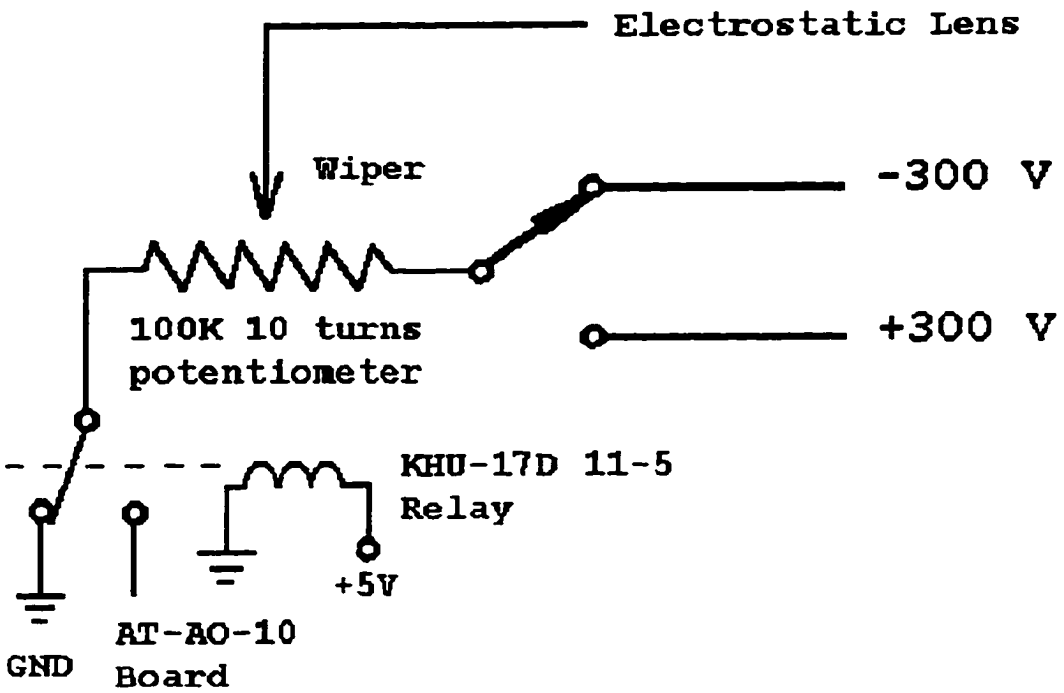

Figure 2 Schematic of the potentiometer coupled with the analog output from a DAQ board.

The quadrupole mass spectrometer is easier to control by the computer since the quadrupole control accept analog voltage inputs for mass selection and mass scanning. The input range is from 0V to 10V, within the range of the AT-AO-10 board. Therefore we can directly connect the output channels on the AT-AO-10 board to the quadrupole control without any conditioning. The resolution of each analog output channel is 12-bit (0.0024V). For a 0V to 10V sweeping range corresponding to a mass range of 0 to 100, which is usually the mass range of interest, a Δm as small as 0.025 is obtained. This exceeds the mass resolution of the spectrometer itself. To summarize, we have set aside five channels on the AT-AO-10 DAQ board for automatic control of the electrostatic lens system, three channels for computer-controlled mass selection and mass sweeping, and two channels for spares.

3. *Configuration of the PC-TIO-10 board*

The PC-TIO-10 plug-in DAQ board is a 10-channel timing and digital I/O interface for the PC. It can perform a wide range of pulse measurement, pulse generation and wave generation functions. The heart of the board is two Advanced Micro Devices (AMD) Am 9513A System Timing Controller (STC) chips, each of which has five independent 16-bit counters and a 4-bit programmable frequency output, FOUT. Each of the STCs connects to an onboard 1MHz frequency source, giving internal frequencies as follows:

- 1-MHz clock(1-μs resolution)
- 100-kHz clock(10-μs resolution)
- 10-kHz clock(100-μs resolution)
- 1-kHz clock(1-ms resolution)
- 100-Hz clock(10-ms resolution)

- 5-MHz clock(200-ns resolution, counters 5 and 10 only, from an onboard 5-MHz timebase)

These frequencies can be programmably selected for different resolution requirements. Each counter of the PC-TIO-10 has a SOURCE input, a GATE input, and an OUT input (See Figure 3).

The SOURCE input is used for counting operations. The signals that come in through the SOURCE input pin on the counter must be TTL signals. The GATE input is also used

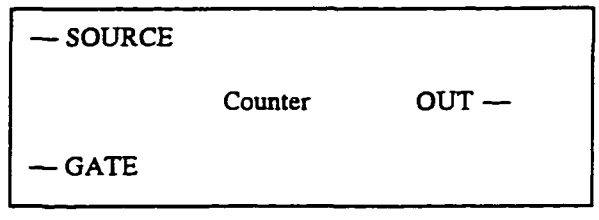

Figure 3 Counter Block Diagram

for counting operations. The user configures the counter for an operation through the software so that a signal at the GATE input starts or stops the counter operation. The counter can generate timing TTL signals at its OUT output. The TTL output can be a single delayed pulse or a pulse train, and it can also be gated externally at the GATE input.

Many different operations are possible with several counters working together through the software. With appropriate software, the user can configure the PC-TIO-10 board to count events or time, to measure frequency, to measure pulse width or period, and to

generate a delayed pulse or a pulse train. Later we will show how a lock-in counting system is constructed with several counters.

The first use of the PC-TIO-10 board, besides events counting, is to control a stepping-motor for the monochromator. The arrangement is illustrated in Figure 4. Here we use counters 6 and 10 to control the stepping-motor. Counter 10 generates a delayed pulse for two purposes: (1) to serve as a gating signal for counter 6, and (2) to serve as the direction signal for the stepping-motor drive. Counter 6 generates a pulse train at a user-specified rate during the gating period (given by the width of the gating pulse received from counter 10). The stepping motor rotates forward or backward, depending on whether the direction signal is logical high or logical low. This rotation changes the monochromator wavelength 1Å for every 8 TTL pulses, with no regard to the frequency or the width of the pulses. With this in mind, the operator then selects a certain frequency for the pulse train and calculates the time needed to generate the desired number of pulses. This time is the width required for the direction pulse. In this way, counter 6 only generates pulses during the period of the direction signal, ensuring that the stepping-motor rotates in the right direction for the desired distance. The PC-TIO-10 is also used in a very important lock-in counting technique used in pulsed molecular beam studies. Figure 5 shows the TOF profile of $C_2H_4^+$ after pulsed C_2H_4 neutral is intersected by an O^+ beam without differential pumping. Shown are two pulses separated by 0.5 second. We are interested in counting the peak area (first 20ms period after the pulse valve is activated for 10ms) and the tail area (last 20ms period before next pulse valve activation) of each pulse. We want to do the same thing for each pulse and accumulate the peak counts and the tail counts. Then we can subtract the

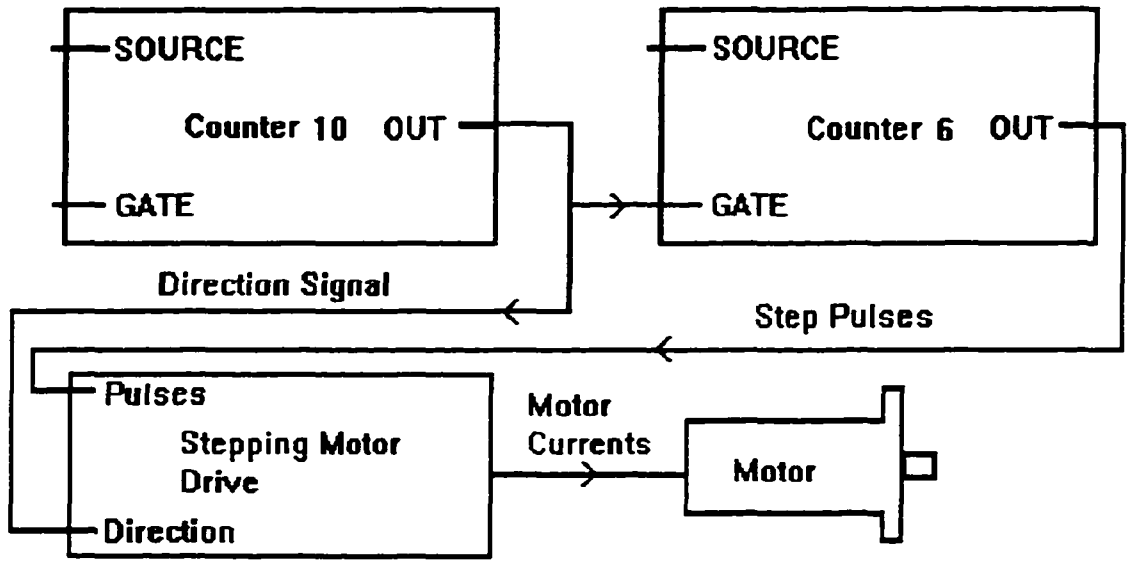

Figure 4. Block Diagram of the Stepping-Motor System

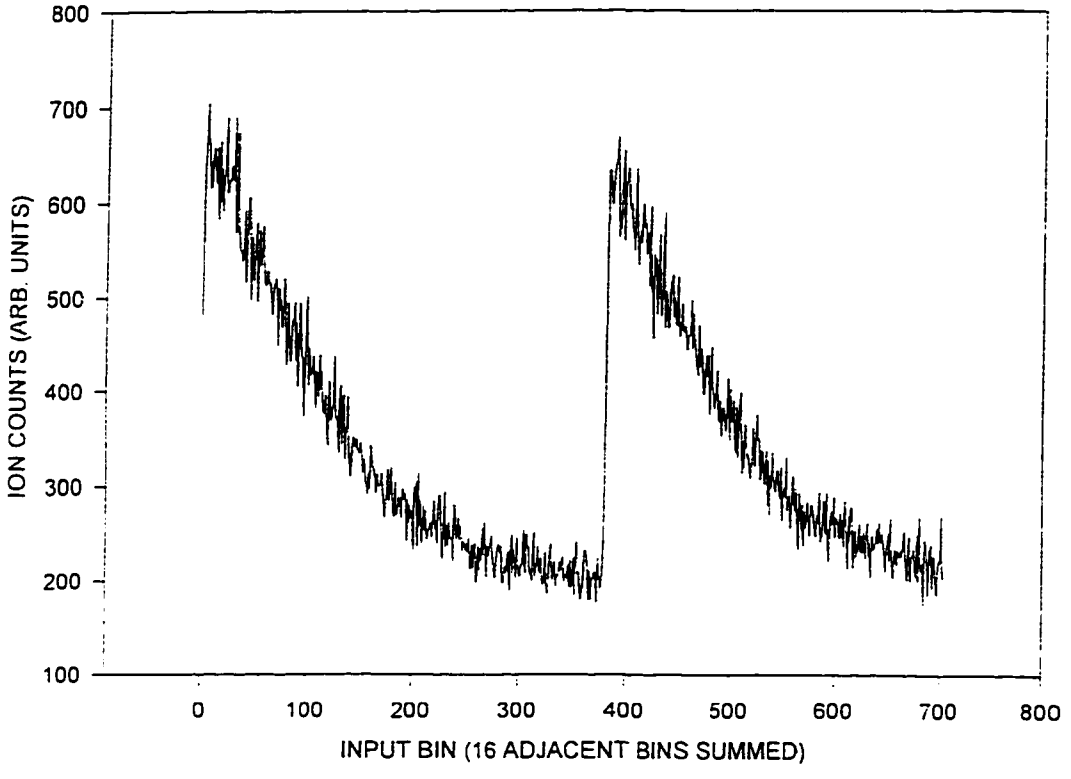

Figure 5 TOF profile of $C_2H_4^+$ after reaction $O^+ + C_2H_4$.

final tail count, which is essentially the background, from the final peak count to obtain the background-corrected ion count. This technique requires one counter for the peak area and one for the tail area. They must be configured so that during the full period of the gas pulse, they only count during the desired portions of each pulse and ignore all other portions of the pulse. Schematic block diagrams in Figure 6 and the pulse trains in Figure 7 show how this is accomplished.

Physical connections of the involved counters are shown in Fig. 6. Here, Counter 5 generates gating signals on its OUT pin for Counter 7. Counter 7 in turn generates gating signals simultaneously for the Pulse Valve Control and Counters 8 and 9. Counter 8 then generates gating signals for Counter 1 & 2, which are internally concatenated to make a larger counter (32-bit), used to count the peak area of the ion pulse. Counters 9 and 3 & 4 are connected similarly to count the tail area.

The pulse trains coming out of Counters 5, 7, 8, 9 are shown in Fig. 7. Here Counter 5 defines the counting period, in this case 10 seconds. Counter 5 generates a delayed pulse(could be minimally delayed) with a logical high width of 10 sec. This pulse serves as a level gate under which Counter 7 generates a pulse train according to user- selected specifications. The pulse has a repetition period of 0.5 second and width of 1 ms. Thus Counter 7 generates a total of 20 pulses during the 10-second period. These pulses go to the Pulse Valve Control to open the pulse valve 20 times for 1ms each, thus generating 20 ion pulses. The pulses from Counter 7 are simultaneously sent to Counters 8 and 9 for rising-edge gating. Counter 8 is configured to generate a 20ms pulse 10 ms after the rising edge of each pulse from Counter 7. These pulses form a train which in turn goes to Counter 1 &

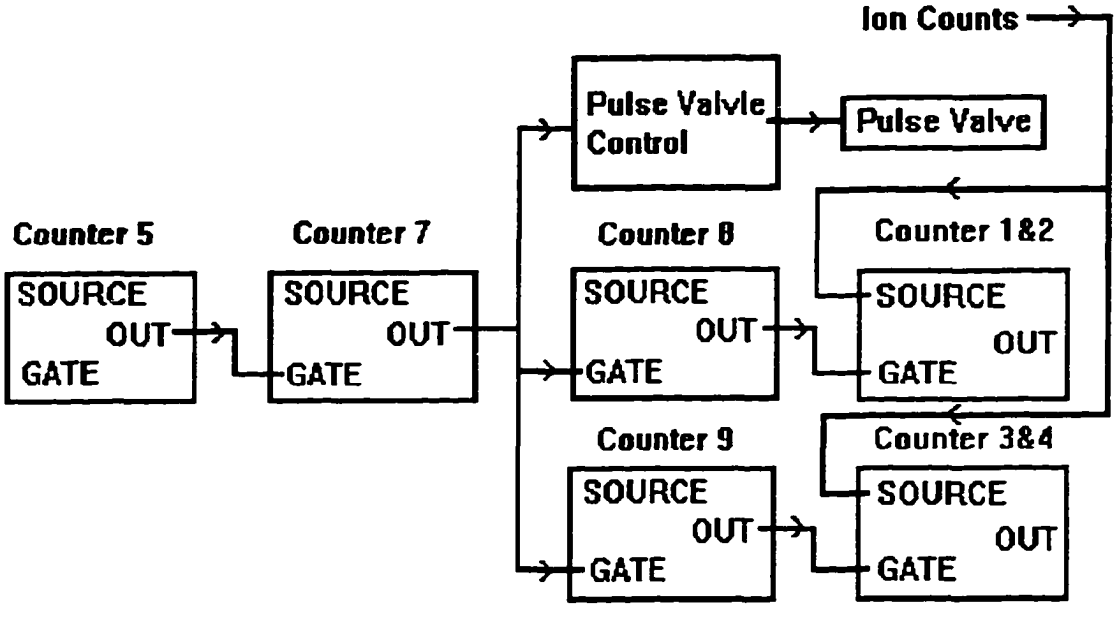

Figure 6 Block diagram of the counter lock-in technique.

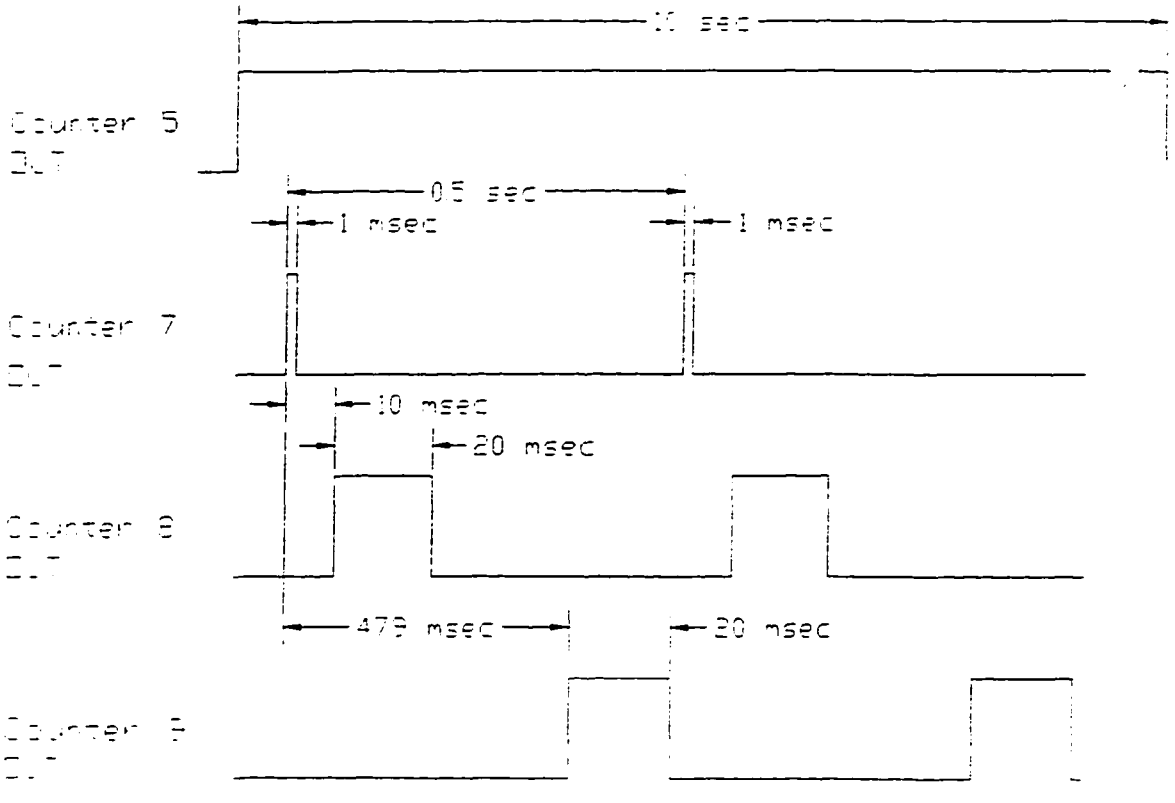

Figure 7 Pulse trains generated by the Timer and Counter Board

2 for level gating. That is, Counter 1 & 2 only counts when the gating pulses from Counter 8 are logical high. In this way, Counter 1 & 2 locks into the first 20 ms period that is 10 ms after each ion pulse, which is the peak area. Counter 9 and Counter 3 & 4 work the same way, except that the delay time for Counter 9 is 479 ms, so that Counter 3 & 4 locks into the tail area of each ion pulse.

4. Some Examples of The Virtual Instruments

The software we used to construct virtual instruments is LabVIEW from National Instrument. LabVIEW provides an object-oriented graphical programming environment. It uses a "virtual instrument" metaphor to build and package software into reusable virtual instrument modules. Each module consists of a graphical front panel (resembling the physical front panel of a real instrument), through which interactive control of the virtual instrument is conducted, a block diagram program to define its functionality, and an icon that makes the virtual instrument re-usable in the block diagram program of higher-level virtual instruments.

Shown in Figure 8 is the front panel of a module that sets the wavelength of the monochromator and scans the desired spectrum. The front panel has a graph display, several indicators and controls. The user can set the starting wavelength (Starting WL), the final wavelength (Destination WL), the step, and the time spent on each step (Time Constants), just as if setting the initial conditions on a real instrument. During run time, the panel shows the photon counts/sec, ion counts/sec, and the current wavelength of the monochromator. At the end of the scan, the spectra for ions and photons are plotted on the graph.

The underlying "circuitry" of the front panel is shown in Figure 9. This is the block diagram program of the module through which the functions of the module are carried out.

The LabVIEW block diagram methodology is based on the concept of data-flow programming. Data-flow programming dictates that an object may not execute until all of its inputs are available and may not output data until the object's function is completed. Thus, the flow of data between connected objects controls the order of execution. The beauty of data-flow programming is that the execution order is not constrained to the sequential order of lines from a text-based program. Free from the constraints of text-based programs, the user can quickly develop applications simply by connecting functional blocks. Multiple data paths are allowed, and hence simultaneous operations. As in traditional, text-based programming languages, LabVIEW contains structures that control the block diagram function execution, for instance, Sequence, Case statement, For Loop and While Loop. These structures are graphically depicted as border structures. There are a Case statement structure and a For Loop structure in Fig. 9. Every icon on the block diagram is an object with inputs and outputs. Even the whole module (called "VI" for virtual instrument) itself can be made into an object and represented by an icon (it becomes a "SUB-VI") in a higher-level module. For example, the "STEP MOTOR DRIVER" icon inside the For Loop is itself a driver module used to rotate the stepping motor. In the block diagram it is an object just like any other object that takes input(s), performs a few functions on the input(s), and sends the output(s) to the next object(s). The packaged SUB-VI can also be used in any other VIs that demand the same function(s) for the stepping motor, giving rise to the object's re-usability. As a matter of fact, this is the essence of developing virtual instruments. The programmer first breaks down a whole operation into many smaller, repetitive tasks, then develops sub-modules to perform these tasks. Finally the sub-modules are assembled to form

Figure 8 The front panel of a VI that sets the wavelength of the monochromator and scans across the desired spectrum.

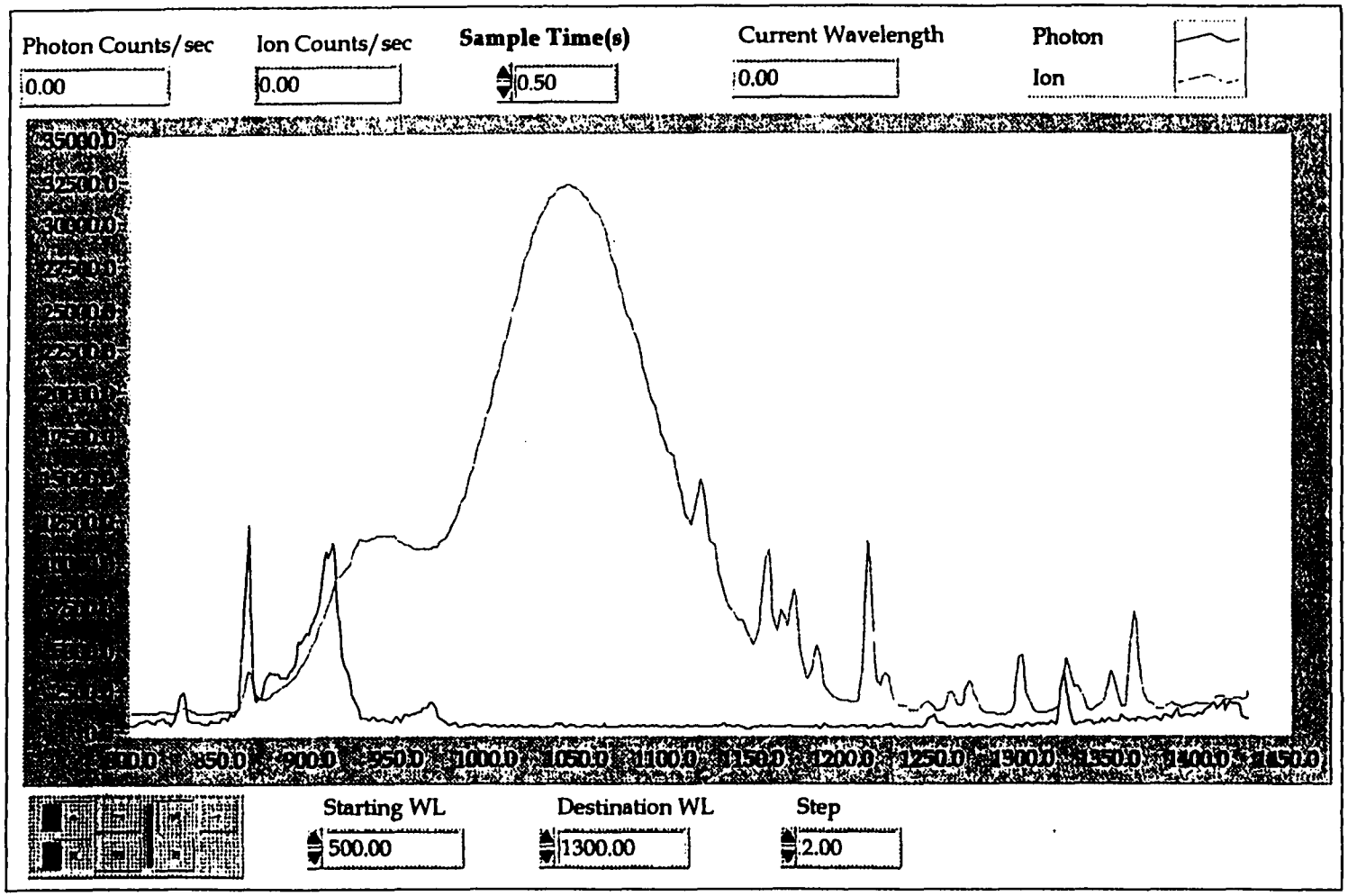
Photon Counts/sec
0.00
Ion Counts/sec
0.00
Sample Time(s)
0.50
Current Wavelength
0.00
Photon
Ion
35000.0
32500.0
850.0
900.0
950.0
1000.0
1050.0
1100.0
1150.0
1200.0
1250.0
1300.0
1350.0
1400.0
1450.0
Starting WL
500.00
Destination WL
1300.00
Step
2.00

Figure 9 The block diagram program of the same VI whose front panel is shown in Fig. 8

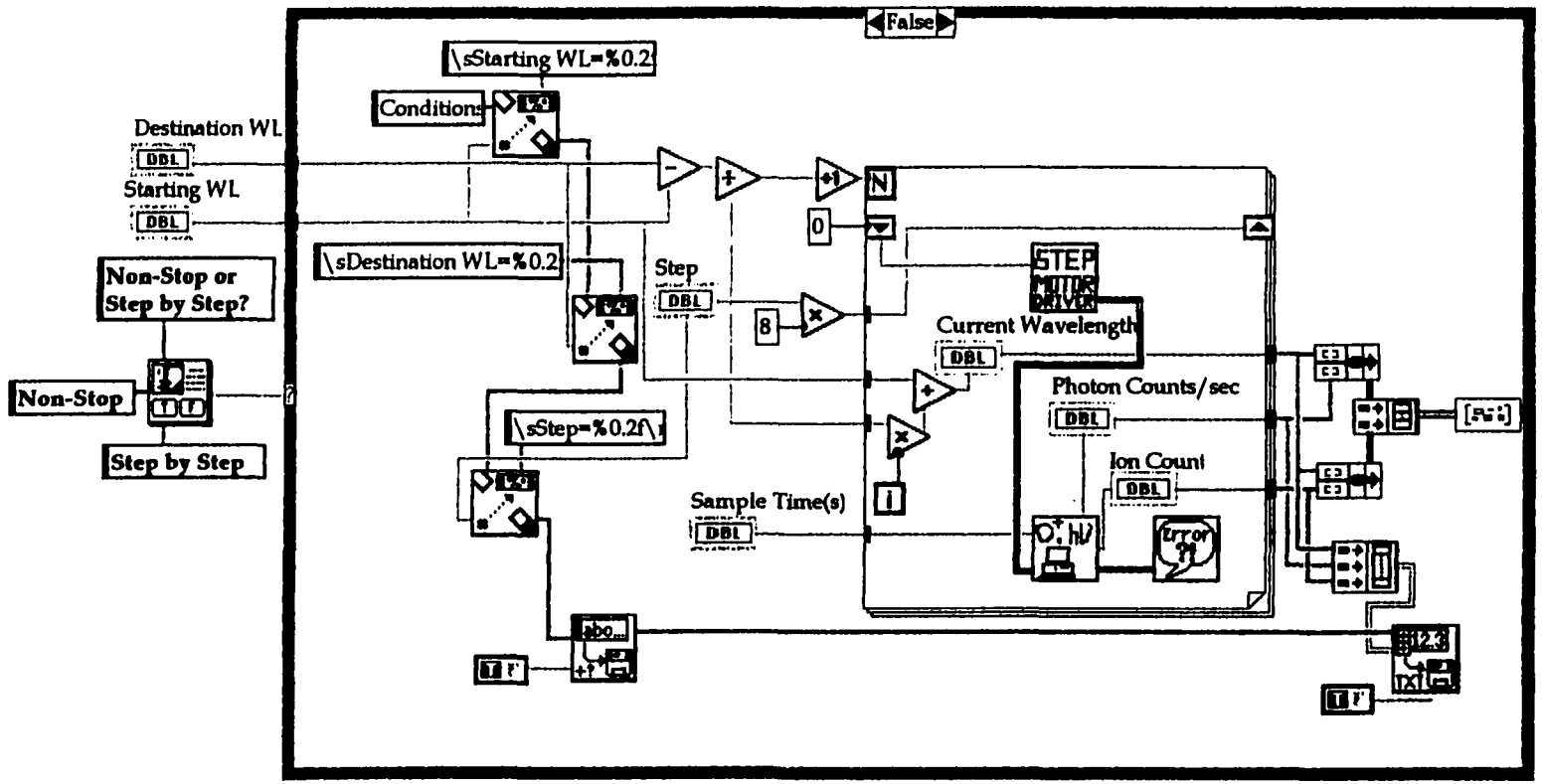
False
\sStarting WL=%0.2
Conditions
Destination WL
DBL
Starting WL
DBL
Non-Stop or Step by Step?
Non-Stop
Step by Step
\sDestination WL=%0.2
Step
DBL
8
0
N
STEP MOTOR DRIVER
Current Wavelength
DBL
Photon Counts/sec
DBL
Ion Count
DBL
\sStep=%0.2f\
Sample Time(s)
DBL
error
abc
TF
123
TF

a master module for the whole operation.

The differential retarding potential method discussed in section I can be conveniently run by the computer with the virtual instrument shown in Figures 10 and 11. The front panel in Fig. 10 contains controls, indicators and a graph display. The graph is used to display the O^+ counts as the voltages of the intermediate lens and the upper RFOIGGC are changed. Lens #21 is the intermediate lens varied to retard the slow O^+ ions. The "Voltage for #21 control demands at least two voltage values for lens #21, with the higher voltage removing more O^+ ions. The "UGC Voltage Array" requires an array of upper RFOIGGC voltages to generate potential retarding data. "Time constants" is the time spent counting each reactant and product ion for each #21 and upper RFOIGGC voltage setting.

The most significant feature of the block diagram in Fig. 11 is the nested structures. There is an outside For loop that steps through the voltage values stored in the "UGC Voltage Array". Nested inside this For loop is another For loop that picks the voltage values in "Voltage for #21 High and Low" one at a time. Inside the second For loop is a While loop whose main function is to check the data to see if repetition is needed in case the apparatus is unstable. Inside this While loop is another For loop that steps through all the masses of interest. Also inside the While loop is a Case loop that works together with the While loop to check data validity. The main functions of this virtual instrument are inside of the While loop. The "set and count pulse(ei-pv).vi" sub-vi uses all the pre-set conditions to control the AT-AO-10 DAQ board to provide the desired voltages to selected electrostatic lenses for voltage variation and to the quadrupole controls for mass selection. Each ion of

Figure 10 Front panel of the Retarding Differential Method(EI-PV).vi

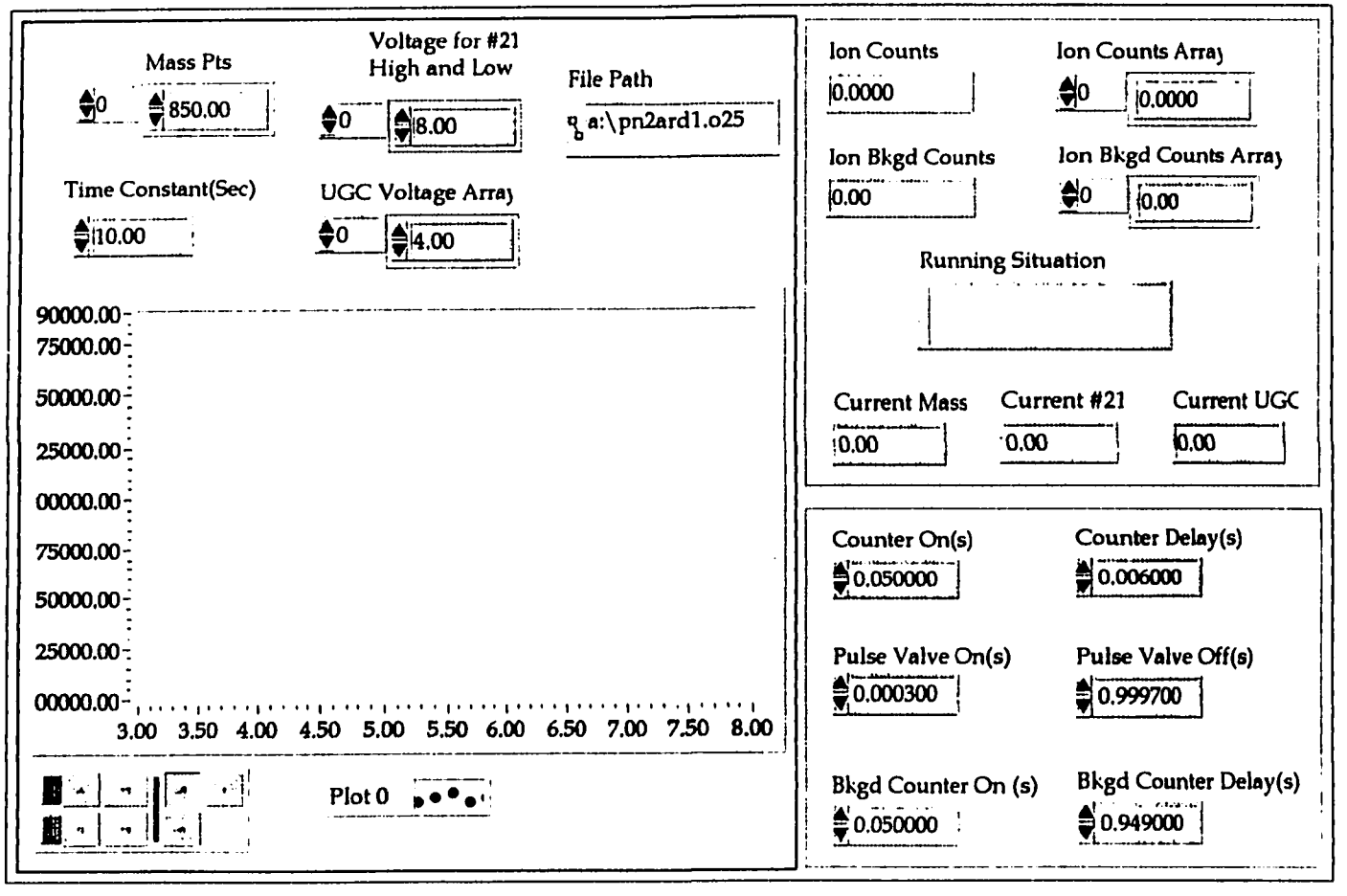
Mass Pts
0
850.00
Voltage for #21
High and Low
0
8.00
File Path
a:\pn2ard1.o25
Time Constant(Sec)
10.00
UGC Voltage Array
0
4.00
90000.00
75000.00
50000.00
25000.00
00000.00
75000.00
50000.00
25000.00
00000.00
3.00 3.50 4.00 4.50 5.00 5.50 6.00 6.50 7.00 7.50 8.00
Plot 0
Ion Counts
0.0000
Ion Counts Array
0
0.0000
Ion Bkgd Counts
0.00
Ion Bkgd Counts Array
0
0.00
Running Situation
Current Mass
0.00
Current #21
0.00
Current UGC
0.00
Counter On(s)
0.050000
Counter Delay(s)
0.006000
Pulse Valve On(s)
0.000300
Pulse Valve Off(s)
0.999700
Bkgd Counter On (s)
0.050000
Bkgd Counter Delay(s)
0.949000

Figure 11 Block diagram of the Retarding Differential Method(EI-PV).vi

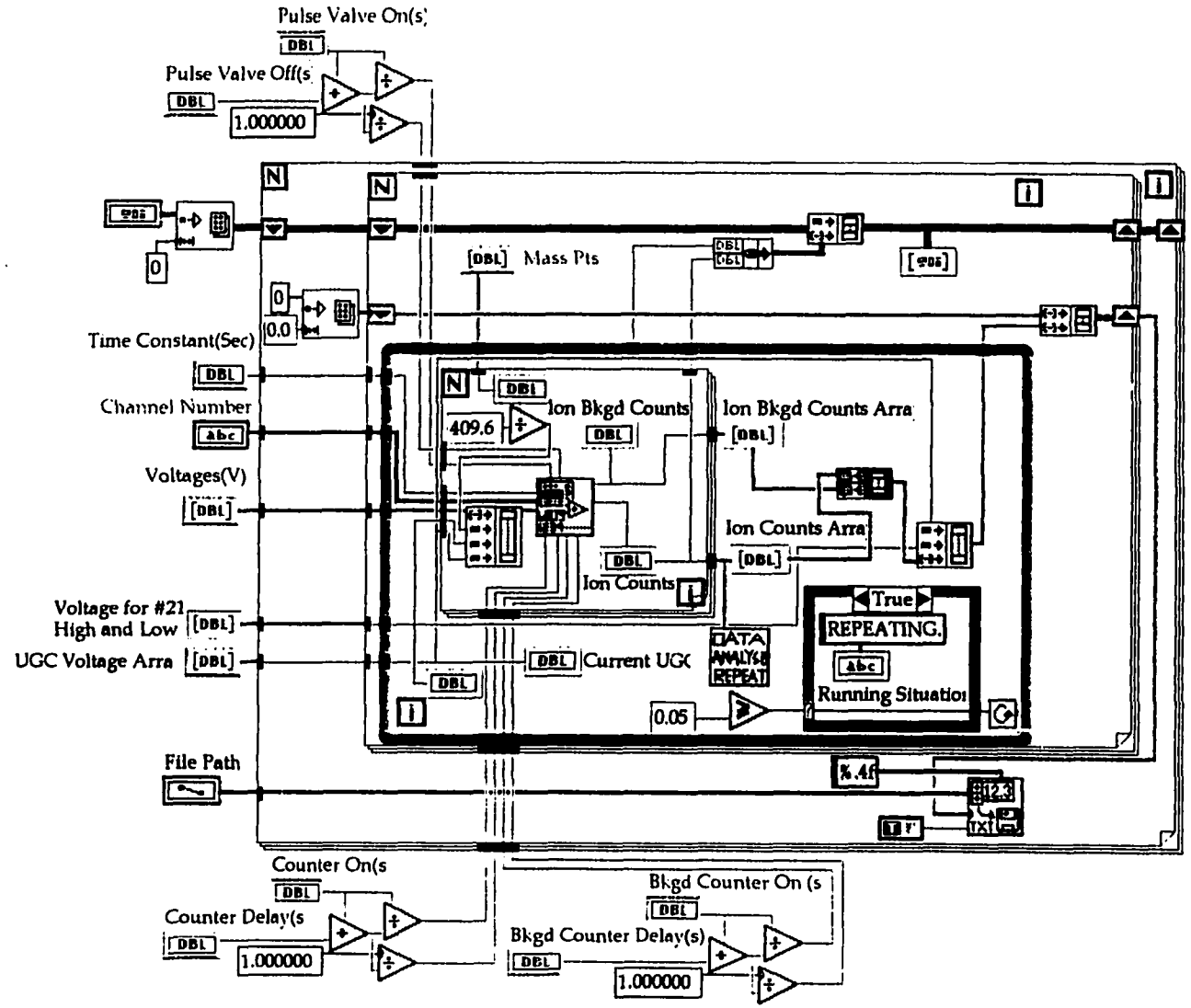
Pulse Valve On(s)
Pulse Valve Off(s
1.000000
Mass Pts
Time Constant(Sec)
Channel Number
Voltages(V)
Voltage for #21 High and Low
UGC Voltage Arra
File Path
409.6
Ion Bkgd Counts
Ion Bkgd Counts Arra
Ion Counts Arra
Ion Counts
Current UGC
True
REPEATING.
Running Situatio
0.05
%.4f
Counter On(s
Counter Delay(s
1.000000
Bkgd Counter On (s
Bkgd Counter Delay(s)
1.000000

interest is counted for the time period set forth by the "Time Constant(Sec)". The collected results are then output to indicators and the graph display. The most important array, "Ion Counts Array", is also sent to the floppy disk for permanent storage and to the "DATA ANALYSIS REPEAT" sub-vi for validity checks. The greatest advantage of this virtual instrument is the automated computer-control of the voltage variation during run-time, which reduces inaccuracies induced by manual adjustments. Shown in Figure 12, 13 and 14 are the front panel and the block diagrams of "set and count pulse(ei-pv).vi" sub-vi.

As can be seen, this sub-vi is an independent VI itself. The fact thatit is recalled in a higher level VI, in this case the Differential Retarding Method.vi, renders it a sub-vi. Notice the small icon on the upper right corner of Fig.12. This icon represents "set and count pulse(ei-pv).vi" in higher level VIs.

The "set and count pulse(ei-pv).vi" sub-vi demands some initial condition inputs in the "CONTROLS" block for voltage setup and in the "Parameters For Counters" block for counters' configuration. It then outputs the data through two indicators in the "INDICATORS" block. The block diagram contains a Sequence structure. In frame 0 in Fig. 13 a sub-vi "AO ONE PT" is used to set the desired voltages on the AT-AO-10 board for coupling with the electrostatic lenses or the quadrupole controls. After the voltages are set, the lock-in counters are set to work in frame 1 in Fig. 14. The related counters are configured according to the parameters received and then started. The results are read after the time period defined in the "Time Constant(sec)" expires. Then the counters are stopped. The next call to this sub-vi re-starts the above actions.

Figure 12 Front panel of the "set and count pulse(ei-pv).vi" sub-vi for the Retarding Differential Method(EI-PV).vi

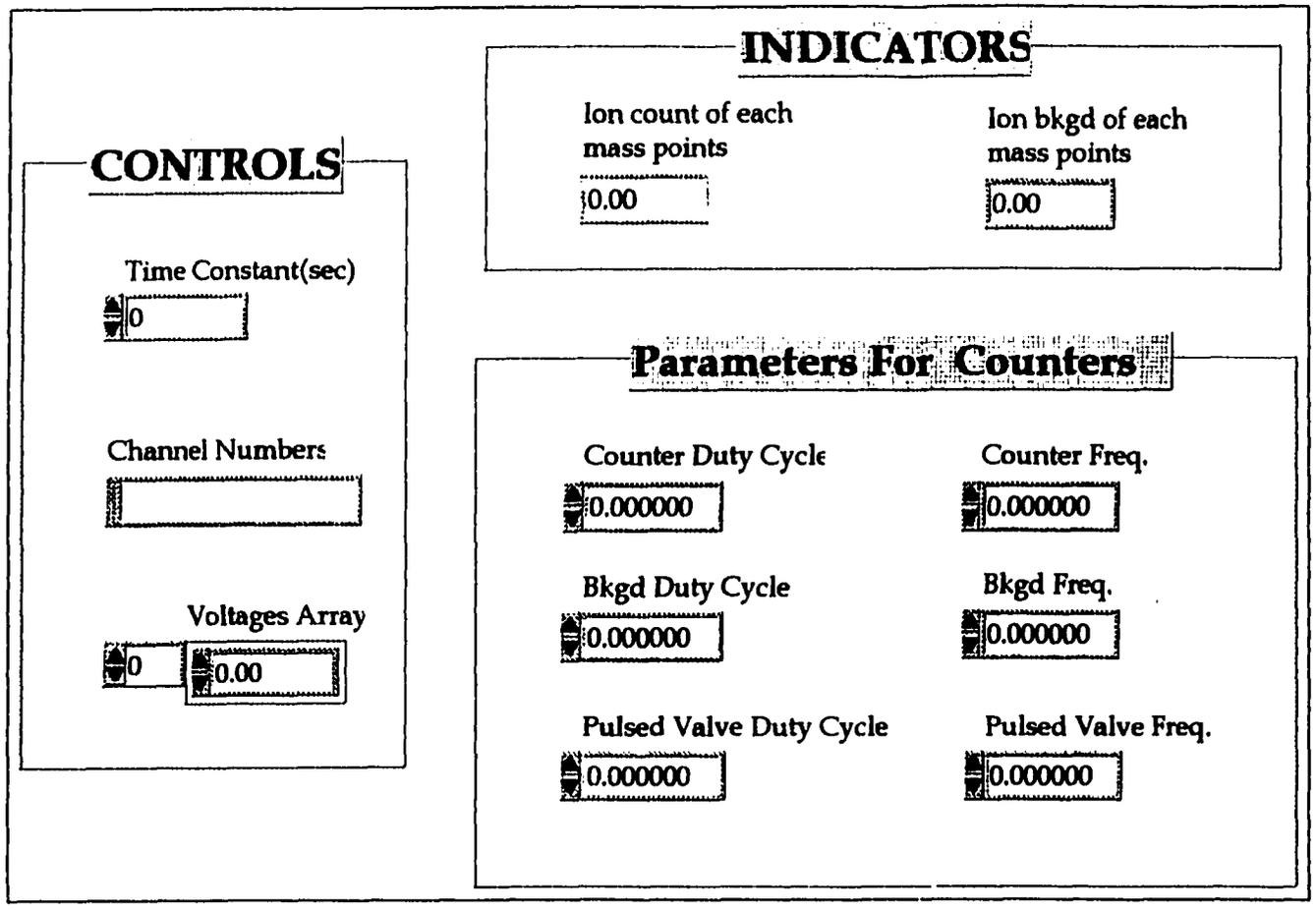
INDICATORS
Ion count of each mass points
0.00
Ion bkgd of each mass points
0.00
CONTROLS
Time Constant(sec)
0
Channel Numbers
Voltages Array
0
0.00
Parameters For Counters
Counter Duty Cycle
0.000000
Counter Freq.
0.000000
Bkgd Duty Cycle
0.000000
Bkgd Freq.
0.000000
Pulsed Valve Duty Cycle
0.000000
Pulsed Valve Freq.
0.000000

Figure 13 First page of the block diagram of the "set and count pulse(ei-pv).vi" sub-vi for the Retarding Differential Method(EI-PV).vi

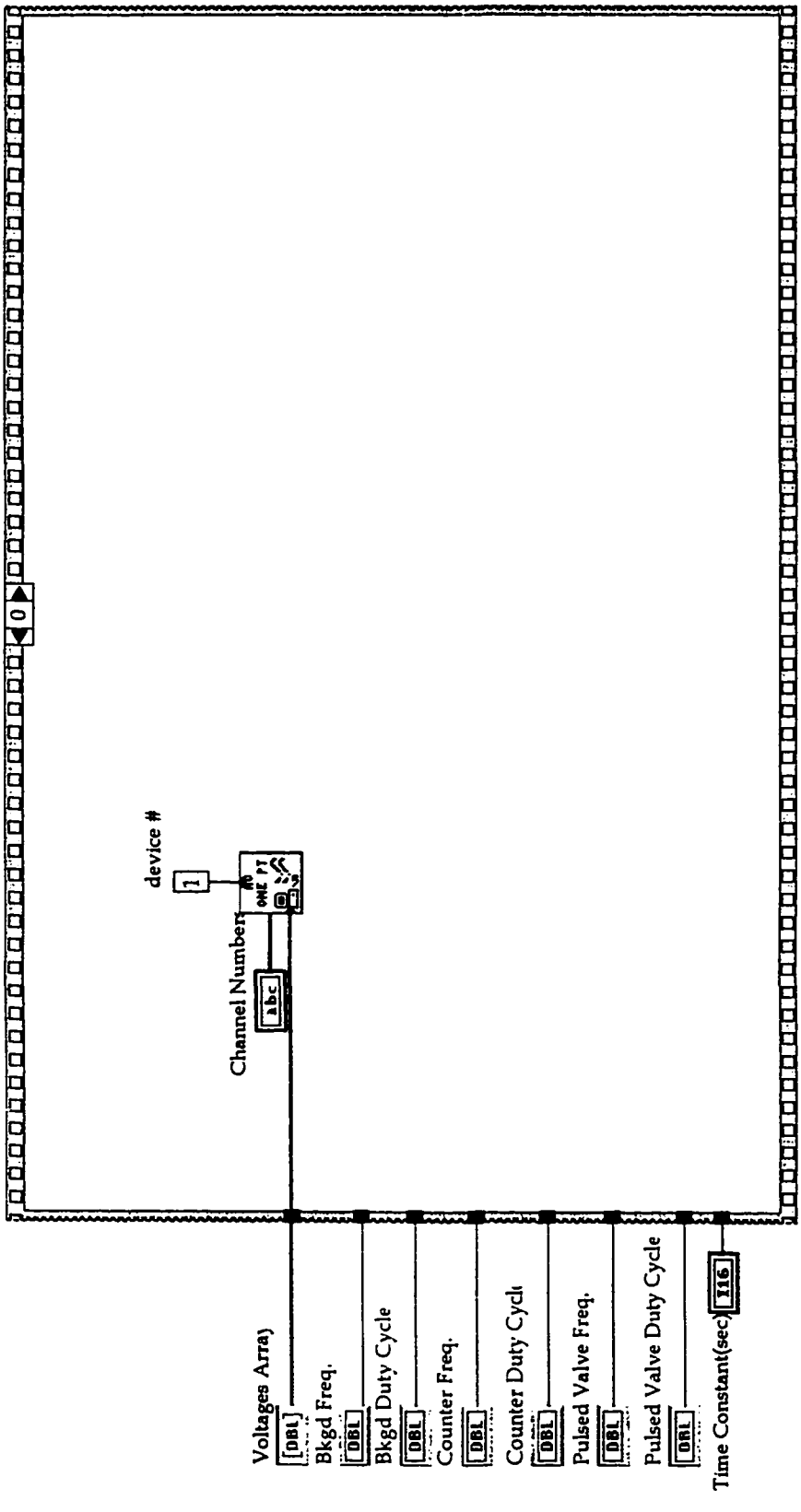
0
device #
1
Channel Number
abc
Voltages Array
DBL
Bkgd Freq.
DBL
Bkgd Duty Cycle
DBL
Counter Freq.
DBL
Counter Duty Cycl
DBL
Pulsed Valve Freq.
DBL
Pulsed Valve Duty Cycle
DBL
Time Constant(sec)
116

Figure 14 Second page of the block diagram of the "set and count pulse(ei-pv).vi" sub-vi for the Retarding Differential Method(EI-PV).vi

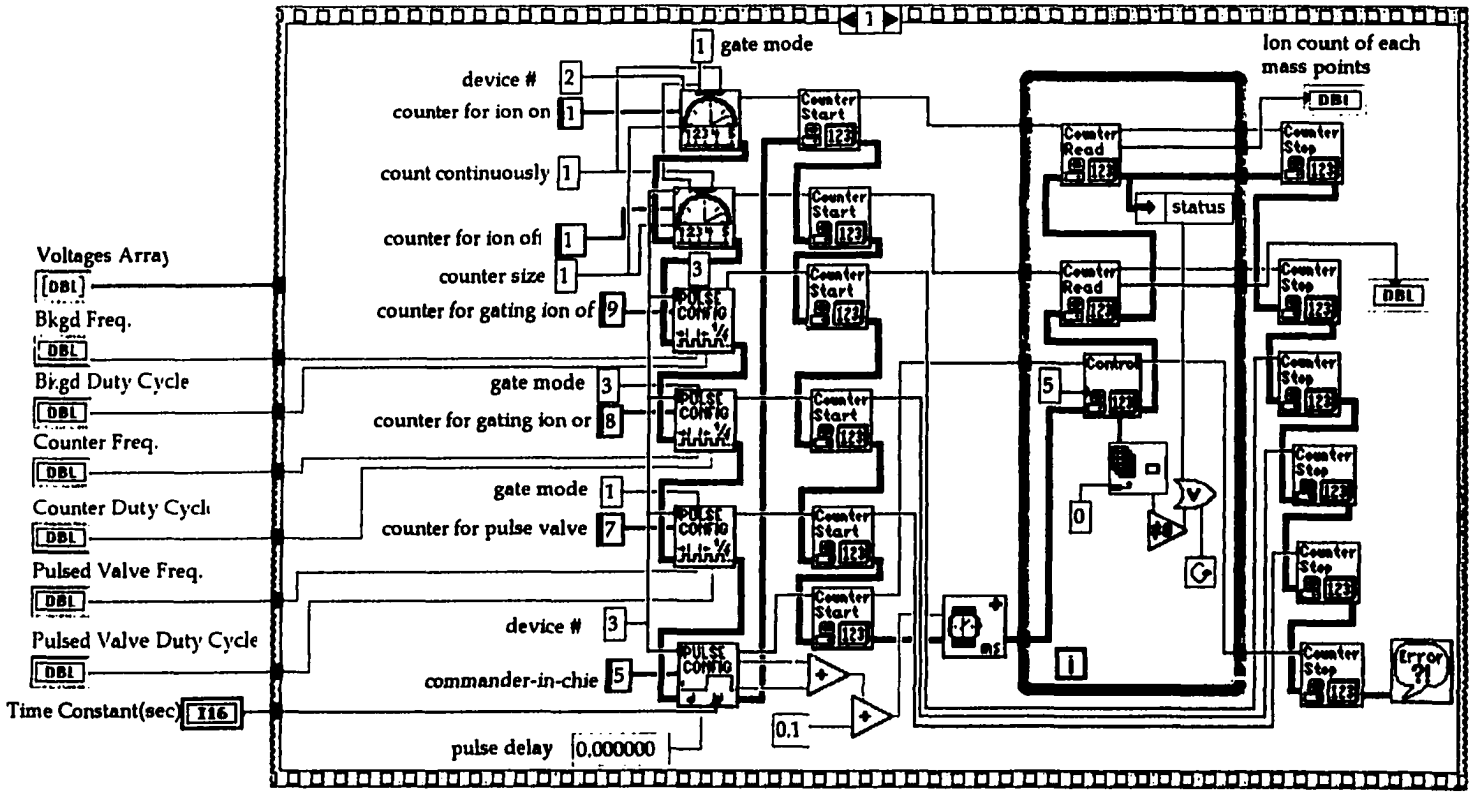
Voltages Array
Bkgd Freq.
Bkgd Duty Cycle
Counter Freq.
Counter Duty Cycle
Pulsed Valve Freq.
Pulsed Valve Duty Cycle
Time Constant(sec)
gate mode
device #
counter for ion on
count continuously
counter for ion of
counter size
counter for gating ion of
gate mode
counter for gating ion or
gate mode
counter for pulse valve
device #
commander-in-chie
pulse delay
0.000000
0.1
Ion count of each mass points
Counter Start
Counter Read
Counter Stop
status
Control
Error

Conclusions

In this paper we have discussed some of the concepts of computer-based instrumentation and their applications in our TQDO experiments. At this first step, we have been able to exploit modern PC technology and plug-in data acquisition boards methodology, as well as state-of-the-art software tools, to build easy-to-use virtual instruments that greatly reduce human labor and partially automate the experimental setup and data acquisition process. Further implementation of the instrumentation techniques and automation are under way in the existing apparatus. For instance, we recently purchased an MCS card for TOF study. We intend to incorporate the operation of this card into our existing PC-based instrumentation. We believe the on-going PC-based instrumentation and automation process is full of potential in our future research.

REFERENCES

1. Tooley, Mike. *"PC-based Instrumentation and Control" 2nd edition* (NEWNES, Oxford, 1995).
2. Gupta, S. and Gupta, J.P. *"PC Interfacing for Data Acquisition and Process Control"* (Instrument Society of America 1994).
3. Fribance, Austin E. *"Industrial Instrumentation Fundamentals"* (McGraw Hill, New York, 1962).
4. Cerni, R.H. and Foster, L.E. *"Instrumentation for Engineering Measurement"* (John Wiley, New York, 1962).
5. Bouwens, A.J. *"Digital Instrumentation"* (McGraw Hill, New York, 1984).

6. Morrison, Ralph *"Instrumentation Fundamentals and Applications"* (John wiley, New York, 1984).

7. *"IEEE Standard 488"* (IEEE Standards Office, New York, 1978).

8. Earnshaw, R. and Vince, J. *"Computer Graphics: developments in virtual instruments"* (Academic Press, San Diego, 1995).

9. Tannenbaum, A.S. *"Computer Networks"* (Prentice Hall, Englewood Cliffs, NJ, 1981).

10. Miner, G.F. *"Physical data acquisition for digital processing: components, parameters, and specifications"* (Prentice Hall, Englewood Cliffs, NJ, 1992).

11. Black, J. *"The system engineer's handbook: a guide to building VME bus and VXI bus systems"* (Academic Press, San Diego, 1992).

12. Voss, G. *"Object Oriented Programming: An Introduction"* (Osborne McGraw Hall, Berkeley, CA, 1991).

13. Dahl, O.J.; Dijkstra, E.W.; and Houe, C.A.R. *"Structured Programming"* (Academic Press, New York, 1972).

14. C. Y. Ng, in "*Techniques for the Study of Gas-Phase Ion-Molecule Reactions*", J. M. Farrar and W. H. Saunder, Jr., eds. (Wiley, New York, 1988), p.417.

15. C. Y. Ng, in "*State-Selected and State-to-State Ion-Molecule Reaction Dynamics: I. Experiment*", C. Y. Ng and M. Baer, eds. (Wiley, New York, 1992), p. 401.

16. G. D. Flesch, S. Nourbakhsh, and C. Y. Ng, *J. Chem. Phys.* **92**, 3590 (1990).

17.C.-L. Liao, J.-D. Shao, R. Xu, G. D. Flesch, Y.-G. Li, and C. Y. Ng, *J. Chem. Phys.* **85**, 3874 (1986).

18.J.-D. Shao, Y.-G. Li, G. D. Flesch, and C. Y. Ng, *Chem. Phys. Lett.* **132**, 58 (1986).

19.J.-D. Shao, Y.-G. Li, G. D. Flesch, and C. Y. Ng, *J. Chem. Phys.* **86**, 170 (1987).

20.G. D. Flesch and C. Y. Ng, *J. Chem. Phys.* **89**, 3381 (1988); G. D. Flesch, S. Nourbakhsh, and C. Y. Ng, *J. Chem. Phys.* **95**, 3381 (1991).

21.G. D. Flesch and C. Y. Ng, *J. Chem. Phys.* **92**, 2876 (1990).

22.X. Li, Y.-L. Huang, G.D. Flesch, and C.Y.Ng, *Rev. Sci. Instrum.* **65**, 3724 (1994).